ISSN Print: 2518-4245
ISSN Online: 2518-4253
Vol. 61(4), December 2024

PROCEEDINGS
OF THE PAKISTAN ACADEMY OF SCIENCES:
A. Physical and Computational Sciences

PAKISTAN ACADEMY OF SCIENCES
ISLAMABAD, PAKISTAN

Proceedings of the Pakistan Academy of Sciences: Part A Physical and Computational Sciences

Proceedings of the Pakistan Academy of Sciences A. Physical and Computational Sciences is the official flagship, the peer-reviewed quarterly journal of the Pakistan Academy of Sciences. This open-access journal publishes original research articles and reviews on current advances in the field of Computer Science (all), Materials Science (all), Physics and Astronomy (all), Engineering Sciences (all), Chemistry, Statistics, Mathematics, Geography, Geology in English. Authors are not required to be Fellows or Members of the Pakistan Academy of Sciences or citizens of Pakistan. The journal is covered by Print and Online ISSN, indexed in Scopus, and distributed to scientific organizations, institutes and universities throughout the country, by subscription and on an exchange basis.

Annual Subscription: **Pakistan:** Institutions, Rupees 8000/-; Individuals, Rupees 4000/- (Delivery Charges: Rupees 300/-)
Other Countries: US$ 200.00 (includes air-lifted overseas delivery)

HEC Recognized; Scopus Indexed

Published by **Pakistan Academy of Sciences**, 3 Constitution Avenue, G-5/2, Islamabad, Pakistan
Email: editor@paspk.org; **Tel:** 92-51-920 7140 & 921 5478; **Websites:** www.paspk.org/proceedings/; www.ppaspk.org

Printed at **Graphics Point.,** Office 3-A, Wasal Plaza, Fazal-e-Haq Road Blue Area Islamabad.
Ph: 051-2806257, **E-mail:** graphicspoint16@gmail.com

PROCEEDINGS OF THE
PAKISTAN ACADEMY OF SCIENCES: PART A
Physical and Computational Sciences

CONTENTS

Volume 61, No. 4, December 2024 **Page**

Research Articles

Submission of Manuscripts: Manuscripts may be submitted as an e-mail attachment at editor@paspk.org or submit online at http://ppaspk.org/index.php/PPASA/about/submissions. Authors must consult the ***Instructions for Authors*** at the end of this issue or at the Website: www.paspk.org/proceedings/ or www.ppaspk.org.

Proceedings of the Pakistan Academy of Sciences: A Physical and Computational Sciences 61(4): 317-323 (2024)

ISSN (Print): 2518-4245; ISSN (Online): 2518-4253
http://doi.org/10.53560/PPASA(61-4)677

Pakistan Academy of Sciences

Research Article

Measurement of Uranium Concentrations in the Soil Samples of Nineveh Province, Iraq Using CR-39 Detector

Malik H. Kheder* and Hanaa N. Azeez

Department of Physics, College of Education for Pure Sciences,
University of Al-Hamdaniya, Nineveh, Iraq

Abstract: The physiological influence of radiation, which may induce cancer, makes the radioactive field vital to human health. Radon, which is hazardous to both humans and the environment, is deposited in soil via uranium decay. Extended exposure to elevated levels of alpha radiation, primarily radon, causes lung cancer. Thus, research is necessary to observe how the levels of human exposure vary. In evaluating natural exposure radiation, it is essential to control the quantity of radionuclides in the soil by determining the radioactivity level from these sources. Twenty samples of soil from different places in the Nineveh province in northern Iraq were analyzed for uranium content by the CR-39 nuclear track detector. These samples had radon concentrations ranging from 27.221 to 59.407 $Bq.m^{-3}$, and the mean is 38.917 $Bq.m^{-3}$. This mean value is below the level of reference limits 100 $Bq.m^{-3}$ of the World Health Organization (WHO). Uranium levels ranged values from 0.129 to 0.281 ppm, with a mean of 0.182 ppm. Findings demonstrate that the natural radiations in the region are within the permissible range, as shown when comparing the results to global averages, the uranium concentration levels fell below the average of global value 2.8 ppm, and below the acceptable limit of 11.7 ppm.

Keywords: Nineveh Province, Soil Samples, Uranium Concentrations, CR-39 Detector, Radon Concentrations.

1. INTRODUCTION

Soil is a major natural source of radioactivity because of its mineral richness. It also makes people more vulnerable to radiation and helps release radioactive materials into the environment. For these reasons, soil's inherent radioactivity is thought to be a key sign of radioactive contamination [1]. The concentration of radionuclides in soil is the primary indicator of natural background radiation [2]. The natural radioactivity can differ significantly across different types of soil. Natural occurring radioactive elements (NORMs) are present in soil and the environment. These elements are the released nuclear radiation from naturally occurring radionuclide materials. Uranium is one of these radionuclides that is produced by nuclear technology [3]. Similar to other minerals, uranium is an element naturally occurring that has existed since the beginning of the earth. Since each uranium isotope is radioactive, its quantity needs to be controlled [4]. It turns into a non-radioactive lead as it decays, releasing alpha particles. A progeny, also known as a decay product, is a new radionuclide that occurs along the decay chain. It adds approximately seven times as much radioactivity to the soil as uranium does. In rocks and soil, The closest source of radium and radon is uranium. One of the primary causes of background radiation is radon, a uranium derivative [5]. Because of its chemical and radioactive characteristics, uranium that accumulates in people may have two effects. Humans may suffer negative consequences from consuming large amounts of uranium and the byproducts of its decay. The Harmful effects on humans are caused by high uranium intake and by-products of its decay. Exposure to naturally soluble uranium of 0.1 mg/kg causes chemical temporary kidney damage [6]. Primordial radionuclides enter the soil through the weathering of the earth's crust. It took the radionuclides in the soil by plants up through their roots and passed them on to humans when crops are consumed, resulting in internal

Received: April 2024; Revised: November 2024; Accepted: December 2024
* Corresponding Author: Malik H. Kheder <malik.19732013@yahoo.com>

exposure to ionizing radiation. Radionuclides consumed through food are major radiation pathways for health long-term considerations, significantly contributing to average doses of radiation to different human body parts and tissues The primary uranium and radium deposition sites are the kidneys, liver, and bones [7]. The uranium amount in the soil varies greatly depending on the geological region; it can range from 0.1 to 20 ppm [8], with a global average of 2.8 ppm and 11.7 ppm being the permitted limit [9, 10]. The plastic CR-39 detector was used to measure The amount of uranium present in soil, due to the great sensitivity of CR-39 to alpha particles of low energy. These tracks are examined under a microscope following the etching procedure to magnify them [11]. The goal of the research is to identify the precise uranium content in twenty samples of soil from the Nineveh province in Iraq.

2. MATERIALS AND METHODS

Twenty samples of soil were gathered in the Iraqi province of Nineveh from various places as in (Figure 1). The samples were taken 30 cm below the surface. The samples were sieved using a 0.2 mm mesh and baked for 24 hours at 100 °C. After that, samples were placed inside a uranium dosimeter, which was covered with plastic tape to keep radionuclides from escaping into the atmosphere (Figure 2). Utilizing a radioactive uranium dosimeter, solid-state track detector techniques were employed in the measurements. Each container has a 7 cm diameter and a height of 10 cm. It holds one CR-39 detector (1 x 1) cm^2. Upon arriving at the detector, alpha particles leave traces. The average concentration of radon is directly correlated with the number of tracks. A sample of 50 g in a cylindrical plastic container (uranium dosimeter) was placed with its back to the CR-39 detector. The sample is 3 cm in height and 7 cm from the detectors to the sample surfaces, closed for 60 days. Detectors were removed after 60 days, and the tracks were revealed by the NaOH etching at normality 6.25 N in the water bath at 70 °C heated. Detectors were cleaned and then tracks were tallied using a microscope at 400x magnification. The following formula is used to calculate track densities [12].

$$\rho = (\text{The tracks number})/(\text{The field of view area}) \quad (1)$$

The track density ρ(in track.cm^{-2}) in sample air space is related to exposure duration T(in a day), and then concentrations of radon CRn (Bq.m^{-3}) can calculated using the relation [13].

$$C_{Rn} = \rho/KT \quad (2)$$

To calculate the radon concentration, the track density of the detector ρ(track.m^{-2}) was used. The radon concentration C_{Rn}(Bq.m^{-3}) during the period of irradiation t(s) is connected to the density of tracks, or total tracks number per area of the detector's field of view via microscope, utilizing the sensitivity of detector K(m), as in the Equation (2). The sensitivity K in a unit of (m) is defined as the density of track per exposure unit of (Bq.s.m^{-3}). From equation (2), the unit $K = (\text{track}.m^{-2})/(\text{Bq}.\text{s}.m^{-3})$.

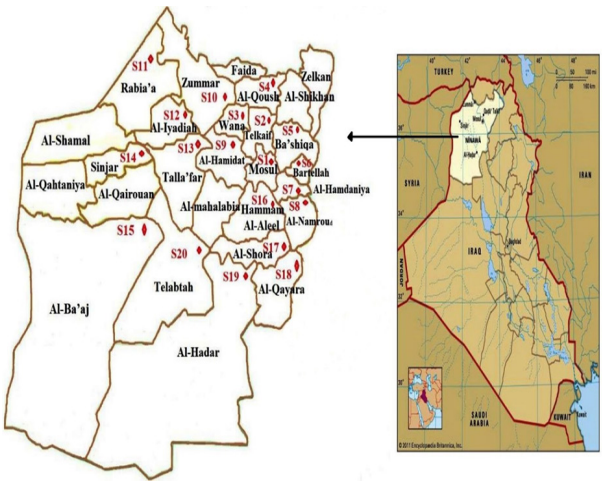

Fig. 1. The sitemap of the samples.

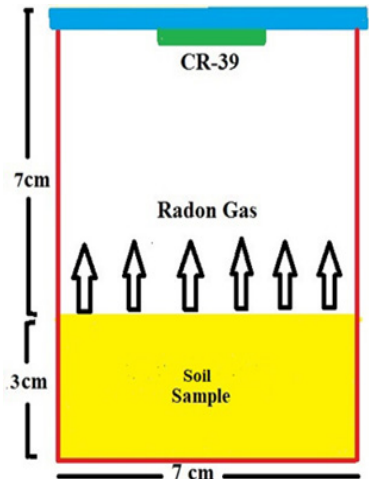

Fig. 2. The sealed-can technique (uranium dosimeter).

Since the unit of Bq is equal to decay/s and each decy leaves a track on the detector then 1Bq = 1track/s, then K will be in unit of (m). The Sensitivity K is given traditionally, in track/cm^2 per Bq.d/m^3. To convert K from the definition in equation (3) to traditionally, the units (cm, d) must converted to (m, s), where 1m = 100 cm, 1day = 86400s, then subtiuting the values of m, s in equation (3) produce

$$(m) = (\text{track}.cm^{-2}10^{-4})/(\text{Bq}.\text{d}\ \frac{1}{86400}.m^{-3}).$$

Then, $(m) = 8.64(\text{track}.cm^{-2})/(\text{Bq}.\text{d}\,.m^{-3})$.

Divided by 8.64 to convert to m or m must be multiplied by 8.64 to convert to track.cm^{-2} per Bq.d.m^{-3} or by 0.0864 if K in cm) [14]. K determined using the relation.

$$K = (\frac{1}{4})r(2cos\theta_c - r/R_i) \quad (3)$$

where, the sealed container radius r is 3.5 cm, θ_c is the critical angle of the CR-39 detector equal to 35^o, and R_i is the range of alpha particle in air equal to 4.09 cm (for alpha particle emitted from radon with energy 5.49 MeV) [15-17]. R_i is calculated by the relation.

$$R_i = 0.318\ E_i^{3/2} \quad (4)$$

K is then equal to 0.684 cm and has the value (0.0591 Traks.cm^{-2}.day^{-1}/Bq.m^{-3}) after multiplying by 0.0864 [18]. The formula determines the sample's radon concentration Rn [19].

$$C_s = \lambda_{Rn} C_{Rn} HT/L \quad (5)$$

where C_s (Bq.m^{-3}) represents the inside sample's radon concentration, the C_{Rn} (Bq.m^{-3}) represents radon in the air of the sample, λ_{Rn} (0.1814 day^{-1}) of the sample air space The can's air space height, T (sixty days) is the exposure time, and the radon decay constant, H (7 cm). L (3cm) is the thickness of the sample. The activity of the sample's radon (A_{Rn}) was calculated using the formula.

$$A_{Rn} = C_s V \quad (6)$$

where A_{Rn} represents the sample radon activity. The scan radius is r, and the sample's volume is (V = πr^2 L) = 115.4X10^{-6}m^3 [20]. From the radon activity and the number of radon atoms N_{Rn}, the uranium concentration is obtained using the following formula [21].

$$A_{Rn} = \lambda_{Rn}\ N_{Rn} \quad (7)$$

The uranium atoms number in the sample (N_U) is calculated using the equation of secular equilibrium, which states that uranium activity is equal to radon activity.

$$\lambda_U N_U = \lambda_{Rn} N_{Rn} \quad (8)$$

Where λ_U (4.883X10^{-18} sec^{-1}) is the decay constant of uranium and the equation determines the weight of uranium inside the sample [22].

$$W_U = N_U\ At_U\ /N_{avo.} \quad (9)$$

The Avogadro number is Navo. (6.02X10^{23} atom/mol), and the mass number of uranium is represented by At_U. The concentration of uranium is calculated from relation [23].

$$C_U = W_U/W_s \quad (10)$$

where, Ws (50 grams) is the sample mass and C_U (ppm) is the uranium concentration [24].

3. RESULTS AND DISCUSSION

The results obtained from the present study are presented in Table 1. It was discovered that the range of uranium concentrations was (0.129 - 0.281) ppm, and the mean value was 0.182 ppm as displayed in Figure 3. The estimated radon concentration values in soil samples fall within the range of (27.221 - 59.407) Bq.m^{-3}. The uranium content and soil location determine the uranium concentration values in the samples, which vary from one sample to the next. The local geology of the area, along with mineralization, geophysical, and climatological factors, determines the amount of radon gas in the soil and the rate at which it is exhaled. Mountainous areas and near hills have higher concentration values than areas near the river because river flow may reduce concentrations.

Sample S15 Al-Ba'aj had the lowest reported Uranium concentration (0.129 ppm), which is an open soil area without stones far from the river water. While sample S11 Rabia'a had the highest value (0.281 ppm), this location is a large agricultural area

Table 1. Soil sample findings related to track density, the radon concentration in the sample air, radon concentration in the soil, and uranium concentration.

S. No.	Location	ρ Track / cm^2	C_{Rn} Bq/m^3	C_S Bq/m^3	C_U ppm
S1	Mosul	120	33.898	860.8814	0.160
S2	Telkaif	140	39.719	1008.709	0.188
S3	Wana	131	37.151	943.4912	0.176
S4	Al-Qoush	119	33.727	856.5335	0.160
S5	Ba'shiqa	138	39.034	991.3179	0.185
S6	Bartellah	132	37.322	947.8391	0.177
S7	Al-Hamdaniya	141	40.061	1017.405	0.190
S8	Al-Namroud	128	36.295	921.7518	0.172
S9	Al-Hamidat	198	56.154	1426.106	0.266
S10	Zummar	180	51.018	1295.67	0.242
S11	Rabia'a	210	59.407	1508.716	0.281
S12	Al-Iyadiah	121	34.240	869.5771	0.162
S13	Talla'far	155	43.828	1113.059	0.207
S14	Sinjar	166	46.909	1191.321	0.222
S15	Al-Ba'aj	96	27.221	691.3138	0.129
S16	Hammam Al-Aleel	165	46.704	1186.103	0.221
S17	Al-Shora	108	30.576	776.5324	0.145
S18	Al-Qayara	105	29.720	754.7929	0.141
S19	Al-Hadar	102	28.899	733.9231	0.137
S20	Telabtah	100	28.419	721.749	0.134
	Min	96	27.221	691.3138	0.129
	Max	210	59.407	1508.716	0.281
	Mean	137.5	38.917	989.84	0.182

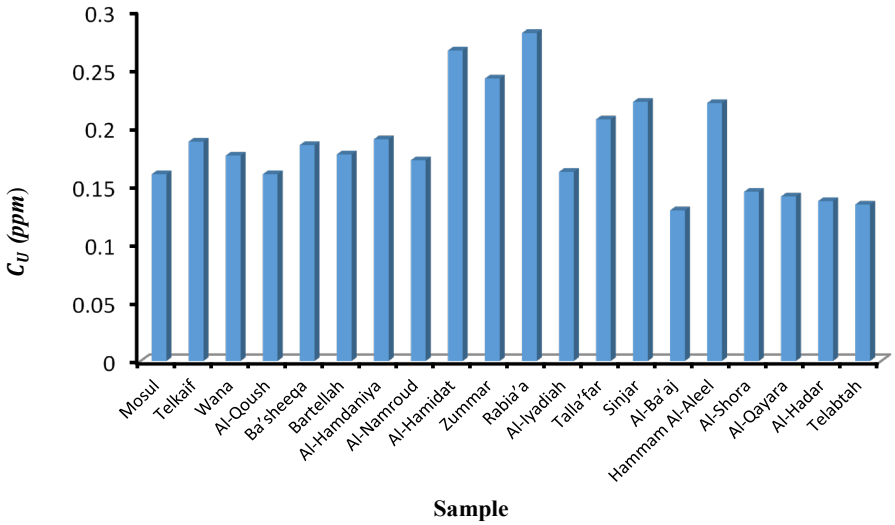

Fig. 3. The uranium concentration (ppm) in samples.

in which organic and chemical fertilizers are widely used. These fertilizers may contain a percentage of radioactive materials, although the percentage is small, but it may contribute to increasing uranium concentrations in this area. The average uranium concentration was 0.182 ppm which is lower than the global average of 11.7 ppm. The compression with recent measurements in Iraq is displayed in Table 2.

Table 2 indicates that the obtained values fall within a certain range of values published for different regions of Iraq. It is far lower than the Sulaimani region, Um Qasr district, and the southern Basrah governorate. Higher than the Al-Najaf area, it lies in the middle of the other measurements in the AL-Hamdaniya region of Mosul and regions of Jalawla'a city-Diyala. The origin of soil types, geochemical makeup, and reported concentrations on dry soil samples all point to the possibility that radioactively rich sandstone is the source of the elevated recorded radionuclide values in the soil sample from that particular area. Therefore, it was concluded that no harmful effects from the radiation and that the population of the research zone is safe from radioactive threats and health concerns coming from the concentrations of uranium in the soil.

4. CONCLUSIONS

The majority of the investigation's uranium-specific activity result values showed that soil samples had less uranium than the average amount found worldwide. Sample S15 Al-Ba'aj had the lowest reported Uranium concentration, which is an open soil area without stones far from the river water. While sample S11 Rabia'a had the highest value, this location is a large agricultural area in which organic and chemical fertilizers are widely used. These fertilizers may contain a percentage of radioactive materials, although the percentage is small, but it may contribute to increasing uranium concentrations in this area. It was discovered that the uranium content was below both the UNSCEAR-recommended global average of 2.8 ppm and the maximum permissible level of 11.7 ppm. Therefore, it was concluded that no harmful effects from radiation and that the population of the research zone is safe from radioactive threats and health concerns coming from the concentrations of uranium from the soil.

5. CONFLICT OF INTEREST

The authors declare no conflict of interest.

6. REFERENCES

1. S. Rahman and M. Faheem. Natural radioactivity measurements in Pakistan an overview. *Journal of Radiological Protection* 28(4): 443-52 (2008).
2. K. Kapanadze, A. Magalashvili, and P. Imnadze. Distribution of natural radionuclides in the soils and assessment of radiation hazards in the Khrami Late Variscan crystal massif (Georgia). *Heliyon* 5(3): e01377 (2019).
3. P. Egidi. Introduction to Naturally Occurring Radioactive Material (01 August 1997, No. CONF-970795-1). *Oak Ridge National Lab. Grand Junction CO. United States* (1997).
4. G. Graetz. Energy for whom? Uranium mining, Indigenous people, and navigating risk and rights in Australia. *Energy Research and Social Science* 8: 113–126 (2015).
5. P. Todorov and E. Ilieva. Contamination with

Table 2. The compression of results with other measurements in Iraq.

No.	Research	Location	Uranium concentration (ppm)		
			Min	Max	Mean
1.	Present work	Nineveh province -Iraq	0.129	0.281	0.182
2.	[25] 2017	AL-Hamdaniya-Mosul-Iraq	0.313	0.784	0.488
3.	[26] 2015	Sulaimani - Iraq	1.253	18.225	6.029
4.	[27] 2014	Al-Najaf - Iraq	0.0935	0.1843	
5.	[28] 2013	Jalawla'a city-Diyala-Iraq	0.719	1.280	
6.	[29] 2022	Southern Basrah governorate	0.65	2.67	1.382
7.	[30] 2023	Um Qasr district, Iraq	0.6	2.2	1.3

uranium from natural and anthropological sources. *Romanian Journal of Physics* 50(9-10): 25–30 (2005).
6. A.B. Tanner. Radon Migration in the Ground: a Supplementary Review. In: The Natural Radiation Environment III: Proceedings of the 3rd International Symposium on the Natural Radiation Environment. T.F. Gesell and W.M. Lowder (Eds.). *U.S. Department of Energy, Washington USA* pp. 5–55 (1978).
7. M.H. Kheder. Radium and Uranium Concentrations in Some Fruits and Vegetables Cultivated in Nineveh Governorate, Iraq. *Iraqi Journal of Applied Physics* 19(3B): 15–19 (2023).
8. S. Sahoo. Measurement of uranium and its isotopes at trace levels in environmental samples using mass spectrometry. *Indian Journal of Physics* 83: 787–797 (2009).
9. B. Saied, R. Al-Khafaji, and A. Al-Bayati. Measurement of Uranium Concentration in the Soil Samples by Using Solid State Nuclear Track Detectors (SSNTDs). *International Journal of Scientific Research and Technology* 2(4): 130–135 (2016).
10. UNSCEAR. United Nations Scientific Committee on the Effects of Atomic Radiation. *Sources and Effects of Ionizing Radiation. vol. 2. United Nations New York* (2000).
11. R.L. Fleischer, P.B. Price, and R.M. Walker (Eds.). Nuclear Tracks in Solids: Principles and Applications. *University of California Press* (1975).
12. M. Kheder. Measurement of radon concentration using SSNTD in Bartella region. *Al-Mustansiriyah Journal of Science* 29: 110–116 (2019).
13. N. Ahmad, M. Jaafar, S. Khan, T. Nasir, S. Ahmad, and M. Rahim. Measurement of radon exhalation rate, radium activity and annual effective dose from bricks and cement samples collected from Dera Ismail Khan. *American Journal of Applied Sciences* 11: 240 (2014).
14. D. Nikezic, K. Yu, and J. Stajic. Computer program for the sensitivity calculation of a CR-39 detector in a diffusion chamber for radon measurements. *Review of Scientific Instruments* 85: 22102 (2014).
15. M. Kheder, H. Azeez, and F. Al-Jomaily. Alpha Emitters Radioactivity Concentrations in Some Cosmetics Used in Iraq Using LR-115 Detector. *EUREKA: Physics and Engineering* 2: 65–70 (2020).
16. M. Mansy, M. Sharaf, H. Eissa, S. El-Kamees, and M. Abo-Elmagd. Theoretical calculation of SSNTD response for radon measurements and optimum diffusion chambers dimensions. *Radiation Measurements* 41: 222–228 (2006).
17. A.Kh. Thannon, M.H. Kheder, Y.Y. Kassim, and H.N. Azeez. Environmental and Radioactive Contamination in the Village of Kabarli in the Nineveh Plain Region in Iraq. *Iraqi Journal of Applied Physics* 20(3): 561–564 (2024).
18. M. Kheder, L. Najam, R. Mahmood, and F. Majeed. Radioactivity concentrations in barley and wheat crops in Nineveh plain region in Iraq. *International Journal of Nuclear Energy Science and Technology* 14(1): 50–60 (2020).
19. G. Somogyi, A. Hafez, I. Hunyadi, and M. Toth-Szilagyi. Measurement of exhalation and diffusion parameters of radon in solids by plastic track detectors. *International Journal of Radiation Applications and Instrumentation. Part D. Nuclear Tracks and Radiation Measurements* 12(1-6): 701–704 (1986).
20. M. Kheder, A. Ahmad, H. Azeez, and I. Mustafa. Radium and Uranium Concentrations of Powder Juice in the Iraq Markets Using CR-39 Detector. *Journal of University of Babylon for Pure and Applied Sciences* 27 (6): 341–349 (2019).
21. M. L'Annunziata (Ed.). 2nd edition. Radioactivity: introduction and history, from the quantum to quarks. *Elsevier* (2016).
22. E. Podgorsak (Ed.). Basic Radiation Physics. Radiation Oncology Physics: A Handbook for Teachers and Students. *IAEA, Vienna Austria* (2005).
23. M. Kheder, L. Najam, and H. Azeez. Long-lived alpha emitters concentrations in the spices consumed in Iraq using CR-39 detector. *Journal of University of Babylon for Pure and Applied Sciences* 28(1): 274–283 (2020).
24. M. Kheder, A. Ahmad, H. Azeez, M. Slewa, B. Badr, and S. Sleeman. Radon and uranium concentration in ground water of nineveh plain region in Iraq. *Journal of Physics: Conference Series* 1234: 012033 (2019).
25. M. Kheder, H. Azeez, M. Slewa, and T. Zaker. Determination of Uranium Contents in Soil Samples in Al-Hamdaniya Region Using Solid State Nuclear Track Detector CR-39. *Al-Mustansiriyah Journal of Science* 30(1): 199–204 (2019).
26. K. Abdullah, S. Muhammed, and A. Hussein. Assessment of Rn and U concentrations in the soil of Qadafery, Kalar and Zarayan located in Sulaimani governorate of Kurdistan region-Iraq. *American Journal of Environmental Protection* 4(1): 40–44 (2015).

27. A. Abojassim. Uranium concentrations measurement for groundwater and soil samples in Al-Najaf/Iraq. *IOSR Journal of Applied Chemistry* 6: 61–65 (2014).
28. A. Mohammad, I. Ahmed, and Y. Ahmed. Measurement of Uranium Concentration in Some Soil Samples in Jalawla'a City Using CR-39 Detector. *Al-Nahrain Journal of Science* 16(1): 112–116 (2013).
29. T.M. Salman and M.A. Algrifi. Measurement of Uranium Concentration in Basrah Soils Using the CR-39 Detector. *Biomedicine and Chemical Sciences* 1(3): 164–167 (2022).
30. M.A. Algrifi and T.M. Salman. Measuring uranium concentration in Um Qasr district, southern Iraq, in two different ways. *Applied Radiation and Isotopes* 192: 110595 (2023).

Proceedings of the Pakistan Academy of Sciences: A Physical and Computational Sciences 61(4): 325-330 (2024)

ISSN (Print): 2518-4245; ISSN (Online): 2518-4253
http://doi.org/10.53560/PPASA(61-4)678

Pakistan Academy of Sciences

Research Article

Theoretical Evaluation of Silicon Crystal Growth Using Gallium Solvent

Alijon Razzokov[1] and Khushnudbek Eshchanov[2*]

[1]Department of Physics, Urgench State University, Urgench, Uzbekistan
[2]Department of Chemistry, Urgench State University, Urgench, Uzbekistan

Abstract: Semiconductor materials are of great importance throughout the world. Silicon crystals are this field's most widely used and relatively inexpensive material. Obtaining low-dislocation and defect-free silicon crystals is one of the current issues, and we theoretically investigated the production of low-defect silicon crystals from silicon-gallium melt. We considered the defects that appear in the silicon crystals grown from the solution related to the large-sized silicon nanoclusters involved in the crystal formation based on the obtained results, we showed the conditions for obtaining silicon crystals with few defects from the silicon-gallium solution.

Keywords: Silicon, Defect, Nanocluster, Solution, Gallium.

1. INTRODUCTION

Obtaining semiconductor materials under uniform technological conditions has been of great importance. Since producing semiconductor crystals from liquid solutions is carried out at lower temperatures than other methods, energy consumption is low and environmentally friendly. The liquid phase growth method is promising for obtaining thin epitaxial layers and multilayer structures. However, in most cases, it is observed that the dislocation density is high and there are more defects on the surface of the formed crystals. Many solvent materials have been used to grow Si and Si-containing solid solution semiconductor crystals. To clean Si crystals in production processes, it was studied to obtain silicon crystals from Si-Al solution. However, the results showed that there were defects on the surface of the obtained Si crystals, and it was known that Al was included in the composition [1]. Si crystals were grown from a solution of Si in Na metal at low temperatures. In this case, Na metal in the solution was vaporized at temperatures of 1173 K and below, saturating the solution and obtaining Si single crystals [2]. The main advantage of the solution growth method is that the crystals grow at temperatures below the melting temperature and the crystal growth occurs spontaneously through nucleation or crystallization. On the other hand, crystal growth in solution is much slower [3]. Due to the small density difference in the Si-Fe solution, it is difficult to separate Si from the solution. In the Si-Cu solution, Cu and Si can form intermediates during directional crystallization, which makes it difficult to remove Cu from Si [4-8]. Therefore, effective solvents that are useful for Si growth rate, benefaction, and purification are in high demand.

It has been studied that the growth of Si crystals using Ga-Si, Au-Si and Ag-Si solutions can prevent the introduction of polluting additives metals such as Ni, Co, Fe and Cr into the crystal structure [9]. Studies on the effect of gallium (Ga) doping on Czochralski (CZ) Si crystal growth have also been carried out. When Ga was directly added to molten Si, only a few clusters of Ga atoms were detected from the surface of the Si solution during crystal growth. It was confirmed that Ga concentration is very small in millimeteres measurements made in several steps along the direction of crystal growth [10]. Based on these data, we theoretically investigated the formation mechanisms of Si crystals from Si-Ga melt and the conditions for the formation of low-defect crystals.

Received: July 2024; Revised: November 2024; Accepted: December 2024
* Corresponding Author: Khushnudbek Eshchanov <xushnudbek.e@urdu.uz>

2. THEORETICAL PART

The formation of crystals in the solution is related to the saturation of the solution, in which nanoclusters of crystals (formers of crystal centres) play an important role. The nanoclusters formed in the solution unite and cause crystals to grow. Nanoclusters are very active particles that always tend to reduce their surface free energy. Due to this, the merging of nanoclusters and the formation of large aggregates are observed. Determination of the size of nanoclusters formed in a saturated solution is carried out using the Equation (1) [11, 12]:

$$r_c = \frac{2\sigma_{s-l} \cdot V_m}{\Delta G_V} \quad (1)$$

where V_m-molar volume (m^3), σ_{s-l}-specific surface tension at the liquid-solid interface (J/m^2), ΔG_V-volumetric Gibbs energy (J/mol).

The volumetric Gibbs energy (ΔG_V) of nanoclusters in the solution medium is related to the volumetric dimensions of the particles. If the size of the nanocluster is small, the share of its surface Gibbs energy (ΔG_s) will be larger, and the volume Gibbs energy will have a smaller contribution. As the size of the nanocluster increases, the percentage of volumetric Gibbs energy increases. Volumetric Gibbs energy values are determined using the Equation (2) [11].

$$\Delta G_V = \frac{\Delta H_f \cdot (T_l - T)}{T_l} \quad (2)$$

where, ΔH_f is the heat of fusion (J/mol), T_l is the temperature of liquefaction (K), and T is the temperature of nanocluster formation (K).

It is important to determine the ratio of concentrations of nanoclusters formed at temperature T in the solution environment to large-sized particles. The higher the concentration of nanoclusters in the medium, the less defective the crystal formed from their fusion is. The ratio of the concentrations of particles in the environment of the concentrations of large particles is determined by Equation (3) [12].

$$r = \frac{2\sigma_{s-l} V_m}{RT \ln \frac{C_r}{C_\infty}} \quad (3)$$

In the equation, R is the universal gas constant (8.314 $J \cdot K^{-1} \cdot mol^{-1}$), r is the radius of the nanocluster (m), C_r is the concentration of nanoclusters with radius r, and C_∞ is the concentration of large-sized particles.

The process of crystallization from a solution and the processes of melting (mixing of solution components) are interdependent. As mentioned above, nanoclusters are directly involved in the crystallization process, and it is important to know the Gibbs energies of their formation. The interdependence between the maximum Gibbs energy of formation ($\Delta G_{max,cr}$) and the Gibbs energy of mixing (ΔG_{mix}) of nanoclusters in the medium determines the Gibbs energy of this system. The highlighted parameters are determined as follows [13, 14].

$$\Delta G_{mix} = RT(X_1 \ln X_1 + X_2 \ln X_2) \quad (4)$$

$$\Delta S_{mix} = -R(X_1 \ln X_1 + X_1 \ln X_2) \quad (5)$$

$$\Delta G_{max,\,cr} = \frac{16\pi\sigma_{s-l}{}^3 V_m^2}{3\Delta G_V{}^2} \quad (6)$$

$$\Delta G_{sistem} = \Delta G_{max,cr} + \Delta G_{mix,then} - \Delta G_{mix,first} \quad (7)$$

where, ΔG_{mix}-mixing Gibbs energy (J/mol), ΔS_{mix}-entropy of mixing ($J \cdot mol^{-1} \cdot K^{-1}$) X-mol fraction, $\Delta G_{max,cr}$ - maximum formation Gibbs energy (J/mol).

The temperature at which the change in the Gibbs energy of the system is the smallest can be considered the energetically optimal temperature of the crystallization process.Carrying out the process under conditions with a lower value of Gibbs energy results in the least consumption of energy. Therefore, it is important to determine the Gibbs energy of the system. The size of the defects that can be formed on the surface of the crystals forming in the solution determines the quality of the crystal. Equation (8) can be used to determine defect sizes (b) on the crystal surface [12].

$$\Delta G_{max,cr} = \frac{4\sigma_{s-l} b V_m}{\Delta G_V} \quad (8)$$

Using the above information, we can determine the conditions for growing crystals with few dislocations and few defects from the solution.

3. RESULTS AND DISCUSSION

Since the solubility of silicon (Si) in gallium (Ga) is very good, it is important to grow Si and Si-containing crystals from this solution. It should also be noted that Ga does not contaminate growing Si crystals. In our previous papers, we have published information about the participation and importance of nanoclusters in the medium in crystal growth from solutions [15, 16]. The defect-free surface of the crystals growing from the solution is also related to the amount of nanoclusters of the same size participating in the process. Therefore, it is important to determine the sizes and quantitative indicators of nanoclusters involved in the crystallization process. We determined the radius of the nanoclusters involved in the crystallization process at temperatures of 873-1273 K (Figure1).

In the growth of a Si crystal from a solution of Si in Ga, the difference in the size of the nanoclusters in the solution causes defects on the surface of the crystal. The presence of nanoclusters in the crystal growth, and the fact that they are the same and smaller in size, or that there are few differences between their sizes, creates the possibility of obtaining a crystal with fewer defects.

At higher temperatures, the sizes of Si nanoclusters become larger. Large-sized nanoclusters lead to an increase in defects in the growing crystal. Therefore, we considered the maximum temperature to study the crystallization process to be 1273 K. We determined the changes in the sizes of Si nanoclusters formed in the solution of Si in Ga depending on different temperatures. Depending on the temperature, the size of Si nanoclusters in the solution corresponded to the appearance of a polynomial function. At temperatures below 1073 K, the difference between the sizes of Si nanoclusters was observed to be small. In studies, we have published the results of experiments determining the sizes of Si and Ge nanoclusters dissolved in Sn solvent. In these studies, we showed that the size of Si and Ge nanoclusters decreased with a decrease in temperature [15, 17]. If Si crystals are grown from a Ga-Si solution starting from a temperature of 1073 K, the probability of obtaining perfectly crystalline films is high. We used the activity parameters used for real processes to explain the crystallization process in the Si-Ga solution more precisely. It will be possible to obtain results closer to real systems through the activity (a) parameters of the components in the solution. For this purpose, we determined and used the activities of Si and Ga components [18] based on the literature.

When considering the processes of crystallization in solutions, it is important to determine the Gibbs energy of mixing (ΔG_{mix}). To determine the Gibbs energy of mixing for real systems, we use the following equation [19]:

$$\Delta G_{mix} = RT(X_{Si}\ln a_{Si} + X_{Ga}\ln a_{Ga}) \qquad (9)$$

where, X_{Si} and X_{Ga} are the mole fractions of silicon and gallium, and a_{Si} and a_{Ga} are their activities.

Using Equation (9), the Gibbs energies of mixing for a real solution of Si-Ga were calculated. In the process of cooling the Si-Ga solution, it was found that the Gibbs energy of mixing of the system increases in a curved form depending on the temperature (Figure 2).

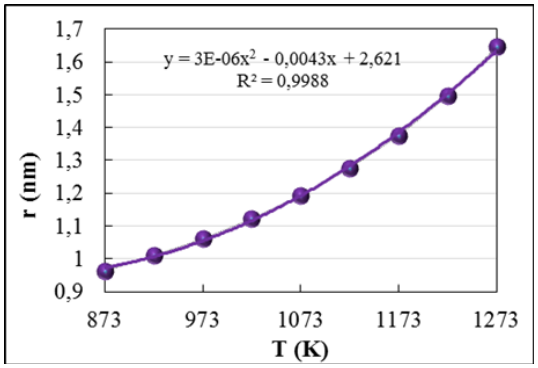

Fig. 1. Temperature dependence of the sizes of Si nanoclusters in the Si-Ga solution.

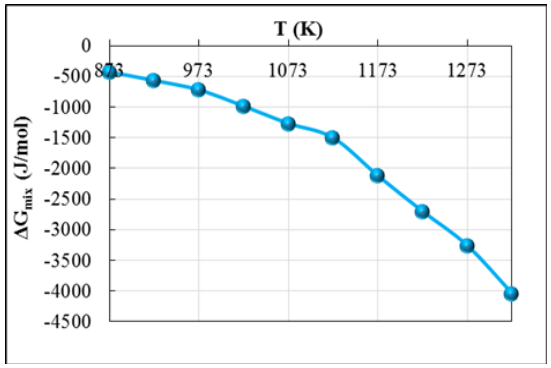

Fig. 2. Temperature dependence of the Gibbs energy of mixing of Si and Ga.

The increase in the Gibbs energy of mixing at lower temperatures causes a decrease in the solubility property in this situation. In such cases, the solute is more likely to separate from the solution by forming crystals. When the entropy of mixing (ΔS_{mix}) change of the components in the solution was studied, the value of ΔS_{mix} decreased with decreasing temperature (Figure 3). Decreasing the value of ΔS_{mix} means reducing the disorder level of components in the system. In such a situation, the probability of the transition of particles from disorder states to order states increases.

$$\Delta S_{mix} = -R(X_{si}\ln a_{Si} + X_{Ga}\ln a_{Ga}) \qquad (10)$$

By determining the Gibbs energies of the maximum formation of Si nanoclusters in the solution, it is possible to determine the results of the total Gibbs energy of the process system (ΔG_{sis}). We used Equation (6) to determine the Gibbs energy of the maximum formation of nanoclusters. Based on the obtained results, a temperature dependence graph of maximum Gibbs energy of Si nanoclusters formed in Ga medium was drawn and attention was paid to the changes. Changes in the graph showed that the Gibbs energy changes exponentially from 1273 K to 1073 K as the temperature decreases. As the temperature decreases from 1073 K to 873 K, a linear change of Gibbs energy is observed (Figure 4). The change in the Gibbs energy of the solution system was found by subtracting the differences between the initial and final values of the Gibbs energies of mixing from the maximum Gibbs energy of the nanoclusters causing crystallization (Equation (7)).

In the process of growing Si crystals from the Si-Ga solution, the temperature dependence graph of the Gibbs energy of the system can be divided into 2 parts. In the temperature range of 873-1073 K, it was observed that the change of Gibbs energy of the system is linearly dependent on temperature, and at temperatures of 1073-1273 K, it is exponential (Figure 5). During the growth of Si from the solution, the temperatures in the states of linear variation of the Gibbs energy of the system are important. Because the Gibbs energy of the system changes linearly (depending on the temperature), the energy differences at each process stage are smaller.

Using the results obtained above, the ratio of the concentration of nanoclusters in the Si-Ga solution to the concentration of large particles was determined (using Equation (3)). It was found that the concentration of Si nanoclusters with the radius r in the solution increases with the decrease in temperature (Figure 6). This means that at low temperatures, the concentration of nanoclusters is greater than that of large-sized particles.

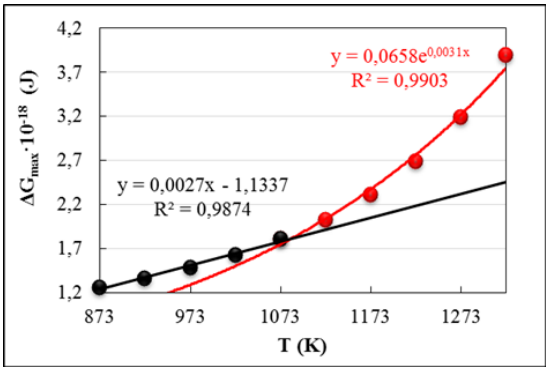

Fig. 4. Temperature dependence of maximum Gibbs energies of Si nanoclusters.

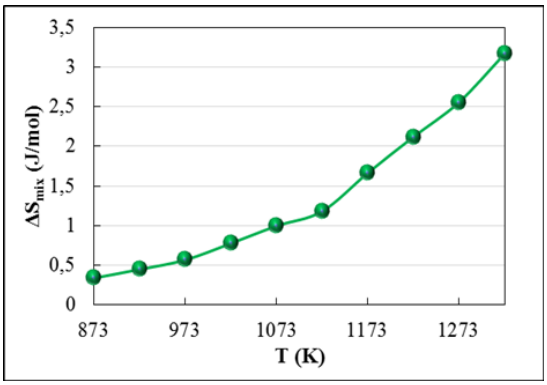

Fig. 3. Temperature dependence of the entropy change of mixing Si and Ga.

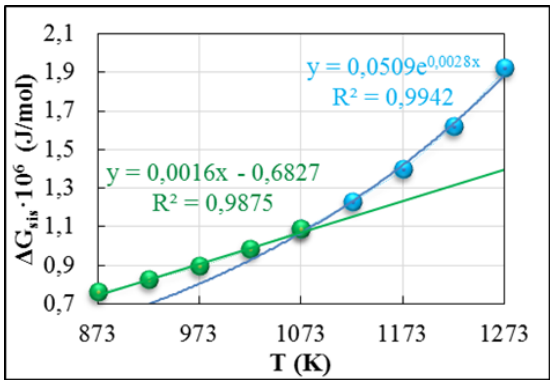

Fig. 5. Gibbs energy change of the system during the growth of Si crystals from Si-Ga solution.

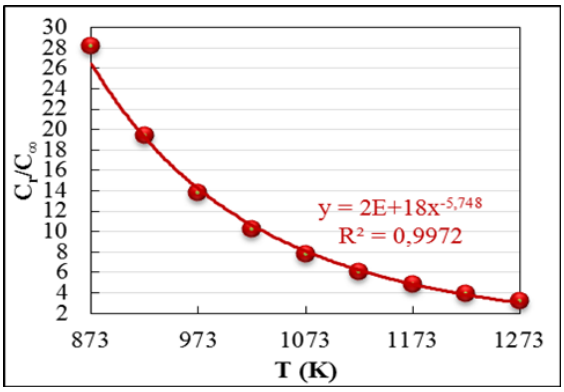

Fig. 6. The ratio of the concentrations of Si nanoclusters at different temperatures to the concentrations of large particles in the solution.

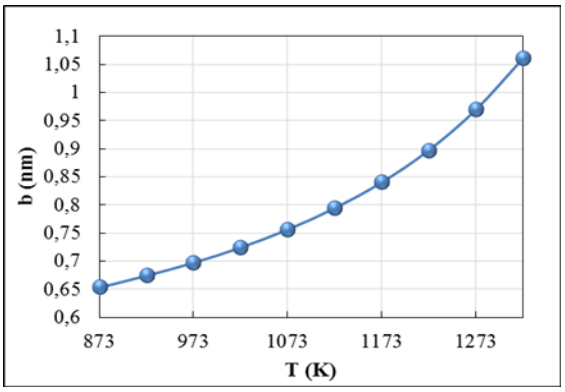

Fig. 7. 2D dimensions that can be formed on the surface of Si crystals growing from a Si-Ga solution.

If we pay attention to all the determined results, it can be seen that as the temperature decreases, the size of Si nanoclusters in the solution decreases and their concentration increases. This situation can allow obtaining Si crystals with fewer defects (less dislocations) from the Si-Ga solution. Dislocations that appear on the surface of the crystal are related to defects on the surface.

Studying the sizes of initial 2D defects that appear on its surface during crystal growth helps to determine the conditions under which crystals with fewer defects can be obtained. The size of the defects formed on the surface of the Si crystal growing from the Si-Ga solution is depicted in the temperature dependence graph (Figure 7). The sizes of these defects are determined using Equation (8).

If we pay attention to the results, it can be seen that the sizes of 2D defects formed on the surface of Si crystals growing in Si-Ga solution are small. The size of the defect was around 1 nm at 1323 K and at temperatures below 1273 K, the size of nanoclusters decreased sharply below 1 nm. These indicators show that obtaining Si and Si-containing crystals in Ga solvent is possible with few dislocations and defects.

4. CONCLUSIONS

The possibilities of growing Si crystals from liquid Si-Ga solution were considered. The results of the study showed that the size of the nanoclusters involved in the crystallization process becomes relatively small with the decrease in temperature, and the defects on the surface of the crystals growing from this solution are very likely to be very small. It was found that the concentration of nanoclusters increases as the temperature decreases. Based on these results, it can be concluded that the use of Ga solvent is very promising for obtaining crystals with low dislocation density and few defects and semiconductor structures based on them.

5. CONFLICT OF INTEREST

The authors declare no conflict on interest.

6. REFERENCES

1. Y. Nishi, Y. Kang, and K. Morita. Control of Si crystal growth during solidification of Si-Al melt. *Materials Transactions* 51(7): 1227-1230 (2010).
2. H. Morito. Low-temperature synthesis of Si and Si-based compounds using Na. *Journal of the Ceramic Society of Japan* 122(1432): 971-975 (2014).
3. I. Milisavljevic and Y. Wu. Current status of solid-state single crystal growth. *BMC Materials* 2: 2 (2020).
4. G. Qian, L. Zhou, S. Li, Z. Wang, and L. Sun. Enhanced In Situ Separation of Boron at the Silicon Alloy Solidification Interface through Innovating the Impurity Chemical Reconstruction Approach for SoG-Si. *ACS Sustainable Chemistry & Engineering* 9(33): 11179-11193 (2021).
5. G. Qian, L. Sun, H. Chen, Z. Wang, K. Wei, and W. Ma. Enhancing impurities removal from Si by controlling crystal growth in directional solidification refining with Al–Si alloy. *Journal of Alloys and Compounds* 820: 153300 (2020).
6. L. Sun, Z. Wang, H. Chen, D. Wang, and G. Qian. Removal of phosphorus in silicon by the formation of $CaAl_2Si_2$ phase at the solidification interface. *Metallurgical and Materials Transactions B* 48:

420-428 (2017).
7. L. Hu, Z. Wang, X. Gong, Z. Guo, and H. Zhang. Impurities removal from metallurgical-grade silicon by combined Sn-Si and Al-Si refining processes. *Metallurgical and Materials Transactions B* 44: 828-836 (2013).
8. L. Hu, Z. Wang, X. Gong, Z. Guo, and H. Zhang. Purification of metallurgical-grade silicon by Sn–Si refining system with calcium addition. *Separation and Purification Technology* 118: 699-703 (2013).
9. E.A. Good, T.H. Wang, T.F. Ciszek, R.H. Frost, M.R. Page, and M.D. Landry. Partitioning effects in recrystallization of silicon from silicon-metal solutions. In: 12th Workshop on Crystalline Silicon Solar Cell Materials and Processes. *August 11-14, 2002, Breckenridge, Colorado* (2002).
10. T. Hoshikawa, T. Taishi, S. Oishi, and K. Hoshikawa. Investigation of methods for doping CZ silicon with gallium. *Journal of Crystal Growth* 275(1-2): e2141-e2145 (2005).
11. P. Rudolph. Thermodynamic Fundamentals of Phase Transitions Applied to Crystal Growth Processes. In: Crystal growth Technology. H.J. Scheel and T. Fukuda (Eds.). *John Wiley & Sons, New York* pp. 15-42 (2003).
12. E.D. Shchukin, A.V. Pertsov, E.A. Amelina, and A.S. Zelenev (Eds.). Colloid and Surface Chemistry. *Elsevier Science* (2001).
13. D.R. Gaskell and D.E. Laughlin (Eds.). Introduction to the Thermodynamics of Materials. 6th Edition. *CRC Press, Boca Raton* (2017).
14. A.D. Pelton (Ed.). Phase Diagrams and Thermodynamic Modeling of Solutions. *Elsevier, München* (2019).
15. A. Razzokov and K. Eshchanov. Thermodynamic Bases for Obtaining Crystalline Perfect Silicon from Tin-silicon Solution. *International Journal of Thermodynamics* 25(2): 1-6 (2022).
16. A. Razzokov and K. Eshchanov. Optimal Regime for Growth of Epitaxial Germanium Layers from the Liquid Phase Based on Thermodynamic Calculations. *International Journal of Thermodynamics* 25(3): 41-45 (2022).
17. A.S. Razzokov, A.S. Saidov, V.V. Girzhon, and O.V. Smolyakov. Features of growing Si- and $Si_{1-x}Ge_x$-single-crystal films from solution-melt based on tin. *Journal of Physical Studies* 26(4): 4601-4605 (2022).
18. J. Safarian, L. Kolbeinsen, and M. Tangstad. Thermodynamic activities in silicon binary melts. *Journal of Materials Science* 47: 5561-5580 (2012).
19. P.W. Atkins and J. de Paula (Eds.). Atkins' Physical Chemistry. Eighth Edition. *W.H. Freeman and Company, New York* (2006).

Proceedings of the Pakistan Academy of Sciences: A Physical and Computational Sciences 61(4): 331-337 (2024)

ISSN (Print): 2518-4245; ISSN (Online): 2518-4253
http://doi.org/10.53560/PPASA(61-4)876

Pakistan Academy of Sciences

Research Article

Atomistic Simulation of Temperature-Dependent Interfacial Diffusion between Solid Nickel and Liquid Aluminum

Alzais Safii[1], Yoyok Winardi[1], Sudarno[1], Desriyanti[2], Norhasnidawani Johari[3], Ali Selamat[3], and Rizal Arifin[1,2]*

[1]Department of Mechanical Engineering, Universitas Muhammadiyah Ponorogo, Ponorogo, Indonesia

[2]Department of Electrical Engineering, Universitas Muhammadiyah Ponorogo, Ponorogo, Indonesia

[3]Malaysia-Japan International Institute of Technology, Universiti Teknologi Malaysia, Kuala Lumpur, Malaysia

Abstract: The performance and durability of welded joints are directly influenced by interfacial diffusion between the metals involved, making it essential to investigate the effect of temperature on these processes. The present research examines temperature-dependent diffusion mechanisms at the interface between solid nickel and liquid aluminum using molecular dynamics simulations. Investigations were conducted at 1200, 1300, 1400, and 1500 K to explore the influence of temperature on atomic mobility and interfacial mixing. Radial distribution function analysis revealed a significant increase in the diffusion of nickel atoms into the aluminum phase with increasing temperature, indicating enhanced atomic interactions at the interface. The mean square displacement analysis supported these findings, showing that aluminum atoms were more mobile than nickel atoms at lower temperatures, while nickel atoms exhibited a faster diffusion rate with increasing temperature, surpassing aluminum in mobility. This trend is reflected in the diffusion coefficients, which exhibit a temperature-dependent increase in the diffusion rate of the nickel atoms. These results emphasize the role of temperature in controlling the diffusion dynamics at the solid–liquid interface. The insights gained from this study are critical for optimizing processes, such as dissimilar metal welding, where precise control over interfacial diffusion is essential for achieving the desired material properties and ensuring the structural integrity of nickel–aluminum joints in high-temperature applications.

Keywords: Nickel–Aluminum Interface, Molecular Dynamics Simulation, Interfacial Diffusion, Temperature Dependent Diffusion.

1. INTRODUCTION

The joining of metals with different compositions, melting temperatures, and thermal expansion coefficients is referred to as dissimilar-metal welding. This process is essential in various industries and requires a change in the mechanical properties or performance [1]. The strength of dissimilar metal welds is significantly influenced by the diffusion of weld metals, where the parent metals have dissimilar thermal expansion coefficients [2]. Furthermore, the formation of intermetallic compounds at the weld interface during fusion welding can result in poor strength because of the different chemical and mechanical qualities of the metals involved [3]. Studies have indicated that dissimilar metal welds may produce tensile residual stresses on both the inner and outer surfaces after welding, emphasizing the significance of understanding and managing such stresses for the structural soundness of the joint [4]. Moreover, the microstructure and mechanical properties of dissimilar metal welds can be influenced by welding parameters such as the heat

Received: August 2024; Revised: November 2024; Accepted: December 2024
* Corresponding Author: Rizal Arifin <rarifin@umpo.ac.id>

input, holding time, and post-weld heat treatment [5–7]. Metallurgical compatibility between the interlayer and base metals is crucial when selecting interlayers in dissimilar weld joints because it can have a significant impact on the overall quality and performance of the weld [8, 9]. In addition, the presence of weld residual stresses in dissimilar metal welds, even after post-weld heat treatment, highlights the importance of considering these stresses when evaluating potential welding defects and joint performances [10]. The direction of crack growth in dissimilar metal-welded joints can also influence the fracture toughness and fatigue crack growth rates, underscoring the need to elucidate crack propagation mechanisms in such joints [11].

Solid metal–liquid metal diffusion is of significant interest because of its implications in various fields including materials science, metallurgy, and electrochemistry. This diffusion process, in which atoms move between solid and liquid metals, is essential for processes such as alloy formation, electroextraction, and liquid-metal embrittlement. It should be noted that in the process of atom diffusion between solid and liquid metals, the diffusion coefficients of liquid metals are several times greater than those of solid metals [12], which is attributed to the excited states of the atoms in the liquid phase. The diffusion of metal atoms primarily occurs in the liquid phase rather than in the solid phase, which influences the characteristic contact melting time [13].

The diffusion of nickel and aluminum at the interface is a crucial process in various applications involving these materials; it occurs when atoms from one material move into another, resulting in the formation of intermetallic compounds and altered material properties. This phenomenon is particularly important for nickel and aluminum. Research has revealed considerable variations in the diffusion coefficients of these metals in nickel–aluminum systems. The rapid outward diffusion of nickel, in contrast to the slower inward diffusion of aluminum, led to the formation of Kirkendall voids. This process is commonly referred to as the Kirkendall effect [14] and is responsible for the generation of pores and vacancies within the crystal structure of the material owing to the disparity in diffusion rates. According to previous studies, interfacial diffusion between nickel and aluminum typically results in inward diffusion of aluminum toward the nickel substrate. However, the presence of zirconium causes it to diffuse toward specific layers at the β-NiAl/γ'-Ni_3Al interface, where it can be substituted for aluminum atoms in the β-NiAl phase [15]. This substitution can affect the microstructure and properties of the intermetallic compounds formed at the interface. Furthermore, studies on nickel diffusion in intermetallic compounds have revealed that nickel diffuses through compound layers and dissolves in the aluminum phase at the other end of the couple [16]. This process plays a crucial role in the formation and evolution of intermetallic phases at the nickel–aluminum interface. The role of nickel diffusion in practical applications, such as welding and coating processes, is essential for enhancing the bonding and mechanical properties of joints. In particular, the incorporation of a nickel interlayer can prevent the formation of brittle intermetallic compounds and improve the strength and ductility of joints between dissimilar metals, such as aluminum and steel [17].

Despite extensive research on interfacial diffusion in dissimilar metal systems, the specific mechanisms driving atomic diffusion at solid nickel–liquid aluminum interfaces, particularly at elevated temperatures, remain inadequately understood. Although, Zhang *et al*. [18] employed molecular dynamics (MD) simulations to examine the interfacial diffusion between nickel and aluminum, their research was constrained to a single high-temperature condition of 1200 K. Despite offering valuable insights into diffusion mechanisms, their study did not explore how diffusion coefficients vary with temperature, creating a notable gap in understanding the impact of thermal changes on atomic mobility and interfacial dynamics in the nickel-aluminum system. Our research addresses this limitation by broadening the scope to include simulations at multiple temperatures: 1200, 1300, 1400, and 1500 K. This comprehensive approach allows for a thorough analysis of the diffusion coefficients and their temperature dependence, providing more extensive insights into the interfacial diffusion mechanisms across various thermal conditions. By analyzing the diffusion coefficients and structural evolution of Ni atoms at the interface, this research aims to provide a deeper understanding of how temperature and atomic interactions influence the diffusion processes. The findings of this study will contribute to optimizing

welding techniques and improving the performance of dissimilar metal joints in high-temperature applications, where precise control over diffusion is crucial.

2. SIMULATION DETAILS

Simulations were carried out using the LAMMPS software package [19, 20] to investigate the interfacial diffusion between solid nickel and liquid aluminum. The Embedded Atom Method (EAM) potential parameterized for nickel and aluminum [21] was used to ensure accurate interactions between the nickel and aluminum atoms. The simulation system, with dimensions of 35.2 Å × 35.2 Å × 204.5 Å, comprised 6,400 nickel atoms in a face-centered cubic structure, representing the solid phase, and 6,400 Al atoms as the liquid phase (Figure 1). The temperature dependence of diffusion was studied by conducting simulations at 1200, 1300, 1400, and 1500 K using the NVT ensemble with a Nosé–Hoover thermostat to maintain stability. The Velocity Verlet algorithm was used to integrate the equations of motion with a time step of 1 fs; each simulation was run for a total duration of 1,000,000 fs, allowing sufficient time for the diffusion processes to occur.

Structural analysis and visualization were performed using OVITO [22], allowing for a thorough examination of the atomic structure and interfacial diffusion. The atomic structure of the system was analyzed using the radial distribution function $g(r)$. The radial distribution function was calculated using Equation (1).

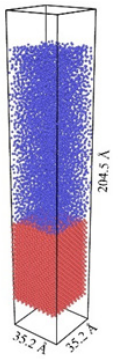

Fig. 1. Initial simulation configuration. The red and blue spheres represent nickel and aluminum atoms, respectively.

$$g(r) = \frac{1}{N}\sum_{i=1}^{N}\frac{n_i(r, r+\Delta r)}{\rho \cdot V(r, r+\Delta r)} \quad (1)$$

Where,

N = Total number of atoms in the system

$n_i(r, r+\Delta r)$ = Number of atoms found within a spherical shell of radius r and thickness Δr around atom i.

ρ = Atomic number density (atoms/Å^3)

$V(r, r+\Delta r)$ = Volume of the spherical shell (Å^3)

The mean square displacement (MSD) of the nickel and aluminum atoms at the interface was calculated from the atomic trajectories to quantify the diffusion behavior. The MSD was calculated using Equation (2).

$$\text{MSD} = \frac{1}{N}\sum_{i=1}^{N}\langle|\vec{r}_i(t) - \vec{r}_i(0)|\rangle \quad (2)$$

Where,

MSD = Mean square displacement (Å^2)

N = The total number of atoms

t = Time (fs)

$\vec{r}_i(t)$ = position of atoms i at time t

$\vec{r}_i(0)$ = position of atoms i at time t = 0

This study specifically focused on interfacial atoms, as they are essential for understanding the diffusion process at the solid–liquid boundary. The diffusion coefficients for nickel and aluminum were estimated from the slope of the plots of MSD versus time, utilizing the Einstein relation for diffusion, as expressed in Equation (3).

$$D = \frac{1}{2d}\lim_{t\to\infty}\frac{MSD}{t} \quad (3)$$

Where,

D = Diffusion coefficient (Å^2/ps)

d = Dimension of the system

3. RESULTS AND DISCUSSION

This section presents and examines the results of MD simulations using visual and quantitative methods. The structural evolution of the nickel–aluminum interface was analyzed to illustrate the diffusion processes at various temperatures. Additionally, we employed the radial distribution function, $g(r)$, to analyze atomic interactions (Figure 2), MSD to quantify atomic mobility, and diffusion coefficients to assess the rate of diffusion.

In Figure 2, $g(r)_{\text{Ni-Al}}$ depicts the distribution of the distances between nickel and aluminum atoms in the system in both the initial and final states of the MD simulations at temperatures of 1200, 1300, 1400, and 1500 K. $g(r)$ is an essential tool for elucidating the local atomic structure and degree of atomic interactions within a material, particularly at the interface between two distinct phases. At the beginning of the simulation, $g(r)_{\text{Ni-Al}}$ exhibits a very low first peak, indicating that only a few nickel atoms are within a close range of aluminum atoms. This initial condition reflects the configuration of the system, in which the nickel atoms are primarily confined to the solid phase and the aluminum atoms are in the liquid phase, with minimal intermixing at the interface. The low intensity of the first peak suggests that the atomic interactions between nickel and aluminum are limited, primarily occurring at the solid–liquid boundary, with most of the atoms remaining in their respective phases**.**

When the temperature is increased to 1200 K, a notable transformation occurred in $g(r)_{\text{Ni-Al}}$ curve. After 10^6 fs, the first $g(r)_{\text{Ni-Al}}$ peak became more pronounced, which indicated that a larger number of nickel atoms moved closer to the aluminum atoms, suggesting an increase in atomic diffusion at the interface. The higher intensity of the first peak at 1200 K suggests greater mobility of atoms at the interface, allowing for greater intermixing between the solid nickel and liquid aluminum phases. The elevated degree of atomic interaction at this temperature arises from enhanced diffusion, resulting in a higher number of nickel atoms coordinating with aluminum atoms.

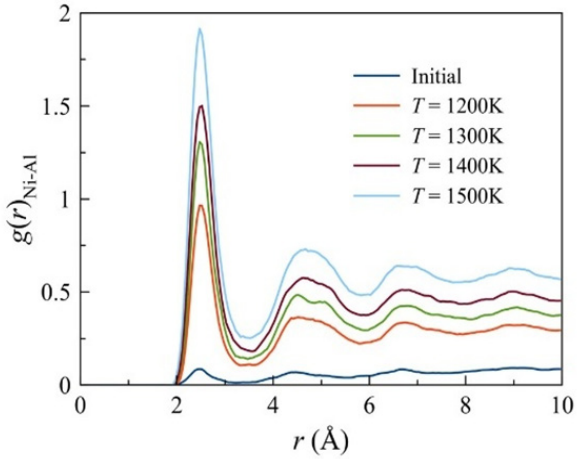

Fig. 2. Radial distribution function, $g(r)_{\text{Ni-Al}}$.

At 1300 K, the diffusion process is further accelerated, as evidenced by the more pronounced first peak of the $g(r)_{\text{Ni-Al}}$ curve. This suggests that more nickel atoms can migrate into the liquid aluminum phase because of the higher thermal energy, which provides the atoms with the necessary kinetic energy to overcome barriers to diffusion. Additionally, the increased peak intensity indicates that the nickel atoms not only entered the aluminum phase but also found more stable positions within the liquid structure, leading to more defined atomic interactions.

At 1400 and 1500 K, the first $g(r)_{\text{Ni-Al}}$ peak exhibits a noteworthy increase in intensity, which suggests that the diffusion of nickel atoms into the aluminum phase becomes more pronounced as the temperature increases. As the temperature increased, the atomic mobility also improved, leading to more significant interfacial mixing and the formation of a more ordered interfacial region. The observed trend indicates that, as the temperature increases, the atoms gain sufficient thermal energy to surmount any remaining diffusion barriers, resulting in a more homogeneous distribution of nickel atoms within the liquid aluminum phase.

Figure 3 validates the results of the $g(r)_{\text{Ni-Al}}$ analysis, demonstrating that higher temperatures lead to increased diffusion of nickel atoms into the liquid aluminum region. As the temperature increased, the kinetic energy of the atoms increased, enhancing their mobility and leading to a

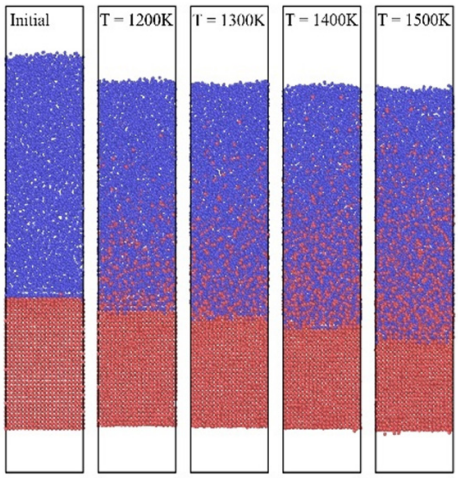

Fig. 3. Snapshots of the initial and final MD configurations. The red and blue spheres represent nickel and aluminum atoms, respectively.

more significant interfacial mixing. This increased diffusion is visually evident in Figure 3, where the simulation snapshots show a greater number of nickel atoms migrating from the solid phase to the liquid phase as the temperature increases from 1200 to 1500 K. Moreover, Figure 3 reveals another critical aspect of the diffusion process: the erosion of nickel layers from the solid phase. Initially, the solid nickel structure in the simulation comprised 32 layers; after 10^6 fs, the number of layers progressively decreased with increasing temperature. At 1200 K, the solid Ni was reduced to 28 layers, indicating the diffusion of four layers of nickel atoms into liquid aluminum. As the temperature increased to 1300 K, the number of Ni layers further decreased to 26, and at 1400 K, only 24 layers remained. At the highest temperature of 1500 K, the solid nickel structure was reduced to 22 layers, indicating significant erosion owing to the high rate of diffusion.

Figure 4 presents the MSD of nickel and aluminum atoms at the solid–liquid interface at various temperatures, including 1200, 1300, 1400, and 1500 K. The MSD curves offer insights into atomic mobility and diffusion behavior under different thermal conditions. At 1200 K, the slope of the curve for nickel atoms at the interface was notably smaller than that for aluminum atoms. This suggests that, at this temperature, aluminum atoms exhibit higher mobility and, consequently, a higher diffusion rate than nickel atoms. This observation is corroborated by the diffusion coefficients presented in Table 1, with a value of 0.23 Å²/ps for aluminum atoms compared to 0.18 Å²/ps for nickel atoms at 1200 K. The higher mobility of aluminum atoms at this lower temperature can be attributed to the liquid state of aluminum, which facilitates atomic movement compared with the more rigid solid structure of nickel. However, as the temperature increases to 1300, 1400, and 1500 K, a reversal in this trend is observed: the MSD curves for nickel atoms at the interface are steeper (with larger slopes) than those for aluminum atoms, indicating a more rapid diffusion of nickel atoms compared to aluminum atoms. This shift is also reflected in the diffusion coefficients listed in Table 1. At 1300 K, the diffusion coefficient for nickel is 0.30 Å²/ps, slightly higher than that of aluminum (0.28 Å²/ps). The difference becomes more pronounced at 1400 and 1500 K, with nickel exhibiting diffusion coefficients of 0.39 and 0.43 Å²/ps, respectively, compared to 0.30 and 0.40 Å²/ps for aluminum. The simulation results indicate that the diffusion

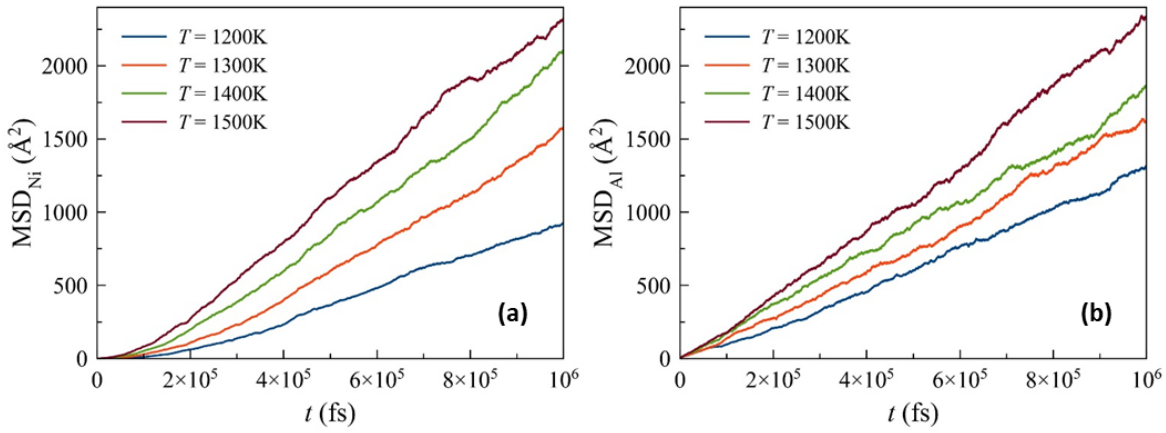

Fig. 4. MSD plots of (a) nickel and (b) aluminum atoms at the surface.

Table 1. Diffusion coefficients of surface atoms at the nickel–aluminum interface.

No.	Temperature (K)	Nickel diffusion coefficient (Å²/ps)	Error (%)	Aluminum diffusion coefficient (Å²/ps)	Error (%)
1	1200	0.18	0.3	0.23	0.2
2	1300	0.30	0.2	0.28	0.5
3	1400	0.39	0.3	0.30	0.4
4	1500	0.43	0.4	0.40	0.4

coefficient of aluminum is lower than its self-diffusion coefficient in pure liquid form (0.88 Å²/ps) [23], which can be attributed to interfacial effects at the solid nickel-liquid aluminum boundary. In the pure liquid state, aluminum atoms exhibit higher mobility in a homogeneous environment. However, at the nickel-aluminum interface, aluminum atoms interact with nickel atoms, creating a nonhomogeneous environment that constrains their movement. These interactions, in conjunction with the ordered structure induced by the solid nickel substrate, increase the energy barriers for diffusion and decrease atomic motion. Consequently, the interfacial dynamics significantly reduce the effective diffusion of aluminum compared with its behavior in a pure liquid state.

The results indicate that increasing the temperature increases the thermal energy available to the nickel atoms, which surpasses the energy barriers associated with diffusion and leads to increased atomic mobility. Elevated temperatures result in higher diffusion rates for nickel atoms and their stronger inclination to migrate into the liquid aluminum phase, leading to enhanced interfacial mixing and structural changes. These findings align with those of previous studies conducted on liquid metal systems such as liquid nickel and liquid titanium, where nickel displayed a higher diffusion coefficient than titanium [24]. The results of the present study highlight the significance of controlling the temperature during processing to ensure optimal material properties as well as the critical role of elevated temperatures in influencing the stability and performance of dissimilar metal interfaces under various thermal conditions.

4. CONCLUSIONS

This study investigated the diffusion dynamics at the interface between solid nickel and liquid aluminum via MD simulations at temperatures ranging from 1200 K to 1500 K. The results showed that, as the temperature increased, the diffusion of nickel atoms into the aluminum phase became more pronounced, leading to enhanced interfacial mixing. The $g(r)_{\text{Ni-Al}}$ analysis indicates a significant increase in atomic interactions at higher temperatures, correlating with the greater mobility of nickel atoms observed in the MSD analysis. At lower temperatures, aluminum atoms exhibit more mobility, but as the temperature increases, nickel atoms display faster diffusion, surpassing aluminum in mobility. This shift is reflected in the diffusion coefficients, indicating the temperature-dependent acceleration of nickel atom diffusion. These findings highlight the critical role of temperature in controlling atomic diffusion at the solid–liquid interface and have implications for processes such as dissimilar metal welding.

5. ACKNOWLEDGEMENTS

The authors thank Universitas Muhammadiyah Ponorogo and Universiti Teknologi Malaysia for their support.

6. CONFLICT OF INTEREST

The authors declare that they have no conflicts of interest.

7. REFERENCES

1. B. Belkessa, D. Miroud, B. Cheniti, N. Ouali, M. Hakem, and M. Djama. Dissimilar Welding Between 2205 Duplex Stainless Steel and API X52 High Strength Low Alloy Steel. *Diffusion Foundations* 18: 7–13 (2018).
2. R. Chaudhari and A. Ingle. An Empirical Research on Dissimilar Metal Weld of SA335 P11and SA312 TP304 Formed by Metal Inert Gas (MIG) Welding. *International Journal of Recent Technology and Engineering* 8(2): 5008–5012 (2019).
3. S. Murugan, P. Sathiya, and A.N. Haq. Rotary Friction Welding and Dissimilar Metal Joining of Aluminium and Stainless Steel Alloys. *Annals of Dunarea De Jos University of Galati Fascicle Xii Welding Equipment and Technology* 32(1): 85–92 (2021).
4. W. Dong, D. Gao, and S. Lu. Numerical Investigation on Residual Stresses of the Safe-End/ Nozzle Dissimilar Metal Welded Joint in CAP1400 Nuclear Power Plants. *Acta Metallurgica Sinica (English Letters)* 32: 618–628 (2018).
5. S. Ismadi. Study Effect of Holding Time at Post Weld Heat Treatment (PWHT) on Joint Dissimilar Welding ASTM 335 P11 to ASTM 304L Under Controlled Condition. *Key Engineering Materials* 975: 9–20 (2024).
6. M.A. Hayatu, E.T. Dauda, O. Aponbiede, K.A. Bello, and U. Abdullahi. Evaluation of Microstructure and Impact Toughness of Shielded Metal Arc Dissimilar Weldments of High Strength Low Alloy Steel and Austenitic Stainless Steel. *Fuoye Journal of Engineering and Technology* 5(2): 171–174 (2020).
7. M. El-Shennawy, H.A. Abdel-Aleem, M.M.

Ghanem, and A.M. Sehsah. Effect of Welding Parameters on Microstructure and Mechanical Properties of Dissimilar AISI 304 / Ductile Cast Iron Fusion Welded Joints. *Scientific Reports* 14: 19827 (2024).

8. R.R. Gabbasov, E.V. Galieva, E.Y. Klassman, and V.A. Valitov. Effect of pressure welding temperature on the microstructure and mechanical properties of solid-state joints of wrought nickel-based EK79 and EP975 superalloys. *Letters on Materials* 14(2): 155–160 (2024).
9. A.U. Rehman, N.K. Babu, M.K. Talari, S. Anwar, Y. Usmani, and A.M. Al-Samhan. Dissimilar Rotary Friction Welding of Inconel 718 to F22 Using Inconel 625 Interlayer. *Applied Sciences* 11(22): 10684 (2021).
10. B. Spisák, Z. Bézi, and S. Szávai. Study of the Stress State of a Dissimilar Metal Weld Due to Manufacturing and Operational Conditions. *Periodica Polytechnica Mechanical Engineering* 66(2): 120–128 (2022).
11. T. Saju and M. Velu. Analysis of Fracture Toughness and Fatigue Crack Growth Rates of Electron Beam-Welded Dissimilar Nickel-Based Superalloys: Mode-I Cracks Oriented Normal to the Weld. *Proceedings of the Institution of Mechanical Engineers Part L Journal of Materials Design and Applications* 237(8): 1699–1714 (2023).
12. O.B. Girin. Review-Electrochemical Phase Formation via a Supercooled Liquid State Stage: Metastable Structures and Intermediate Phases. *Journal of the Electrochemical Society* 169(9): 092511 (2022).
13. A.V. Melkikh. Contact Melting of Metals Explained via the Theory of Quasi-Liquid Layer. *Applied Sciences* 11(1): 51 (2021).
14. M. Zagula-Yavorska, J. Morgiel, J. Romanowska, and J. Sieniawski. Nanoparticles in Zirconium-Doped Aluminide Coatings. *Materials Letters* 139: 50–54 (2015).
15. J. Romanowska, M. Zagula-Yavorska, M. Góral, and J. Sieniawski. Zirconium Modified Aluminide Coatings Obtained by the CVD Method. *Solid State Phenomena* 227: 174–177 (2015).
16. M. Khieokae, R. Hanamornroongruang, R. Ramasoot, A. Taechakaesaree, P. Ngamchaliew, and T. Luangvaranunt. Diffusion Coefficient of Nickel in Ni_2Al_3 Intermetallic Compound. *Advanced Materials Research* 1025–1026: 731–736 (2014).
17. Z. Nurisna, A. Supriyanto, N. Muhayat, and T. Triyono. Thermal Spray Application on the Dissimilar Metals Weld Between Aluminum and Steel. *Defect and Diffusion Forum* 402: 27–32 (2020).
18. C. Zhang, H. Wang, and Y. Qiu. Study of Ni/Al Interface Diffusion by Molecular Dynamics Simulation. *Engineering* 3(3): 227–232 (2011).
19. S.J. Plimpton. Fast Parallel Algorithms for Short-Range Molecular Dynamics. *Journal of Computational Physics* 117(1): 1–19 (1995).
20. A.P. Thompson, H.M. Aktulga, R. Berger, D. Bolintineanu, M.W. Brown, P.S. Crozier, P.J. in ‘t Veld, A. Kohlmeyer, S.G. Moore, T.D. Nguyen, R. Shan, M.J. Stevens, J. Tranchida, C. Trott, and S.J. Plimpton. LAMMPS - a flexible simulation tool for particle-based materials modeling at the atomic, meso, and continuum scales. *Computer Physics Communications* 271: 108171 (2022).
21. G.P. Purja Pun and Y. Mishin. Development of an interatomic potential for the Ni-Al system. *Philosophical Magazine* 89(34-36): 3245–3267 (2009).
22. A. Stukowski. Visualization and analysis of atomistic simulation data with OVITO–the Open Visualization Tool. *Modelling and Simulation in Materials Science and Engineering* 18: 015012 (2009).
23. F. Kargl, H. Weis, T. Unruh, and A. Meyer. Self diffusion in liquid aluminium. *Journal of Physics: Conference Series* 340: 012077 (2012).
24. R. Arifin, Y. Winardi, Y.A. Wicaksono, L. Poriwikawa, Darminto, A. Selamat, W.T. Putra, and M. Malyadi. Atomic diffusion at the Ni–Ti liquid interface using molecular dynamics simulations. *Canadian Metallurgical Quarterly* 61(3): 359–365 (2022).

Proceedings of the Pakistan Academy of Sciences: A Physical and Computational Sciences 61(4): 339-347 (2024)

ISSN (Print): 2518-4245; ISSN (Online): 2518-4253
http://doi.org/10.53560/PPASA(61-4)682

Pakistan Academy of Sciences

Research Article

Uranium, Polonium-218, and Polonium-214 Concentrations in Serum Samples of Cancer Patients at Al-Najaf Governorate

Talib A. Abdulwahid[1], Ali Abid Abojassim[1*], Abdulhussein A. Alkufi[2], and Hussien Abid Ali Mraity[1]

[1]Department of Physics, Faculty of Science, University of Kufa, Najaf, Iraq
[2]Education Directorate of Najaf, Ministry of Education, Al-Najaf, Iraq

Abstract: This research examines the concentrations of uranium (U_C), polonium of POW (^{218}Po and ^{214}Po on the wall of the irradiation container), and polonium of POS (^{218}Po and ^{214}Po on the surface of the irradiation container) in serum samples of male and female cancer patients and human health in the Al-Najaf Governorate of Iraq. U_C, ^{218}Po, and ^{214}Po were determined using a track detector technique with a CR-39 detector. The mean values of U_C for male and female cancer patients were 0.110 ± 0.024 ppb and 0.099 ± 0.013 ppb, respectively. The POW's average values for male and female cancer patients were 3.885 ± 2.132 Bqm^{-3} and 2.958 ± 1.146 Bqm^{-3}, respectively while the mean values of POS for male and female cancer patients were 0.702 ± 0.386 Bqm^{-3} and 0.535 ± 0.207 Bqm^{-3}, respectively. The results show that the mean concentrations of U_C, ^{218}Po, and ^{214}Po are significantly higher ($p < 0.001$) in male and female cancer patient groups compared with the healthy group. Also, the mean values of U_C, ^{218}Po, and ^{214}Po concentrations do not correlate with variables for male and female patient groups. Therefore, the concentrations of U_C, ^{218}Po, and ^{214}Po in cancer patients and healthy groups in the present study were not significant in terms of gender. According to the ICRP and WHO report, the concentrations of uranium and polonium in all samples of the current study were within the accepted limits (uranium = 0.810 ppb) and (polonium = 550 Bqm^{-3}), So the serum samples of male and female cancer patients and healthy in the Al-Najaf Governorate of Iraq were not contaminated with uranium.

Keywords: Uranium, Polonium, Blood Serum Radioactivity, Cancer, Irradiation Container, NTDs, Iraq.

1. INTRODUCTION

Essentially, people are exposed to two different types of radiation sources: natural and man-made. While the first source includes terrestrial endogenous radiation, the second source is manmade. In the two situations indicated above, radionuclides are essential for the emission of alpha or beta particles. Through eating or inhalation, these tiny particles may enter the human body [1]. Many radionuclides undergo decay by the emission of alpha (α) particles. The radiological characteristics of these radionuclides must be accurately assessed, particularly regarding their impact on human health [2]. Their existence in human bones, blood, and other tissues induces several health difficulties, including cancer, renal failure, dermatological conditions, a rise in chromosomal abnormalities in live cells, and congenital anomalies [3, 4]. Uranium is a dense, silver-hued radioactive element that is widely found in the Earth's crust and has both radioactive and poisonous properties. It is an element that is known to occur naturally. It includes three isotopes (^{238}U, ^{235}U, and ^{234}U). The latter isotopes, mostly, emit alpha particles, along with some emissions of beta and gamma rays [5]. The daily intake of uranium by the human body comes from water, air, and food, with the latter being the predominant source [6]. Uranium is very hazardous, capable of being ingested and absorbed by the gastrointestinal tract, thereafter entering the circulation upon entering the human body. The radioactive together with the corresponding toxicological properties of uranium and its radioactive isotopes make them a major source of pollution, presenting a risk to both human health and the environment too [7]. The

Received: September 2024; Revised: November 2024; Accepted: December 2024
* Corresponding Author: Ali Abid Abojassim <ali.alhameedawi@uokufa.edu.iq>

World Health Organization (WHO) stipulates that the permissible intake (daily basis) of uranium is around 0.6 μg/kg of body mass. Healthy individuals generally excrete quantity of uranium, on daily basis, in their urine between 0.01 μg and 0.4 μg, depending on their dietary intake [8, 9]. Uranium trace analysis in blood samples is expected to supply with a reliable estimation of the concentration of heavy metals in specific tissues of the body [10]. Uranium accumulation in bones and other organs is later discharged into the blood circulation, resulting in many health issues, including cancer, renal failure, respiratory ailments, congenital anomalies, dermatological conditions, and other unidentified illnesses [7]. Radon is released during the radioactive decay process of uranium-238. Radium-226, its progenitor radionuclide, generates alpha particles that energize it. Upon disintegration into its daughter isotopes, ^{218}Po and ^{214}Po, it emits alpha particles [11, 12]. The distribution of radon varies by geography. Two alpha-emitting decay products, namely ^{218}Po and ^{214}Po, provide the bulk of the radiogenic dosage and have been recognized as the principal cause of radon-induced cancer [13]. Upon inhalation, radon gas infiltrates the lungs and then disseminates throughout the body via the bloodstream, which transports it to other organs. Epidemiological studies are often affected by lifestyle and demographic characteristics; however, in vitro studies have the advantage of removing confounding factors like as smoking and exposure to known or suspected carcinogens [14]. Recently, experts have increasingly revealed that some environmental toxins may play a crucial role in contributing, at least in some instances, to the underlying causes of cancer in both sexes. Given the prevalence of cancer, it is essential to comprehend the risk factors associated with it in human life [15]. Thus, the purpose of this research is to use solid-state nuclear track detectors (CR-39) to assess the levels of alpha emitters such as uranium, ^{218}Po and ^{214}Po in the blood serum of cancer patients in the Governorate of Al-Najaf in the republic of Iraq.

2. MATERIALS AND METHODS

2.1. Sample Collection

The current study was performed on serum samples of male and female cancer patients and healthy humans in the Governorate of Al-Najaf in the republic of Iraq. In 2024, Table 1 provides detailed demographic and clinical information about cancer patients, including their gender, sample code, type of cancer, age, and Body Mass Index (BMI) which can assist in statistical or medical analysis within the present study. The patients' ages range from 20 to 82 years, while BMI values range from 18 to 44. Cancer types vary across the Table, including lung cancer, prostate cancer, breast cancer, leukemia, kidney cancer, skin cancer, and more. There are 15 male and 15 female participants, providing a balanced gender distribution among the patients.

2.2. Sample Preparation

For this study, we obtained blood serum samples from 30 cancer patients aged 20 to 82. Each participant received a unique code, and samples were produced to quantify uranium concentrations, ^{218}Po, and ^{214}Po. Study subjects were mandated to attend the laboratory in which blood samples from the antecubital vein were collected. A professional phlebotomist performed venipuncture at a pathological laboratory in the Governorate of Najaf, collecting and storing 5-6 ml of blood in gel tubes. The latter blood samples were then left to coagulate for 5-10 minutes to enable serum separation during the centrifugation. The apparatus was set to function at a rotating velocity of four thousand revolutions every minute for 3-5 minutes, throughout this period the blood was clearly separated from the studied serum. Every sample was given a unique identification number to indicate for the participant's name. Thereafter, the collected samples of people sera were kept into clean, sterile Eppendorf tubes, each containing one ml, and then to be kept at a specific freezer in preparation for the measuring process [16, 17].

2.3. Irradiation Method

The present study used the Long-term irradiation method [18, 19]. Following the collection and preparation of the samples, 1 ml of blood serum was transferred into sterile plastic tubes. The tubes measured 10 ml in volume, 9.5 cm in length, and 1.5 cm in diameter. The tubes had two detectors (CR-39), each measuring 1 mm in thickness and 1 × 1 cm² in area (from Track Analysis Systems Ltd, UK). The first detector was positioned at the base of the sample to measure uranium concentrations, while the subsequent detector was situated at the top to assess Polonium on

Table 1. Information on cancer patients in the present study.

No.	Gender	Sample code	Type of cancer	Age	BMI
1	Male	*MC1	Lung	52	28
2		MC2		64	25.1
3		MC3		73	27
4		MC4		50	19.1
5		MC5		54	28.7
6		MC6		49	18.8
7		MC7	Prostate	69	34
8		MC8		73	23.8
9		MC9	Leukemia	65	25.3
10		MC10	Throat	74	21
11		MC11	Kidney	65	28.4
12		MC12	Testis	20	27.2
13		MC13	bone	30	29.3
14		MC14	Stomach	42	29.3
15		MC15	Breast	74	28
16	Female	**FC1	Breast	63	23.6
17		FC2		58	31.2
18		FC3		50	31.5
19		FC4		55	32.5
20		FC5		43	32
21		FC6		52	39
22		FC7		42	21.5
23		FC8		33	31
24		FC9	Leukemia	64	30.7
25		FC10		73	18
26		FC11	Skin	20	32
27		FC12		68	44
28		FC13	Larynx	58	26.6
29		FC14	Salivary gland	82	27.2
30		FC15	Lung	56	21

*MC = male cancer, **FC = female cancer

the wall (POW) of the irradiation container and Polonium on the surface (POS) of the irradiation container. The tubes were retained at the Nuclear and Environmental Laboratory at the Faculty of Science/ University of Kufa for a minimum of 90 days. After a three-month exposure period, detectors of CR-39 were taken from containers (plastic) and chemically etched under NaOH (6.25 N) in a bath of water (HH-420, Germany) at 98°C temperature for one hour. The latter detectors were next cleaned utilizing distilled water. Using a 400x optical microscope (Novel, China), the track count was determined by equipped with a digital eyepiece and a specified field of view [20].

2.4. Uranium and Polonium Concentration Assessment

The calibration curve was used in blood serum samples of the present study, which can determine the uranium concentrations (U_C) according to track density per unit time (ρ) in a unit (Track/cm^2.hour), as from the following equation [21]:

$$U_c\ (ppb) = \frac{(\rho + 12.5)}{18.6} \qquad (1)$$

The concentrations of ^{218}Po and ^{214}Po (POW and POS), deposited on the wall and face of the irradiation chamber, were identified using the below equations [22, 23]:

$$D_{P218} = D_{P214} = \frac{C}{4} r \left(\frac{r}{r+h}\right) cos\theta_C \qquad (2)$$

$$D_{P218} = D_{P214} = \frac{C}{4} r \left(\frac{r}{r+h}\right)\left(cos\theta_C \frac{r}{R_\alpha}\right) \qquad (3)$$

where, C refers to the radon concentration, h denotes the distance extended from the sample surface to the detector, r represents the exposure tube radius, that is 0.75 cm, R_α signifies the average range of alpha particle in the air for radon-222, measured at 4.15 cm, and θ_C indicates the mean critical angle for CR-39 detectors, recorded at 15° [23, 24].

3. STATISTICAL ANALYSIS

IBM SPSS Statistics program was employed for the conduction of statistical analysis of the data, particularly (version 27 for the Windows) operating system. The Mann-Whitney test compared mean uranium, POW, and POS concentrations (means ± S.D) in cancer Patients and healthy males and females. This non-parametric test compares two independent groups when the data are not normally distributed. It is used to determine whether the two groups have statistically significant differences.

4. RESULTS AND DISCUSSION

Table 2 demonstrates the results of uranium U_C, POW, and POS concentrations in blood serum samples from cancer patients, male and female, respectively. The values of U_C in male patients ranged from 0.082 ppb to 0.171 ppb while the values of U_C in female patients ranged from 0.084 ppb to 0.126 ppb, respectively. The values of POW in male patients ranged from 1.41 Bqm^{-3} to 9.06 Bqm^{-3} while the values of POW in female patients ranged from 1.60 Bqm^{-3} to 5.24 Bqm^{-3}, respectively. The values of POS in male patients ranged from 0.25 Bqm^{-3} to 1.64 Bqm^{-3}. While the values of POS in female patients ranged from 0.29 Bqm^{-3} to 0.95 Bqm^{-3}, respectively.

Table 2. Results of uranium concentrations in cancer patient groups in the present study.

No.	Gender	Sample code	U_C ppb	POW Bqm^{-3}	POS Bqm^{-3}
1		MC1	0.088	1.92	0.35
2		MC2	0.107	3.54	0.64
3		MC3	0.082	1.46	0.26
4		MC4	0.091	2.15	0.39
5		MC5	0.088	1.92	0.35
6		MC6	0.097	2.71	0.49
7		MC7	0.144	6.72	1.22
8	Male	MC8	0.123	4.98	0.90
9		MC9	0.171	9.06	1.64
10		MC10	0.127	5.28	0.95
11		MC11	0.082	1.41	0.25
12		MC12	0.106	3.51	0.63
13		MC13	0.117	4.39	0.79
14		MC14	0.120	4.66	0.84
15		MC15	0.119	4.57	0.83
16		FC1	0.126	5.24	0.95
17		FC2	0.084	1.60	0.29
18		FC3	0.087	1.82	0.33
19		FC4	0.089	1.99	0.36
20		FC5	0.117	4.42	0.80
21		FC6	0.117	4.43	0.80
22		FC7	0.099	2.91	0.53
23	Female	FC8	0.114	4.22	0.76
24		FC9	0.087	1.84	0.33
25		FC10	0.103	3.26	0.59
26		FC11	0.104	3.35	0.61
27		FC12	0.091	2.22	0.40
28		FC13	0.091	2.16	0.39
29		FC14	0.093	2.33	0.42
30		FC15	0.095	2.58	0.47

Table 3 shows the results of U_C, POW, and POS concentrations in blood serum samples from healthy males and females, respectively. The values of U_C in healthy males ranged from 0.073 ppb to 0.082 ppb while, the values of UC in healthy females ranged from 0.073 ppb to 0.074 ppb, respectively. The values of POW in healthy males ranged from 0.68 Bqm^{-3} to 1.44 Bqm^{-3} while the values of POW in healthy females ranged from 0.66 Bqm^{-3} to 0.74

Bqm^{-3}, respectively. The values of POS in healthy males ranged from 0.12 Bqm^{-3} to 0.26 Bqm^{-3} while the values of POS in healthy females ranged from 0.12 Bqm^{-3} to 0.13 Bqm^{-3}, respectively.

All criteria in blood serum samples are compared between patient and healthy groups using the Mann-Whitney Test. With a p-value less than 0.01. Table 4 and Table 5 clearly illustrate the extremely significant variations between the sick and healthy groups for U_C, POW, and POS. The results indicated that men exhibited the greatest amounts of uranium, ^{218}Po, and ^{214}Po, whilst females had the lowest values. The mean concentrations of uranium, ^{218}Po, and ^{214}Po in cancer patient samples from the Al-Najaf governorate were greater than those in healthy individuals, for both men and females, as seen in Table 4 and Table 5, respectively.

Table 3. Results of uranium concentrations in healthy groups in the present study.

No.	Gender	Sample code	U_C ppb	POW Bqm^{-3}	POS Bqm^{-3}
1		*MH1	0.080	1.26	0.23
2		MH2	0.082	1.44	0.26
3	Male	MH3	0.079	1.20	0.22
4		MH4	0.080	1.26	0.23
5		MH5	0.073	0.68	0.12
6		**FH1	0.074	0.73	0.13
7		FH2	0.073	0.69	0.12
8	Female	FH3	0.073	0.69	0.12
9		FH4	0.074	0.74	0.13
10		FH5	0.073	0.66	0.12

*MH = male healthy, **FH = female healthy

Table 4. Results of uranium, POW and POS concentrations in patient and healthy groups in males.

Radioactivity	Groups	N	Mean ± SD	P value
U_C ppb	patient	15	0.110±0.024	0.001
	healthy	5	0.078±0.003	HS
POW Bqm^{-3}	patient	15	3.885±2.132	0.001
	healthy	5	1.168±0.287	HS
POS Bqm^{-3}	patient	15	0.702±0.386	0.002
	healthy	5	0.212±0.053	HS

Table 5. Results of uranium, POW and POS concentrations in patient and healthy groups in females.

Radioactivity	Groups	N	Mean ± SD	P value
U_C ppb	patient	15	0.099±0.013	0.001
	healthy	5	0.073±0.001	HS
POW Bqm^{-3}	patient	15	2.958±1.146	0.001
	healthy	5	0.702±0.032	HS
POS Bqm^{-3}	patient	15	0.535±0.207	0.001
	healthy	5	0.124±0.005	HS

Figure 1 shows three box plots representing the concentrations of U_C ppb, ^{218}Po (POW), and ^{214}Po (POS) in a group of male patients. The median value of U_C is around 0.10, indicating that most values are concentrated near this point. An outlier above 0.18, located beyond the upper whisker, suggests a case with a high concentration. The IQR

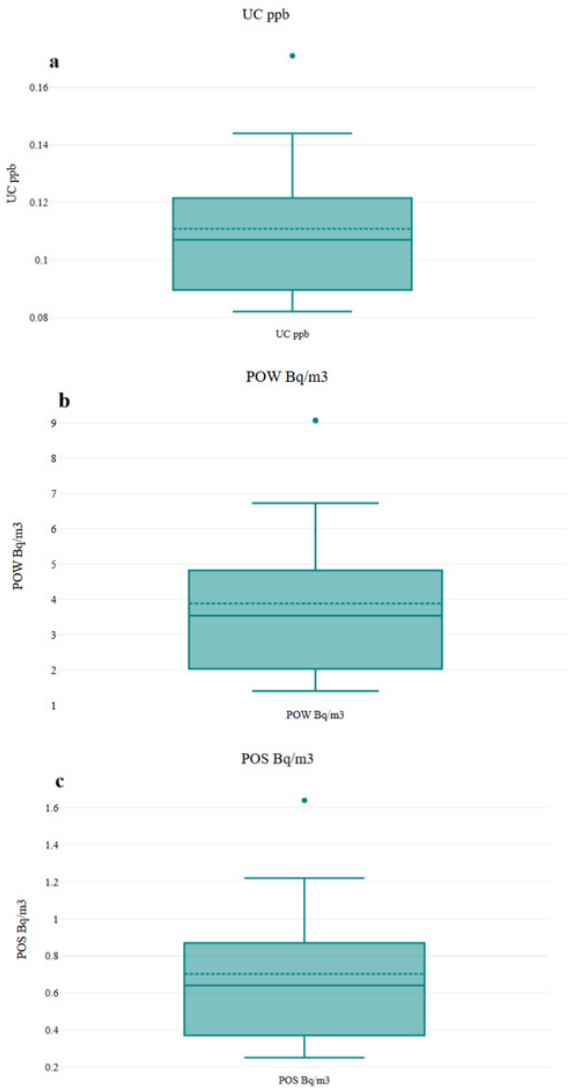

Fig. 1. Box plot of (a) uranium, (b) POW, and (c) POS concentrations in patient groups for male.

shows moderate dispersion, reflecting a relatively stable distribution of concentrations. The median (POW) here is slightly above 4, indicating higher concentrations compared to Uranium. Outliers above 9 indicate some cases with higher-than-usual concentrations. The box shows relatively wide dispersion, suggesting variability in ^{218}Po levels among patients. The median of POS is around 0.8, reflecting lower concentrations compared to ^{218}Po. There are also outliers in sample MC9. Moderate dispersion in the IQR reflects relatively uniform data.

Figure 2 shows three box plots representing the concentrations of U_C, POW, and POS in a group of female patients. The median concentration is approximately 0.10, indicating that most values are concentrated around this point. There are no significant outliers, and the upper whisker extends just above 0.12. The IQR shows moderate dispersion, reflecting a stable concentration distribution. The median of POW concentration is around 3, indicating higher levels compared to Uranium. No outliers are present, and the whiskers show moderate spread, with values reaching up to about 5. The relatively wide IQR suggests variability in ^{218}Po concentrations among female patients. The median of POS concentration is near 0.6, indicating lower levels compared to ^{218}Po but slightly higher than Uranium. No outliers are present, and the whiskers extend from approximately 0.2 to 1.0. Moderate dispersion within the IQR suggests a consistent distribution of ^{214}Po concentrations.

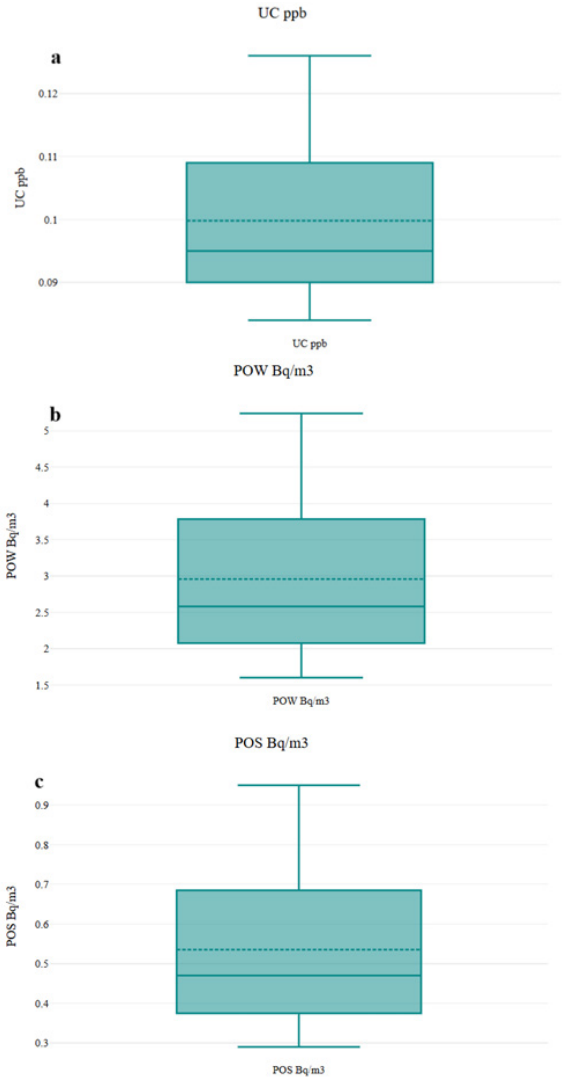

Fig. 2. Box plot of (a) uranium, (b) POW and (c) POS concentrations in patient groups for females.

Uranium is found in trace levels in soil, water, rocks, and living things. Everybody possesses trace amounts of natural uranium. Uranium's inherent radioactivity is low, resulting in little radiotoxicity. However, having considered it is a heavy metal, it has chemical toxicity (lead), which is more serious than its radiotoxicity. Lethal doses of uranium vary from several grams, while the standard body of male (adult) content is around tens of milligrams [8, 25]. Uranium and polonium levels in blood serum samples from male and female patients and healthy people were measured. Both men and women in the ill group had higher mean uranium and polonium levels than healthy people. The Mann-Whitney Test showed a significant difference in uranium levels between the ill and healthy groups ($P < 0.01$). The ill have higher uranium and polonium levels than non-patients. The afflicted group had 61% more uranium in their blood below and the internationally healthy group. The findings showed that both sick and healthy persons had blood serum uranium concentrations below the ICRP (International Commission on Radiological Protection) limit of 0.801 ppb [26, 27]. Additionally, none of the samples in this investigation had polonium values above the 550 Bqm^{-3} WHO (World Health Organization) recommended safe level [28]. The findings of this research demonstrate that the amounts of radon progeny (POW and POS) in blood serum samples varied across all men and females, regardless of health status. The prolonged indoor confinement of most women presumably resulted in increased radiation exposure; however, the variation may also stem from the nature of the samples and the nuclear composition inside them.

The study findings indicate that the blood may be devoid of environmental contaminants, and the levels of radon progeny (POW and POS) are much below international safety standards. The findings indicated that radon levels fluctuate based on the kind of cancer, individual patient, and geographical region, attributable to the body's allergic response to radiation [11]. All findings were markedly elevated for male patients compared to female individuals. Radiation induces an allergic reaction in women, perhaps explaining the lower radon levels seen in this demographic; women who spend prolonged durations at home are more susceptible to elevated radiation exposure. Individuals who spend greater durations inside have decreased ventilation rates compared to individuals who spend less time in their residences. Numerous research has been made using CR-39 NTD (Nuclear Track Detectors) to ascertain the quantity of uranium/radon progenies and alpha emitters in biological materials, facilitating a deeper comprehension of radon and its ephemeral offspring. Splatter investigations have been made using CR-39 NTDs, to assess the content of uranium (U_C), radon progenies (POW and POS), and alpha emitters in biological samples, facilitating a deeper comprehension of radon and its ephemeral offspring [29-32].

Table 6 displays Pearson correlation coefficients between Uranium, ^{218}Po (POW), and ^{214}Po (POS) concentrations for both male and female patient groups.

Uranium and ^{218}Po (POW):
For males, there is a very strong positive correlation ($r = 1.000$, $p < 0.01$), suggesting that as Uranium levels increase, ^{218}Po levels also increase consistently.

For females, the correlation is weak and not statistically significant ($r = -0.302$, $p > 0.05$).

Uranium and ^{214}Po (POS):
In males, there is a strong positive correlation ($r = 1.000$, $p < 0.01$). or females, the correlation is weak ($r = -0.301$) and not significant.

^{218}Po (POW) and ^{214}Po (POS):
In both males and females, there is a significant positive correlation (males: $r = 1.000$, females: $r = 1.000$, $p < 0.01$), indicating a consistent relationship between these two isotopes across genders.

Lastly, strong correlations between Uranium, ^{218}Po, and ^{214}Po are observed in male patients, indicating similar concentration patterns. In contrast, correlations are weaker and less significant among females, suggesting different distribution or metabolic patterns.

5. CONCLUSIONS

This research aimed to investigate uranium and polonium concentrations in serum samples from cancer patients and healthy individuals. The results revealed that the mean uranium and polonium levels in patient samples were higher than those in healthy samples. Additionally, male participants exhibited greater mean uranium and polonium concentrations compared to females. However, the concentrations of studied uranium in all examined samples were generally low, remaining below the global average levels reported by the International Commission on Radiological Protection (ICRP). Similarly, polonium concentrations in all samples were below the limits recommended by the World Health Organization (WHO). Therefore, the uranium and

Table 6. Pearson correlation between variables for female and male patients.

Pearson correlation		U_C		POW		POS	
		M	F	M	F	M	F
U_C	M	1	-0.3	1**	-0.2	1**	-0.3
	F	-0.3	1	-0.3	1**	-0.2	1**
POW	M	1**	-0.3	1	-0.2	1**	-0.2
	F	-0.2	1**	-0.2	1	-0.2	1**
POS	M	1**	-0.2	1**	-0.2	1	-0.2
	F	-0.3	1**	-0.2	1**	-0.2	1

** Correlation is significant at the 0.01 level (2-tailed).

polonium (POW and POS) concentrations in blood serum samples from patients and healthy males and females in Al-Najaf Governorate, Iraq, were determined to be within safe limits.

6. CONFLICT OF INTEREST

The authors declare no conflict of interest.

7. REFERENCES

1. A.A. Alkufi, A.A. Abojassim, and M.H. Oleiwi. Use of air things radon detector in liquid samples (serum and urine). *Applied Radiation and Isotopes* 207: 111265 (2024).
2. N.F. Kadhim, Y.A. Kadhim, R.S. Ahmed, A.A. Ridha, and M.Y. Mostafa. The impact on alpha emission rates of varying distances between a CR-39 detector and alpha-emitting bone samples. *Radiation Detection Technology and Methods* 5: 618-626 (2021).
3. H.K. Obaed and M.S. Aswood. Estimated of U, Rn and Po concentrations in smokers blood samples collected from Babylon, Iraq. *Materials Science and Engineering* 928: 072043 (2020).
4. C.J. Olowookere, K. Aladeniyi, G.A. Abu, and J. Erimona. Evaluation of Cancer Risks Associated with Radon Concentration Measured in the Science Faculty Building Complex Basement of a Tertiary Institution in South West, Nigeria. *Journal of Applied Sciences and Environmental Management* 26: 837-843 (2022).
5. Z.Q. Rahman and A.A. Al-Hamzawi. In-vitro radiological and toxicological detection in urine samples of cancer patients in Al-Diwaniyah governorate, Iraq. *International Journal of Radiation Research* 20: 103-108 (2022).
6. M.S. Aswood, A.A. Abojassim, and M.S.A. Al Musawi. Natural radioactivity measurements of frozen red meat samples consumed in Iraq. *Radiation Detection Technology and Methods* 3: 57 (2019).
7. A.A. Al-Hamzawi, M.S. Jaafar, and N.F. Tawfiq. The measurements of uranium concentration in human blood in selected regions in Iraq Using CR-39 track detector. *Advanced Materials Research* 925: 679-683 (2014).
8. A.A. Alkufi, M.H. Oleiwi, A.A. Abojassim, N.U.G. Mohammed, A.S. Jassim, and M. Guida. Determination Uranium and its Isotopes in Biological Samples of Smokers. *Baghdad Science Journal* 21(12): 4105-4117 (2024).
9. A. Boryło. Determination of uranium isotopes in environmental samples. *Journal of Radioanalytical and Nuclear Chemistry* 295: 621-631(2013).
10. D. Banks, O. Røyset, T. Strand, and H. Skarphagen. Radioelement (U, Th, Rn) concentrations in Norwegian bedrock groundwaters. *Environmental Geology* 25: 165-180 (1995).
11. S. Othman, N. Salih, and Z. Hussein. Determination of radon concentration level and its progenies in breast cancer using CR-39 NTD. *International Journal of Cancer Research & Therapy* 7: 216-226 (2022).
12. A.A. Alkufi, M.H. Oleiwi, and A.A. Abojassim. Radon concentrations in the serum of blood and urine of smokers using RAD-7 detector. *International Journal of Nuclear Energy Science and Technology* 17: 18-27 (2024).
13. R.W. Field. Radon: A leading environmental cause of lung cancer. *American Family Physician* 98: 280-282 (2018).
14. A.A. Alkufi, A.A. Abojassim, and M.H. Oleiwi. Radon Concentration in Biological Samples of Smokers and Non-smokers Using Lexan Detector. *Atom Indonesia* 50: 127-134. (2024).
15. J. Gaskin, D. Coyle, J. Whyte, and D. Krewksi. Global estimate of lung cancer mortality attributable to residential radon. *Environmental Health Perspectives* 126(5): 057009 (2018).
16. N.F. Salih, Z.M. Jafri, and M.S. Aswood. Measurement of radon concentration in blood and urine samples collected from female cancer patients using RAD7. *Journal of Radiation Research and Applied Sciences* 9: 332-336 (2016).
17. A.A. Alkufi, M.H. Oleiwi, and A.A. Abojassim. Heavy Metals in Blood Serum of Smokers and Non-smoking Controls. *Current Analytical Chemistry* 20: 175-182 (2024).
18. F.A. Taher and A.A. Abojassim. Uranium concentrations and its isotopes in baby food of Iraq. *Radiochimica Acta* 112: 391-399 (2024).
19. S. Othman, N. Salih, and Z. Hussein. Investigation of radon concentration level and its progeny in different kinds of cancer by using CR-39 NTD. *Radiation Effects and Defects in Solids* 178: 456-484 (2023).
20. A.A. Alkufi, M.H. Oleiwi, and A.A. Abojassim. Thoron Concentrations in Blood Serum, Urine, Hair, and Nails of Smokers and Non-smokers. *Library Progress International* 44: 706-716 (2024).
21. S.M. Qaddoori and S.S. Shafik. CR-39 As A Tool for Uranium Concentration Calculation in Bio Assay Sample: Bladder Cancer as Case Study. *Research Journal of Pharmaceutical Biological and Chemical Sciences* 9: 228-239 (2018).

22. A.A. Abojassim, T.A. Abdulwahid, R.H. Hashim, A.S. Abdulshaheed, and H.H. Rajab. ^{222}Rn, ^{218}Po, and ^{214}Po concentrations in blood samples of cancer patients at Najaf and Kufa cities of Al-Najaf Governorate. *AIP Conference Proceedings* 2386: 080025 (2022).
23. A.A. Alkufi, A.A. Abojassim, and M.H. Oleiwi. Concentrations of radon and other alpha emitters in biological samples of smokers and non-smokers. *Journal of Radioanalytical and Nuclear Chemistry* 333: 3857-3865 (2024).
24. A.P. Pereyra, H.M.E. Lopez, F.D. Palacios, B.L. Sajo, and P. Valdivia. Semi-empirical approach for calibration of CR-39 detectors in diffusion chambers for radon measurements. In: Proccedings of the ISSSD**.** *September 24th to 28th, 2016. Tuxtla Gutierrez, Chiapas, Mexico* pp. 228-253 (2016).
25. L.S. Keith, O.M. Faroon, and B.A. Fowler. Uranium (Chapter 45). In: Handbook on the Toxicology of Metals. G.F. Nordberg, B.A. Fowler, M. Nordberg, and L.T. Friberg (Eds.) *Elsevier* pp. 882-900 (2015).
26. J. Valentin. Basic anatomical and physiological data for use in radiological protection: reference values: ICRP Publication 89. *Annals of the ICRP* 32: 1-277 (2002).
27. Z. Abdelkafi and M.S. Aswood. Quantitative of uranium levels in blood samples of cancer patients collected from different regions in Iraq. *Radiation Physics and Chemistry* 223: 111975 (2024).
28. World Health Organization. WHO vaccine-preventable diseases: monitoring system, global summary (2009). https://iris.who.int/bitstream/handle/10665/70149/WHO_IVB_2009_eng.pdf
29. A. Hassan, A.A.H. Mohsen, H. Zahed, and A.A. Abojassim. Determination of alpha particles levels in blood samples of cancer patients at Karbala Governorate, Iraq. *Iranian Journal of Medical Physics* 16: 41-47 (2019).
30. T.F. Naji and S.O. Hassoon. Measuring of Radon Gas Concentrations in serum samples of Lung cancer patients in Babylon governorate, Iraq. *Journal of Physics: Conference Series* 1999: 012054 (2021).
31. T.A. Abdulwahid, I.K. Alsabari, A.A. Abojassim, H.A.A. Mraity, and A.B. Hassan. Assessment of concentrations of alpha emitters in cancer patients blood samples. *Sylwan* 164: 154-164 (2020).
32. T.I. Todorov, H. Xu, J.W. Ejnik, F.G. Mullick, K. Squibb, M.A. McDiarmid, and J.A. Centeno. Depleted uranium analysis in blood by inductively coupled plasma mass spectrometry. *Journal of Analytical Atomic Spectrometry* 24: 189-193 (2009).

Proceedings of the Pakistan Academy of Sciences: A Physical and Computational Sciences 61(4): 349-359 (2024)

ISSN (Print): 2518-4245; ISSN (Online): 2518-4253
http://doi.org/10.53560/PPASA(61-4)685

Pakistan Academy of Sciences

Research Article

Study of Newly Synthesized Pyridinium-based Cationic Surfactants for Drug Interaction and Antibacterial Activity

Ali Jaan[1,2], Saqib Ali[2], Mohsin Javed[1], Ali Haider[2], Khurram Shahzad Munawar[3,4]*, Saja Abdulrahman Althobaiti[5], and Mahboob ur Rehman[6]

[1]Department of Chemistry, School of Science, University of Management and Technology, C-II Johar Town, Lahore, Pakistan

[2]Department of Chemistry Quaid-i-Azam University, 45320, Islamabad, Pakistan

[3]Institute of Chemistry, University of Sargodha, Sargodha, 40100, Pakistan

[4]Department of Chemistry, University of Mianwali, Mianwali, 42200, Pakistan

[5]Department of Chemistry College of Sciences and Humanities, Prince Sattam Bin Abdulaziz University, Saudi Arabia

[6]Cardiology Department, Pakistan Institute of Medical Sciences (PIMS), Islamabad, Pakistan

Abstract: Two pyridinium-based new cationic surfactants have been synthesized by the reaction of 2-methylpyridine and 3-methylpyridine with an alkyl halide (1-bromoctadecane) using dry toluene as a solvent to get the compounds, N-(n-octadecyl)-2-methylpyridinium bromide (A1) and N-(n-octadecyl)-3-methylpyridinium bromide (A2), respectively. The synthesized samples were characterized by using various spectroscopic techniques. The synthesized compounds showed a critical micelle concentration in a very low-value range (0.111 mM to 0.125 mM), proving the synthesized compounds' best surface-acting ability. Both compounds exhibited limited antibacterial activity across various bacterial strains, with inhibition zones ranging from 3 to 7 mm. The change in Gibb's free energy (ΔG) was also calculated from their binding constant (K_b) for samples A1 **(**-10.0 kJ/mol) and A2 **(**-19.37 kJ/mol). The samples demonstrated spontaneous interactions with the drug molecules, which proved the efficient bioavailability of the drug due to the best incorporation of drug molecules with the aggregated monomers of surfactant molecules.

Keywords: Pyridinium, Cationic Surfactants, Drug Delivery, Antibacterial Activity, Spectroscopic Techniques.

1. INTRODUCTION

Recent advancements in the development and application of surfactants have been notable, driven by a focus on improving their performance [1-3]. These innovations in surfactant production are unlocking new opportunities for their use across various scientific disciplines, leading to more efficient and effective solutions in areas such as chemistry, materials science, and industrial applications [4-8]. Although the surfactants' study has become a considerable field of science, an uninterrupted regulation of environment-friendly consumer products is still needed, by developing new molecules, tailored for the required purposes and applications explicitly. Especially, the compounds of cationic surfactants are a class in which the nitrogen atom (of the pyridine ring in the case of pyridinium-based surfactant) possesses a positive charge, which is referred to as the tail of a compound, directly linked to the alkyl head group. This framework makes them cleavable (i.e., also named cleavable surfactants) because their properties are easily reformed from surface-acting agents to non-active agents by the decomposition process making them an efficient biodegradable

Received: October 2024; Revised: November 2024; Accepted: December 2024
* Corresponding Author: Khurram Shahzad Munawar <khurramchemist@gmail.com>

agent. Alongside, they exhibit germicidal properties as sanitizing agents, static-free agents, corrosion-inhibiting agents, and inter-fiber friction-reducing agents [9, 10]. Surfactants are so named due to their role as surface-active agents, a term that reflects their bioavailability and ability to interact with surfaces [11, 12].

The nature of surfactant molecules is inorganic as they show amphiphilic characteristics. Therefore, they contain a hydrophilic polar head group and a hydrophobic non-polar tail group showing water-soluble and water-insoluble properties, allowing the comparison of solubilities even with the seawater [13-15]. In this regard, when surfactant molecules migrate toward the surface of the water, the hydrophobic part goes on to the air or into the oil phase. If water is mixed with the oil, the polar part is simply retained in the water phase [16]. The aggregation as well as the positioning of the different groups of the surfactant molecules enables the surfactants to change the surface properties of water at different interfaces including water-oil/water-air interfaces [17, 18]. For instance, the decline in the aggregation property of surfactants, regarding their micellization, is due to the salt incorporation having bromide ion as an anionic radical [19-21]. The general and bio-related surfactants are divided into various fields of science regarding their applicability in daily life as well as in vast medical fields, including nucleic acid delivery, etc. [22-25]. In nitrogen-based cationic surfactants, a head group is considered a hydrophilic polar nature part, soluble in water. In contrast, the tail group, which is more often thought to be a long chain of alkyl nonpolar hydrophobic parts, is insoluble in water [26].

The proper and controlled release of drugs is mandatory for drug therapy to living organisms more likely to humans [27]. In most cases, non-uniform drug concentration release is observed and the solution of this proposed remedy is crucial. To avoid the inimical effect produced by the high-concentration delivery to the non-targeted spot and low concentration to the targeted spot, the controlled delivery of the drug is demanded [28, 29]. More often the hydrophobic nature of drugs used for the drug delivery phenomenon is intended to decrease the degradation of the drug and the detrimental effects with the efficient bio-availability on the required site of the body because of the drug's less solubilization property [30, 31]. Another major problem regarding to use of cationic or anionic drugs is the transformation of the structure of the cell membrane, which leads to the disturbance in the proper functioning of cells because the drugs cannot easily cross the cell membrane of living organisms. The complete therapy needs an excess amount of drug, which results in toxicity as well as the aggregation of drugs on non-target sites [32].
The present study is accompanied by the use of broadly used surfactants prepared by the derivatives of pyridine. The newly prepared compounds, followed by the use of the aggregation properties of monomers, are used for the efficient delivery of a required drug to the target site of the living body. The aggregation of the molecules leads to the micellization phenomenon, which provides the basic environmental needs for drug encapsulation as well as its safe delivery [33].

2. MATERIALS AND METHODS

2.1. Chemicals

All chemicals, such as alkyl halide, 2-methyl pyridine, 3-methylpyridine, and solvents, such as toluene, chloroform, methanol, ethanol, n-hexane, diethyl ether, ethyl acetate, and DMSO, used in the current work, were of analytical grade and purchased from Sigma-Aldrich and Alfa-Aesar.

2.2. Instrumentation

A Sanyo electro-thermal melting point apparatus was used for the melting point determination of the synthesized compounds with the help of an open capillary tube. A 3000MX model of Bio-Rad Excalibur was used for recording the FT-IR absorption spectra using KBr pallets in the range of 4000-400 cm^{-1} [34]. A 300 MHz-FT-NMR of Bruker AC was used to take ^{1}H-NMR & ^{13}C-NMR spectra in deuterated solvent ($CDCl_3$). The chemical shift of various bonds was denoted with δ and given in parts per million (ppm). The structures of newly synthesized cationic surfactants were confirmed by FT-IR, ^{1}H-NMR, and ^{13}C-NMR spectroscopies. The peaks for C-N in the samples A1 and A2 were observed at 1170 cm^{-1} and 1209 cm^{-1}, respectively, in FT-IR spectra. Similarly, the signals for C-N moiety in ^{1}H NMR can be seen at 58.56 ppm and 61.98 ppm for samples A1 and A2, respectively. The determination of critical micelle concentration

(CMC) followed by the drug interaction study was carried out using a spectrophotometer (Shimadzu) equipped with a UV lamp (SN:500412). The electrical conductivities also followed by the critical micelle concentration (CMC) of synthesized compounds were performed by the conductometer of Inolab 720 precision conductivity meter at room temperature.

2.3. Synthesis of Cationic Surfactants (A1 and A2)

The surfactants were prepared by reacting 5.20 mL of 1-bromoctadecane (0.020 moles) with 1.97 mL (0.020 moles) of 2-methylpyridine (for A1) and 3-methylpyridine (for A2), in 40 mL of dry toluene, separately. The reaction media were kept on a hot plate under the refluxing environment with continuous stirring for 12 hours until the brownish precipitates of A1 and white precipitates of A2 appeared from their respective media. After cooling, these precipitates were stirred with 50 mL of diethyl ether for 2-3 hours to remove the unreacted precursors. The precipitates were collected using filtration and finally dried in air. The general procedure for the synthesis of both samples and the carbon numbering pattern for NMR studies is shown in Scheme 1.

A1: Yield: 90 %; Molecular formula = $C_{24}H_{44}NBr$; Molecular mass = 426.4 g/mol; Physical state = Solid; Color = Brown: Melting Point = 123 °C: Solubility = Ethanol, Methanol, Acetone, DMSO, Chloroform; CMC at 298.16 K = 0.1255 (mmol/dm^3): FT-IR (400-4000 cm^{-1}), C-N = 1170, C=N = 1632, C=C = 1574, -CH_2 (Aliphatic) = 1466, CH (Aromatic) = 3039, CH_3 = 1142. ^{1}H-NMR (300 MHz, $CDCl_3$, δ-ppm): 9.61 (1H, H^5, d, ^3J = 5.7 Hz), 8.42 (1H, H^4, t, ^3J = 7.8 Hz), 7.997 (1H, H^3, t, ^3J = 3.6 Hz), 4.88 (2H, H^7, t, ^3J = 7.8 Hz), 2.98 (3H, H^6, s), 0.844-2.980 (37H, H^{8-24}, m). ^{13}C-NMR (75.5 MHz, $CDCl_3$, δ-ppm): 154.19 (C^1), 146.66 (C^2), 145.14 (C^3), 130.26 (C^4), 126.43 (C^5), 26.31 (C^6), 58.56 (C^7), 14.1-34.0 (C^8-C^{24}).

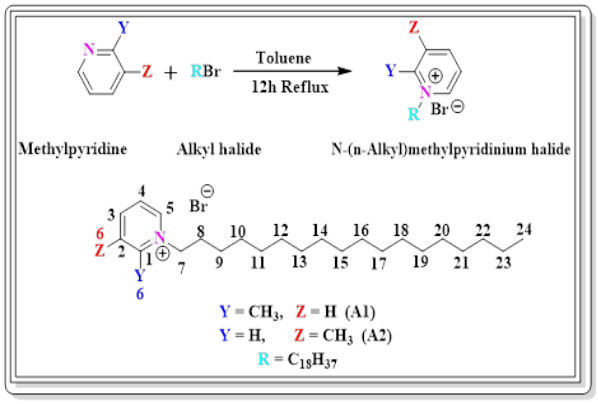

Scheme 1: Conversion of methylpyridine to N-(n-Alkyl) methylpyridinium halide (A1 and A2) and numbering pattern for NMR results.

A2: Yield: 95 %; Molecular formula = $C_{24}H_{44}NBr$; Molecular mass = 426.4 g/mol; Physical state = Solid; Color = White; Melting Point = 118 °C; Solubility = Ethanol, Methanol, Acetone, DMSO, Chloroform; CMC at 298.16 K = 0.1174 (mmol/dm^3); FT-IR (400-4000 cm^{-1}), C-N = 1209, C=N = 1633, C=C = 1590, -CH_2 (Aliphatic) = 1470, CH (Aromatic) = 3033, CH_3 = 1146; ^{1}H-NMR (300 MHz, $CDCl_3$, δ-ppm): 9.324 (1H, H^1, s), 9.216 (1H, H^5, d, ^3J = 5.7 Hz), 8.272 (1H, H^3, d, ^3J = 8.1 Hz), 8.027 (1H, H^4, t, ^3J = 7.5 Hz), 2.62 (3H, H^6, s), 4.92 (2H, H^7 t, ^3J = 7.2 Hz), 0.894-4.948 (37H, H^{8-24}, m). ^{13}C-NMR (75.5 MHz, $CDCl_3$, δ-ppm): 145.61 (C^1), 144.51 (C^2), 142.27 (C^3), 139.64 (C^4), 127.80 (C^5), 26.11 (C^6), 61.98 (C^7), 18.78-34.11 (C^8-C^{24}).

2.4. Determination of Critical Micelle Concentration (CMC)

The evaluation of critical micelle concentration was performed by conductometry and UV-Visible spectrophotometry.

2.4.1. Conductometry

Several different dilutions were prepared and tested by the conductometer, (equipped with a conductivity cell) calibrated by KCl, to check the conductivity of the surfactant-containing solution. Upon dilution with ethanol, the conductivity decreases and a clear change in the values of conduction was observed. The temperature was kept at 25.0 ± 0.1 °C due to the activity.

2.4.2. UV-Visible spectrophotometry

A series of different dilutions were prepared from a 25 mL stock solution of 0.3 M. Then, 1.3 mL was taken from the stock solution and diluted with the help of ethanol up to 2.6 mL to make the solution 0.15 M. To analyze the absorption data of the synthesized surfactants at different concentrations, 13 readings were taken for each 0.1 mL dilution using a micropipette. The dilutions were

prepared similarly to those used in conductivity measurements.

A double-beam spectrophotometer 1800 Shimadzu, having a scanning speed range from 200 to 800 nm was used for the measurement of absorption spectra using quartz cells with a path length of 1 cm. At the start, both cells were filled with 3/4th of solvent (Ethanol) for the baseline auto-zero correction. Then the sample cell was filled with the surfactant-containing a solution of a known concentration of 0.3 M, which was later on diluted to 0.15 M, to record the spectra.

2.5. Drug-Surfactant Interaction

The interaction of synthesized surfactants with the drug was carried out by taking the solution of the drug with a constant concentration in ethanol and interacting it with the variable concentrations (as discussed in the previous section) of surfactants, i.e., from pre-micellar to the post-micellar region. Initially, both cells were filled with solvent, for the auto-zero baseline correction. Consequently, a surfactant solution of different concentrations that are formed for the pre- to post-micellar region was mixed with the drug solution with its constant concentration. All the spectra of surfactant, with the drug, before and after CMC, were recorded.

2.6. Antibacterial Studies

The antibacterial activity was performed against *Staphylococcus aureus*, *Staphylococcus pseudo*, and *Klebsiella pneumoniae* bacterial strains. The bacterial cultured plates were prepared by dissolving Broth and Agar in deionized water in a flask and then autoclaved for 20 minutes. After cooling down the solution, a bacterial strain was introduced to the flask to prepare the inoculum. All three inoculums of bacteria were prepared following the same procedure and kept the inoculums for 24 hours in a shaker at a constant temperature. The already sterilized petri dishes were filled with the prepared solution of Agar and Broth. Then three bacterial strains were introduced separately into the prepared petri dishes. Then the positive and negative controls were added along with the sample and Gentamicin (standard drug) into the different zones of petri dishes and were placed into the incubator carefully for 24 hours. The bacterial strains showed the scavenging areas, which were noted down.

3. RESULTS AND DISCUSSION

3.1. Structural Elucidation

3.1.1. Fourier transform infrared (FT-IR) spectroscopy

The details of the spectral peaks are explained in the experimental section and FT-IR spectra of both samples A1 and A2 are shown in Supplementary Figures S1 and S2 (all Supplementary Figures can be accessed at: https://ppaspk.org/index.php/PPAS-A/article/view/1529/862). Generally, FT-IR spectroscopy exploits the fact of structural elucidation using functional group and type of bond determination. The assigned peaks to different types of bonds and various functional groups present in newly synthesized surfactants are accomplished through a literature review [35, 36]. The attachment of the pyridine ring to the long alkyl chain can be seen using the C-N bond, which is in the range of 1050-1200 cm^{-1}. A range of 717-728 cm^{-1} is purely associated with the hydrocarbon chain length. The peaks for the C=N of sample A1 can be seen at 1632 cm^{-1} and for the sample A2, it is visible at 1633 cm^{-1}. Moreover, the C-N peaks for samples A1 and A2 can be observed at 1170 cm^{-1} and 1209 cm^{-1}, respectively. The stretching peaks for the alkyl chain of aliphatic –CH_2, for samples A1 and A2, can be spotted at 1466 cm^{-1} and 1470 cm^{-1}, respectively. However, the aromatic –C-H, stretching peak usually appears slightly above 3000 cm^{-1}. So, for sample A1, it can be seen at 3039 cm^{-1}, and for sample A2, it is at 3033 cm^{-1}. The appearance of these peaks confirms the successful synthesis of above discussed new compounds and is in good agreement with the relevant literature [37-39].

3.2. Nuclear Magnetic Resonance (NMR) Spectroscopy

The details of the spectral peaks are discussed in the experimental section and the spectra of both samples are shown in Figures S3-S6. In the case of ^{1}H-NMR, a signal for -H_2C-$N_{(pyridine)}$ at 4.880 ppm for A1, and a signal for 4.924 ppm for A2 confirm the synthesis of samples. Furthermore, in the case of ^{13}C-NMR, the confirmatory signal due to -H_2C-$N_{(pyridine)}$ moiety was observed at 58.56 ppm and 61.98 ppm for samples A1 and A2, respectively. In the ^{13}C-NMR, the peaks for aromatic carbons (C1-C5) of sample A1 are visible at 154.19, 146.66,

145.14, 130.26, and 126.43 ppm, respectively. Meanwhile, the peaks for the aliphatic carbon chain can be seen in the 14.12-31.91 ppm range. For sample A2, the signal for aromatic carbons (C1-C5) can be seen at 145.61, 144.51, 142.27, 139.64, and 127.80 ppm, respectively. The peaks for the aliphatic carbon chain can be seen in the range of 18.78-34.11 ppm. The peak for the methyl carbon attached to the aromatic ring appears at 26.31 and 26.11 ppm for samples A1 and A2, respectively. Both samples acquired chemical shift values that nearly match the stated chemical shifts in the literature [3, 40, 41].

3.3. Determination of CMC by Conductometry

For conductometric measurements of synthesized compounds, the standard solutions were prepared in ethanol at 298 K. A graph was plotted against the concentration taken on abscissa and conductivity on the y-axis. A point where the accumulation of surfactant monomers started was of actual interest while discussing the graph, which is generally known to be as critical micelle concentration CMC. For exact CMC determination, the plotted graph was included with the differential conductance corresponding to the concentration of surfactant, which showed a sigmoid-shaped curve (Figure 1).

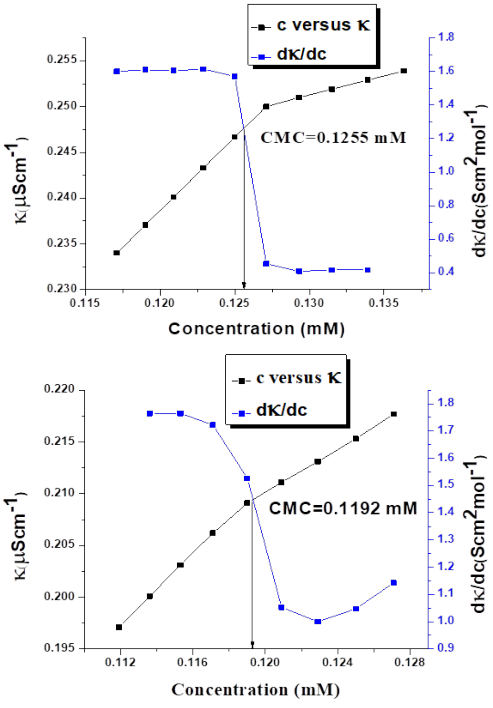

Fig. 1. The plots between conductivity (k) and differential conductivity (dk/dc) versus total concentration for the determination of CMC values for samples A1 (above) and A2 (below).

The graph shows that the conductance of the solution increases due to the excessive availability of free ions in the pre-micellar region of the surfactant solution. This is because, in the pre-micellar region, the molecules of the surfactant are in the form of monomers, which shows the presence of free cations and anions responsible for the increase in conductance value [42].

It was also observed that after reaching the post-micellar region of the surfactant, the conductance of the surfactant solution was lowered. The reason is that after the post miceller region, the free ions get captured by the micelle of the surfactant by incorporating inside the micelle and only the anion of the surfactant (Br^-) moves from one micelle to another. Therefore, the low conductance value is caused by the limited availability of free ions, which is represented on the graph as a sharp decline since they are all involved in the production of micelles [43, 44]. The CMC values of surfactants, A1 and A2, are 0.1255 and 0.1192 mM, respectively.

3.4. Determination of CMC by UV-Visible Absorption Spectroscopy

The absorption patterns of all the newly synthesized surfactant samples A1 and A2 are different, giving the critical micelle concentration (CMC) at different points. Unlike the CMC determination by using a conductometer, the CMC point identification was carried out by plotting a graph between concentration versus absorption and taking their differential values to avoid instrumental error. Whereas, λ_{max} determination of both samples A1 and A2 was carried out by the wavelength and absorption plot. The absorbance plots of samples A1 and A2 are shown in Figure 2. The CMC values of samples A1 and A2 are 0.1245 mM and 0.111 mM, respectively, which indicates that the CMC values calculated by both techniques are in the lower range which is beneficial for minimal toxicity by reducing the surfactant concentration.

3.5. Drug Interaction

The interaction of synthesized surfactants was also carried out with a standard drug ketoprofen (KP) (Figure S7). It has efficient anti-inflammatory activity and is also abbreviated as NSAID (non-steroidal anti-inflammatory drug) [45].

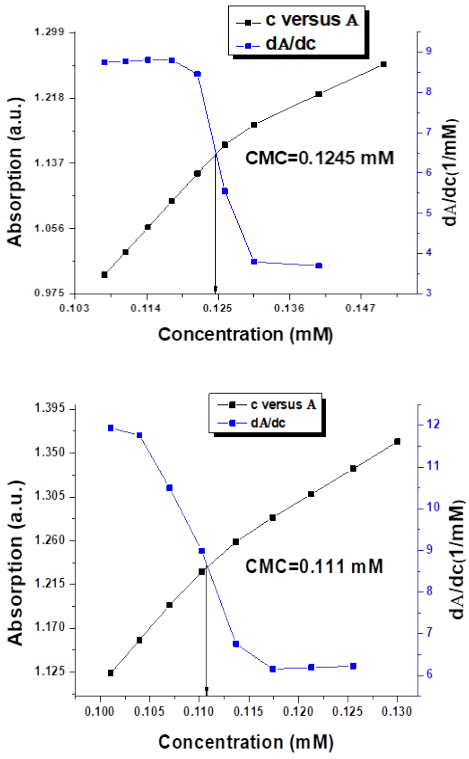

Fig. 2. The plots of Absorbance versus Concentration and the rate of change of absorbance with respect to concentration, showing the calculations of CMC values for samples A1 (above) and A2 (below).

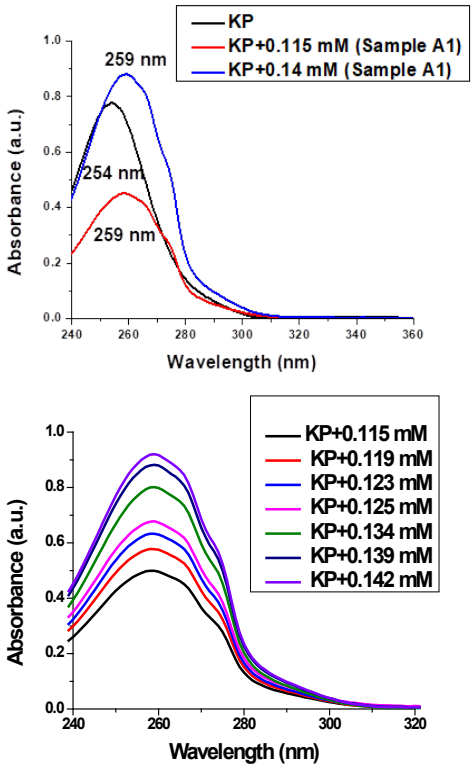

Fig. 3. Absorption spectra of KP; In the absence & presence of pre-micellar and post-micellar concentration of sample A1 (above) and with changing concentration of sample A1 (below).

3.5.1. Interaction of sample A1 with ketoprofen

The interaction pattern of newly synthesized surfactant sample A1 with the drug ketoprofen can be observed from the graphs as shown in Figure 3. As far as the absorption pattern of ketoprofen is concerned, it was noticed that the maximum absorption was at 254 nm. It was detected that when the drug was mixed with surfactant at pre-micellar concentration, a red shift of 5 nm was observed. In a post micellar region, an increase in drug absorption was observed, which depicts the enhancement of bio-availability and solubility of the drug. The premicellar and post-micellar concentrations of the sample with the drug are 0.115 mM and 0.14 mM, respectively [46, 47]. It was observed from the graphs that by increasing the concentration of surfactant, the absorption increases, which depicts the better solubilization of KP drug at 259 nm.

3.5.2. Interaction of sample A2 with ketoprofen

The interaction of ketoprofen with sample A2 shows almost the close pattern of absorption as that of sample A1 (Figure 4). The premicellar and post-micellar concentrations of the sample with the drug are 0.117 mM and 0.142 mM, respectively.

3.5.3. Calculations of Gibb's free energy and binding constant (K_b)

The interaction of samples A1, A2, and ketoprofen shows a straight-line pattern. For the sake of Gibb's free energy (ΔG) and binding constant (K_b) determination, a graph is plotted against 1/(Cs+Ca) versus 1/ΔA (Figure 5). The observed Gibb's free energy value was negative, which shows the reaction spontaneity between the ketoprofen and surfactant sample [48, 49].

As:

$$\Delta A = A^{o} - A$$

ΔA is the differential of absorbance.

A is the absorption of the drug at the same wavelength in the presence of surfactant.

A^{o} is the absorption of a drug in the absence of surfactant at its λ_{max}.

Ca is the concentration of the drug.

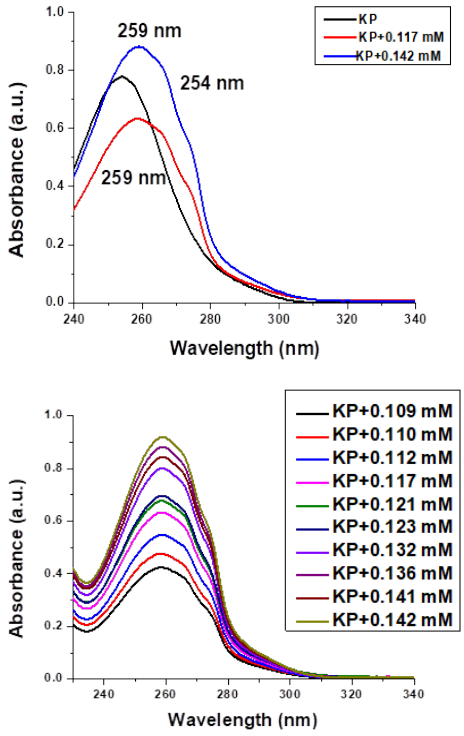

Fig. 4. Absorption spectra of KP, in the absence and presence of pre-micellar and post-micellar concentration of sample A2 (above) and with changing the concentration of sample A2 (below).

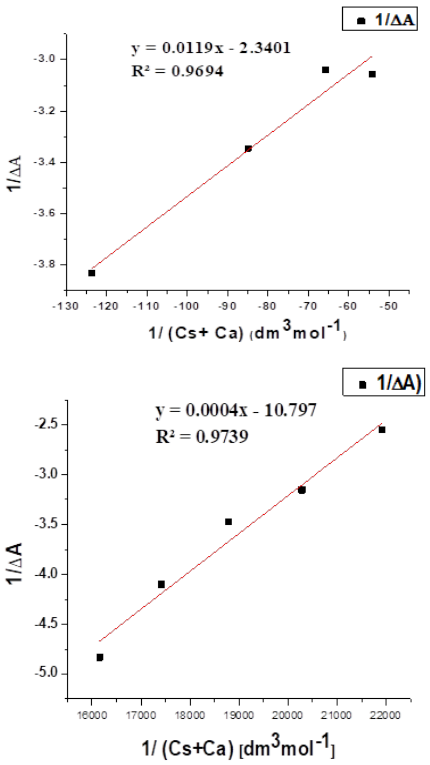

Fig. 5. Determination of binding constant (K_b) for samples A1 (above) and A2 (below).

Cs is the total surfactant concentration.
For sample A1,

We know the Lineweaver-Burk plot:
$1/\Delta A = m \cdot 1/(Cs + Ca) + b$
$y = mx + c$
slope (m) = 0.0119 [From Figure 5 (above)].
As, m = 1/K,
$K = 1/m = 1/0.0119 = 84.03\ M^{-1}$
(Also a binding constant $K_b = 84.03\ M^{-1}$)
We know that
$\Delta G = -RT \ln K$
R = 8.314 J/mol·K ; T = 298 K ; K = 84.03 M^{-1})

By putting the values in the Gibb's free energy equation, we get
$\Delta G = -(8.314\ J/mol \cdot K) \cdot (298\ K) \cdot \ln(84.03)$
$\Delta G = -(8.314 \times 298) \cdot \ln(84.03)$
$\Delta G = -(2477.572) \cdot \ln(84.03)$
$\Delta G = -(2477.572) \cdot 4.430$
$\Delta G = -10995.6\ J/mol \approx -10.0\ kJ/mol$

The change in Gibb's free energy (ΔG) is -10.0 kJ/mol at room temperature (298 K).

For sample A2,

We know the Lineweaver-Burk plot:
$1/\Delta A = m \cdot 1/(Cs + Ca) + b$
$y = mx + c$
slope m = 0.0004 [From Figure 5. (below)]
As, m = 1/K,
$K = 1/m = 1/0.0004 = 2500\ M^{-1}$
(Also a binding constant $K_b = 2500\ M^{-1}$)
We know that
$\Delta G = -RT \ln K$
R = 8.314 J/mol·K ; T = 298 K ; K = 2500 M^{-1})
By putting the values in the Gibb's free energy equation, we get
$\Delta G = -19.37$ kJ/mol

The spontaneity of the binding process is referred to as the negative ΔG value. The greater the negative value, the higher will be the spontaneity and the stronger will be the binding. With the help of concentrations of surfactants and KP, followed by the absorbance of both samples of KP in the presence and absence of drug, the graph is plotted against the reciprocal of change in absorbance and the reciprocal of drug concentration and surfactant concentration.

Table 1. Inhibition zones of samples A1, A2, Gentamycin (standard drug), and ethanol (negative control) against different bacterial strains.

Bacterial strains	A1 (0.1%)	A2 (0.1%)	Gentamycin (Positive control) (0.1%)	Ethanol (Negative control)
	Zones of inhibition (mm)			
Staphylococcus pseudo (Gram-positive)	7	5	6	6
Staphylococcus aureus (Gram-positive)	7	4	12	15
Klebsiella pneumoniae (Gram-negative)	5	3	5	10

The -ΔG for sample A1 and ketoprofen is 10.0 kJ/mol and for sample A2 and ketoprofen is 19.37 kJ/mol. The graph of sample A2 is plotted as same as sample A1 by the same calculations of absorbances and concentrations of surfactant and ketoprofen KP. Both the samples showed excellent activity with the drug and the best spontaneity of reaction. Ketoprofen showed efficient and almost the same patterned interaction regardless of Gibb's free value of both reactions.

3.6. Anti-bacterial Activities of Samples A1 and A2

The interaction of newly synthesized surfactant samples A1 and A2 was performed against *Staphylococcus pseudo, Klebsiella pneumoniae,* and *Staphylococcus aureus* bacterial strains and it was observed that the synthesized surfactants demonstrated limited inhibitory effects as reflected by the small zones of inhibitions observed (Figures S8-10, Table 1). The minimized result regarding the inhibition zones of the antibacterial activity may follow several reasons including the environmental factor involving the temperature and pH, and the invasion through the non-perforated bacterial outer membrane. For instance, Gram-negative bacteria exhibit likewise similar characteristics as discussed. Another reason, for the low antibacterial activity, may be the binding of the compound to the certain infected target, which may be owing to the hindrance in its structure, sterically. Some Gram-negative bacteria undergo the mutation which can be effectively responsible for the diversion of the antibiotic or a compound to another site, instead of the actual target, leading the compound least active toward the anti-bacterial activities [41, 50-52].

4. CONCLUSIONS

The unequivocal authentication for the newly synthesized pyridinium-based cationic surfactants, named N-(n-octadecyl)-2-methylpyridinium bromide (sample A1) and N-(n-octadecyl)-3-methylpyridinium bromide (sample A2), was investigated by FT-IR and NMR spectroscopic analysis. The aggregational behavior of the samples' monomers was manifested by the appreciable range of critical micelle concentration (CMC) values with the aid of conductometry and UV-visible spectroscopy. The efficient absorbance of the drug molecules to the samples' monomers was corroborated and authenticated by observing the absorbance patterns from pre-micellar to the post-micellar regions of the UV-visible spectrum during the sample-drug interaction. After micellization, the increased concentration of surfactant leads to more absorbance of the drug within the micelles of surfactant. The successful surpassing absorbance pattern of the drug-sample solution is remarking the pronounced bioavailability of the samples', leading it to the biomedical domain by augmenting its applicability. The cationic samples' binding capability and affinity with the anionic Ketoprofen drug encompass the substantial objective of the research work. The negative values of Ghibb's free energy for both compounds, calculated from the plots, depict the favorable spontaneity of the compounds. Moreover, both compounds are active toward the Gram-positive and negative bacterial strains, especially for the pronounced activity against *Staphylococcus aureus*. It is concluded that apart from the antibacterial activity, the synthesized samples with lower CMC values, are dynamically active towards the profound medical versatility as drug carriers.

5. CONFLICT OF INTEREST

The authors declare no conflict of interest.

6. ACKNOWLEDGEMENT

A.J. is thankful to Quaid-i-Azam University Islamabad for providing the facilities for this work. S.A. and A.H. thank the Pakistan Academy of Sciences and Quaid-i-Azam University, Islamabad for financial support.

7. REFERENCES

1. R. Aggarwal and S. Singh. Synthesis, self-aggregation, thermal stability, and cytotoxicity trends of alkyloxypropoxycyclohexane based pyridinium ionic liquids. *Journal of Molecular Liquids* 399: 124382 (2024).
2. P. Shenoy, N. Kedimar, and S.A. Rao. A comprehensive review on anticorrosive behaviour of surfactants across diverse metals using multiple techniques: Current insights and future horizons. *Chemical Engineering Journal Advances* 20: 100645 (2024).
3. B. Borikhonov, E. Berdimurodov, T. Kholikov, W.W. Nik, K.P. Katin, M. Demir, F. Sapaev, S. Turaev, N. Jurakulova, and I. Eliboev. Development of new sustainable pyridinium ionic liquids from reactivity studies to mechanism-based activity predictions. *Journal of Molecular Modeling* 30(11): 359 (2024).
4. S. Noori, A.Z. Naqvi, and W.H. Ansari. Experimental and Theoretical Approach to Cationic Drug-Anionic Gemini Surfactant Systems in Aqueous Medium. *Colloids and Surfaces B: Biointerfaces* 115: 71-78 (2014).
5. P. Werawatganone, and W. Muangsiri. Interactions between charged dye indicators and micelles to determine the critical micelle concentration. *Asian Journal of Pharmaceutical Sciences* 4: 221-227 (2009).
6. M.J. Rosen and J.T. Kunjappu (Eds.). 4th Edition. Surfactants and Interfacial Phenomena. *John Wiley and Sons, New York* (2012).
7. P.A. Bhat, A.A. Dar, and G.M. Rather. Solubilization capabilities of some cationic, anionic, and nonionic surfactants toward the poorly water-soluble antibiotic drug erythromycin. *Journal of Chemical & Engineering Data* 53(6): 1271-1277 (2008).
8. T. Feng, H. Yang, J. Zhang, and C. Zong. Applicability of cationic surfactants, anionic surfactants, and nonionic surfactants as foaming agents for foamed concrete: surface activity, foamability, and interaction with cement. *Journal of Sustainable Cement-Based Materials* 13(9): 1330-1347 (2024).
9. P. Madaan and V.K. Tyagi. Quaternary pyridinium salts: a review. *Journal of Oleo Science* 57(4): 197-215 (2008).
10. R. Talat, M.A. Asghar, I. Tariq, Z. Akhter, F. Liaqat, L. Nadeem, H. Ali, and S. Ali. Evaluating the Corrosion Inhibition Efficiency of Pyridinium-Based Cationic Surfactants for EN_3B Mild Steel in Acidic-Chloride Media. *Coatings* 12(11): 1701 (2022).
11. A.O. Ezzat, A.M. Atta, and H.A. Al-Lohedan. Demulsification of stable seawater/Arabian heavy crude oil emulsions using star-like tricationic pyridinium ionic liquids. *Fuel* 304: 121436 (2021).
12. A.G. Hassabo, F. Saad, B.M. Hegazy, A. Sediek, and H. Ghazal. The use of cationic surfactants in the textiles industry. *Journal of Textiles, Coloration and Polymer Science* 20(2): 227-242 (2023).
13. D. Fu, X. Gao, B. Huang, J. Wang, Y. Sun, W. Zhang, K. Kan, X. Zhang, Y. Xie, and X. Sui. Micellization, surface activities and thermodynamics study of pyridinium-based ionic liquid surfactants in aqueous solution. *Royal Society of Chemistry Advances* 9(49): 28799-807 (2019).
14. F. Qin, Y. Zhang, K. Naseem, Z. Chen, G. Suo, W. Hayat, and S.H.S. Gardezi. Assessment of the importance and catalytic role of chromium oxide and chromium carbide for hydrogen generation via hydrolysis of magnesium. *Nanoscale* 16(41): 19518-19528 (2024).
15. F. Qin, K. Naseem, Z. Chen, G. Suo, and A. Tahir. Carbon nano-tube coated with iron carbide catalysis for hydrolysis of magnesium to generate hydrogen. *International Journal of Hydrogen Energy* 83: 1359-1369 (2024).
16. A.Z. Hezave, S. Dorostkar, S. Ayatollahi, M .Nabipour, and B. Hemmateenejad. Effect of different families (imidazolium and pyridinium) of ionic liquids-based surfactants on interfacial tension of water/crude oil system. *Fluid Phase Equilibria* 360:139-45 (2013).
17. L.L. Schramm, E.N. Stasiuk, and D.G. Marangoni. 2 Surfactants and their applications. *Annual Reports Section "C" (Physical Chemistry)* 99: 3-48 (2003).
18. R. Goel, S. Bhardwaj, and S. Bana. Pharmaceutical excipients. *Dosage Forms, Formulation Developments and Regulations* 1: 311-348 (2024).
19. Z. Sun, Y. Ji, H. Wang, J. Zhang, C. Yuan, M. Kang and H. Yin. Impact of hydroxyethyl headgroup on long-

chain quaternary ammonium cationic surfactants: Solubility, surface activities, self-assembly behaviors, and rheological properties. *Colloids and Surfaces A: Physicochemical and Engineering Aspects* 700: 134831 (2024).

20. F.I. El-Dossoki, M.A. Migahed, M.M. Gouda, and S.A.E.H.A. El-Maksoud. Aggregation behavior of newly synthesized Gemini cationic surfactants in absence and in presence of different inorganic salts in 15% DMSO–water solvent. *Scientific Reports* 14(1): 20351 (2024).
21. T. Majeed, T.I. Sølling, and M.S. Kamal. Foamstability: The interplay between salt-, surfactant-and critical micelle concentration. *Journal of Petroleum Science and Engineering* 187: 106871 (2020).
22. C.B. Farias, F.C. Almeida, I.A. Silva, T.C. Souza, H.M. Meira, F.R. de Cássia, J.M. Luna, V.A. Santos, A. Converti, I.M. Banat, and L.A. Sarubbo. Production of green surfactants: Market prospects. *Electronic Journal of Biotechnology* 51: 28-39 (2021).
23. I.F.D.L. Fuente, S.S. Sawant, K.W. Kho, N.K. Sarangi, R.C. Canete, S. Pal, and J.L. Rouge. Determining the Role of Surfactant on the Cytosolic Delivery of DNA Cross-Linked Micelles. *ACS Applied Materials & Interfaces* 16(33): 43400-43415 (2024).
24. R.A. Gonçalves, K. Holmberg, and B . Lindman. Cationic surfactants: A review. *Journal of Molecular Liquids* 375: 121335 (2023).
25. S.P. Moulik, A.K. Rakshit, and B. Naskar. Physical chemical properties of surfactants in solution and their applications: A comprehensive account. *Journal of Surfactants and Detergents 27*(6): 895-925 (2024).
26. G. Hertel and H. Hoffmann. Lyotropic nematic phases of double chain surfactants. *Trends in Colloid and Interface Science II* 76: 123-131 (1988).
27. Z. Zhang, H. Liu, D.G. Yu, and S.W. Bligh. Alginate-Based Electrospun Nanofibers and the Enabled Drug Controlled Release Profiles: A Review. *Biomolecules* 14(7): 789 (2024).
28. S.D. Santos, B. Medronho, T.D. Santos, and F.E. Antunes. Amphiphilic molecules in drug delivery systems. *Drug Delivery Systems: Advanced Technologies Potentially Applicable in Personalised Treatment* 4: 35-85 (2013).
29. J. Abildskov and J.P. O'Connell. Molecular thermodynamic modeling and design of microencapsulation systems for drug delivery. *Journal of Chemical & Engineering Data* 56: 1229-1237 (2011).
30. C.Y. Wang, H.O. Ho, L.H. Lin, Y.K. Lin, and M.T. Sheu. Asymmetric membrane capsules for delivery of poorly water-soluble drugs by osmotic effects. *International Journal of Pharmaceutics* 297(1-2): 89-97 (2005).
31. S.I. Palma, M. Marciello, A. Carvalho, S. Veintemillas-Verdaguer, M.M. del Puerto and A.C. Roque. Effects of phase transfer ligands on monodisperse iron oxide magnetic nanoparticles. *Journal of Colloid and Interface Science* 437: 147-155 (2015).
32. V.P. Torchilin. Structure and design of polymeric surfactant-based drug delivery systems. *Journal of Controlled Release* 73(2-3): 137-172 (2001).
33. M.A. Rub and A.Z. Naqvi. Micellization of Mixtures of Amphiphilic Drugs and Cationic Surfactants: A Detailed Study. *Colloids and Surfaces B: Biointerfaces* 92: 16-24 (2012).
34. K. Naseem, N.A. Khan, and S.H. Safeer. Effect of Magnesium Doping to Reduce the Charge Reservoir Layer in $Cu_{0.5}Tl_{0.5}(Ba_{2-x}Mg_x)Ca_2Cu_3O_y$ (x = 0, 0.15, 0.25, 0.35) Superconductors. *Journal of Electronic Materials* 5: 2164-2170 (2021).
35. G. Socrates (Ed.). Infrared and Raman Characteristic Group Frequencies: Tables and Charts. Third Edition. *John Wiley & Sons* (2004).
36. D. Cook. Vibrational spectra of pyridinium salts. *Canadian Journal of Chemistry* 39(10): 2009-2024 (1961).
37. R.J. Clark and C.S. Williams. The far-infrared spectra of metal-halide complexes of pyridine and related ligands. *Inorganic Chemistry Journal* (3): 350-357 (1965).
38. G.X. Zhao, B.Y. Zhu, Z.P. Dou, P. Yan, and J. X. Xiao. Effect of charge distribution along surfactant molecules on physico-chemical properties of surfactant systems. *Colloids and Surfaces A: Physicochemical and Engineering Aspects* 327(1-3): 122-126 (2008).
39. N.S. Gill, R.H. Nuttall, D.E. Scaife, and D.A. Sharp. The infra-red spectra of pyridine complexes and pyridinium salts. *Journal of Inorganic and Nuclear Chemistry* 18: 79-87 (1961).
40. A. Sager, S. Rahman, S.A. Imtiaz, Y. Zhang, A. Alodhayb, P.E. Georghiou, and M. Al-Gawati. Oxidative and Extractive Desulfurization of Fuel Oils Catalyzed by N-Carboxymethyl Pyridinium Acetate and N-Carboxyethyl Pyridinium Acetate Acidic Ionic Liquids: Experimental and Computational DFT Study. *American Chemical Society Omega* 9: 23121-24104 (2024).

41. S. Fayyaz, S. Ali, N. Khalid, A. Shah, and F. Ullah. One Pot Synthesis and Properties of Cationic Surfactants: n-Alkyl-3-Methylpyridinium Bromide. *Journal of Surfactants and Detergents* (4): 841-848 (2016).
42. T.Q. Liu and R. Guo. Influence of low cetyltrimethylammonium bromide concentration on the interactions and properties of hemoglobin with acyclovir. *Chinese Journal of Chemistry* 24(5): 620-626 (2006).
43. S.S. Shah, A. Saeed, and Q.M. Sharif, A study of micellization parameters and electrostatic interactions in micellar solution of sodium dodecyl sulfate. *Colloids and Surfaces A* 155(2-3): 405-412 (1999).
44. F.A. Shah, A.M. Khan, S. Sabir, and S. Ali. CTAB–tributylstannic [3-(3′, 4′-dichlorophenylamido) propanoate] interaction: a tool for predicting organotin (IV) complex–cell membrane interaction parameters. *Colloid and Polymer Science* 294(1): 87-94 (2016).
45. T.G. Kantor. Ketoprofen: a review of its pharmacologic and clinical properties. *Pharmacotherapy: The Journal of Human Pharmacology and Drug Therapy* 6(3): 93-102 (1986).
46. A.M. Khan and S.S. Shah. A UV-visible study of partitioning of pyrene in an anionic surfactant sodium dodecyl sulfate. *Journal of Dispersion Science and Technology* 29(10): 1401-1407 (2008).
47. H. Itoh, S. Ishido, M. Nomura, T. Hayakawa, and S. Mitaku. Estimation of the hydrophobicity in microenvironments by pyrene fluorescence measurements: n-β-octylglucoside micelles. *The Journal of Physical Chemistry* 100(21): 9047-9053 (1996).
48. B. Naseem, A. Sabri, A. Hasan, and S.S. Shah. Interaction of flavonoids within organized molecular assemblies of anionic surfactant. *Colloies and Surfaces B* 35(1): 7-13 (2004).
49. M.A. Awan and S.S. Shah. Hydrophobic interaction of amphiphilic hemicyanine dyes with cationic and anionic surfactant micelles. *Colloids and. Surfaces A* 122(1-3): 97-101 (1997).
50. H.A. Grema, Y.A. Geidam, G.B. Gadzama, J.A. Ameh, and A. Suleiman. Methicillin resistant Staphylococcus aureus (MRSA): a review. *Advances in Animal and Veterinary Sciences* 3(2): 79-98 (2015).
51. T.D. Tavares, J.C. Antunes, J. Padrão, A.I. Ribeiro, A. Zille, M.T.P. Amorim, F. Ferreira, and H.P. Felgueiras. Activity of specialized biomolecules against gram-positive and gram-negative bacteria. *Antibiotics* 9(6): 314 (2020).
52. X.Z. Li, P. Plésiat, and H. Nikaido. The challenge of efflux-mediated antibiotic resistance in Gram-negative bacteria. *Clinical Microbiology Reviews* 28(2): 337-418 (2015).

Proceedings of the Pakistan Academy of Sciences: A Physical and Computational Sciences 61(4): 361-371 (2024)

ISSN (Print): 2518-4245; ISSN (Online): 2518-4253
http://doi.org/10.53560/PPASA(61-4)872

Pakistan Academy of Sciences

Research Article

Fractional Order ANFIS Sliding Mode Controller for Two-Time Scale Dynamics in PWR

Arshad Habib Malik[1*], Feroza Arshad[2], and Aftab Ahmad Memon[3]

[1]Faculty of Engineering, Information and Technology, Sindh Institute of Management and Technology, Karachi, Pakistan

[2]Department of Information System Division, Karachi Nuclear Power Generating Station, Pakistan Atomic Energy Commission, Karachi, Pakistan

[3]Faculty of Electrical, Electronic and Computer Engineering, Mehran University of Engineering and Technology, Jamshoro, Sindh, Pakistan

Abstract: In this research work, a novel model of Pressurized Water Reactor (PWR) dynamics is developed with special emphasis on nuclear fuel burn-up or fuel depletion dynamics. PWR dynamics is identified and decomposed into fast and slow dynamic modes for the first time in this research work. The stiff two-time scale reactor dynamics problem is addressed, and a new sophisticated fractional order two-time scale sliding mode controller is designed. The PWR dynamics is uncertain due to three distinct operating conditions of nuclear reactor core as Beginning of Core (BOC), Middle of Core (MOC) and End of Core (EOC) synthesizing a variable structure model. The model uncertainties are estimated using Adaptive Neuro-Fuzzy Inference System (ANFIS) while different reactivity components are addressed as active disturbance or measurement noise. The novel robust control design problem is a big challenge in this research. The proposed controller is designed, tested and validated against benchmark data and found excellent in performance.

Keywords: Fractional Order Control, ANFIS, Two-Time-scale, Sliding Mode Control, Burn-up, PWR.

1. INTRODUCTION

Currently, control methods for PWRs are incapable of handling the dynamic uncertainties due to fuel burn-up and thermal reactivity variation under various conditions. The goal of this study is to design a flexible control system that takes into consideration these incalculable factors in order to keep a reactor in check in terms of steady and efficient operation. The reactor core model is developed through a lumped parameter thermo-neutronic coupled reactor dynamics. The dynamic behavior of the fuel burn-up is incorporated. Two new external reactivity controllers are designed; one with only thermal reactivity feedback and other with reactivity feedback due to fuel burn-up and poisons. A detailed literature review is conducted to address the modeling and controller design techniques in general and PWR in specific. Various linear, nonlinear, integer order, fractional order, neural, fuzzy, neuro-fuzzy and hybrid methods are studied, and their pros and cons are established. System dynamics with certainty and uncertainty are also studied so that a suitable and most accurate method could be established for PWR dynamics and control. An adaptive fractional order PID controller is designed for liquid level fine control system by Reddy *et al.* [1]. Similar study is also conducted for nuclear reactor point reactor kinetic model by Safarzadeh *et al.* [2]. A higher order observer is synthesized for PWR dynamics with thermal feedback by Ahmed *et al.* [3]. A point reactor kinetics-based model is developed for same PWR which is under consideration with thermal feedback and a nonlinear sliding mode observer is attempted by Hussain *et al.* [4]. This research provides a basis

Received: July 2024; Revised: November 2024; Accepted: December 2024
* Corresponding Author: Arshad Habib Malik <engr.dr.arshad.habib.malik@gmail.com>

for current research work to extend with more detailed dynamics and extended controller design. A fractional order adaptive neuro-fuzzy inference system (ANFIS) controller is attempted for droop control of wind turbine by Asgharpour-Alamdari [5] which is an intelligent control on fractional scale. A hybrid controller based on adaptive fuzzy fractional order sliding mode control technique is established for a dynamic system by Ullah *et al.* [6]. This is a class of uncertain system dynamics. Another hybrid controller based on adaptive fuzzy fractional order sliding mode control technique is formulated for micro gyroscope system by Liang and Fei [7]. This research uses a backstepping technique for nonlinear controller design. Similarly, a hybrid controller based on adaptive neural fractional order sliding mode control technique is established for micro electro-mechanical system (MEMS) by Fei and Lu [8]. This research uses a backstepping technique for nonlinear controller design. Another hybrid controller based on adaptive neural fractional order sliding mode control technique is addressed for ultrasonic motor by Chen *et al.* [9]. This design incorporates neural network compensation technique. A H_{∞} sliding mode controller is a different control design configuration adopted for 2500 MW_{th} PWR type nuclear reactor by Kirgni *et al.* [10]. Kalman filters, LQG and fractional order sliding mode controllers are designed for uncertain single input single output systems such as PWR reactor power control, reactor coolant temperature control, pressurizer level control, steam generator pressure control and turbine speed control by Surjagade *et al.* [11]. This is a comprehensive model-based controllers' design work and provides a strong basis to extend such fractional order nonlinear SMC for other systems with unique dynamics. A fractional order sliding mode controller is adopted for an uncertain nonlinear system by Zhang *et al.* [12] which is designed based on LQR technique. Research is further explored for ANFIS based sliding mode control for coupled tanks system by Boubakir *et al.* [13] which is a hybrid control design scheme comprising of intelligent control and nonlinear sliding mode control. A similar ANFIS based SMC is synthesized using Harmony Search Optimization technique by George and Mani [14]. An investigation is conducted for uncertain chaotic systems using ANFIS based sliding mode controller by Akbari *et al.* [15]. An adaptive neuro-fuzzy fractional order terminal sliding model controller is designed for micro gyroscope system using backstepping technique by Fei and Liang [16]. A multi-loop adaptive neuro-fuzzy fractional order sliding model controller is attempted for micro gyroscope system by Fang *et al.* [17]. In this research, a multivariable ANFIS based FO SMC is considered which provides a strong basis that new controller could be adopted with some new framework of model.

In this research work, a new model is proposed for reactor dynamics of PWR type nuclear power plant in two-time-scale framework with an addition of burn-up or fuel depletion modeling for the first time. A novel hybrid Fractional Order Adaptive Neuro-Fuzzy Inference System (ANFIS) based Two-Time-Scale Sliding Mode Controller (FO-ANFIS-TTS-SMC) is designed for proposed model of medium scale 300 MWe PWR nuclear power plant under BOC, MOC and EOC as variable nonlinear complex operating conditions of reactor core which formulates a unique complex challenging engineering and computing problem. The aim of this research work is to design and analyze the external reactivity controller for the control of reactor core thermal power, fuel and coolant temperatures of 998 MW_{th} Pressurized Water Reactor type Nuclear Power Plant.

2. MATERIALS AND METHODS

2.1. Modeling of PWR Dynamics

A 300 MWe PWR type nuclear power plant is considered for proposed design, simulation and analysis purposes. Various parameters/symbols and variables used hereafter in PWR dynamics modeling are adopted from Hussain *et al.* [4] while rest of parameters/symbols used in extended modeling and novel controller design are defined in Table 1. The PWR dynamic model is developed in time domain and space dependent effects are not considered throughout the modeling. The sampling interval is 0.001 second and the scale separation factor is 0.12. The exact values of the initial model parameters such as fuel temperature, coolant temperature, reactivity and burn-up are adopted from research work conducted for same PWR [4]. The dynamics of PWR reactor power is modeled as [4]:

$$\frac{dn_r(t)}{dt} = f_n((\rho_{net}, \beta_{eff}, \Lambda, n_r.C_r), t) \qquad (1)$$

Table 1. Symbols/parameters of model and controllers.

Parameters	Definitions
N	Number Density of Radio Nuclide
L	U-235, U-238, Pu-239, Pu-240, Pu-241
P	Poison Nuclide
K_∞	Infinite Multiplication Factor
γ	Yield Fraction
φ	Premise Variable
r	Fuzzy Sets
R	Fuzzy Rules
U	Control Input
X	State Vector
Y	Output Variable
δ	Uncertainty Nonlinear Function
D	Disturbance Nonlinear Function
I	1, 2,…..,n_1
J	1, 2,…..,n_2
μ	Scale Separation Factor
M	Identity Matrix
ψ	Normalized Membership Function
G	Constant Design Matrix
S	Sliding Mode Surface
D	Derivative Operator
I	Integral Operator
A	Fractional Order
$u_{Nom}^{USMC}(t)$	Nominal Control Law for Uncertain Sliding Mode Control (SMC) System
$u_{eq}^{FOUSMC}(t)$	Equivalent Control Law for Fractional Order Uncertain SMC System
K_μ	Gain of FO-ANFIS-TTS-SMC
ω_P	Neuro-Fuzzy Parameter
P	1, 2,…..,q
q	Number of Control Variables or Uncertainty Variables or Disturbance Variables
θ_P	Output of Rule Layer
$\overline{\delta}$	Uncertainty Model Output
$\overline{\omega}_P$	Ideal Value of Neuro-Fuzzy Parameter
$\Delta\omega_P$	Neuro-Fuzzy Parameter Error
ε	Unknown Parameter
τ	Design Constant
z	Special Design Variable
ρ	Adjustable Design Constant

The dynamics of precursors is modeled as:

$$\frac{dC_r(t)}{dt} = f_C((\lambda_{eff}, n_r.C_r), t) \tag{2}$$

The fuel temperature dynamics is modeled as:

$$\frac{dT_F(t)}{dt} = f_{T_F}((f_f, \mu_F, \Omega, n_r.T_F, T_C), t) \tag{3}$$

The coolant temperature dynamics is modeled as:

$$\frac{dT_C(t)}{dt} = f_{T_C}((f_f, \mu_C, \Omega, M, n_r.T_F, T_C, T_{in}), t) \tag{4}$$

The higher isotopes dynamics is modeled as:

$$\frac{dN^I(t)}{dt} = f_{N^I}((\delta_a^I; n_r.N^I, K_\infty), t) \tag{5}$$

The poisons' dynamics is modeled as:

$$\frac{dN^P(t)}{dt} = f_{N^P}((\delta_a^P; n_r.N^P, \gamma_P, \lambda_P), t) \tag{6}$$

2.2. Uncertain Two-Time Scale PWR Modeling

The PWR dynamics is uncertain due to three distinct operating conditions of reactor core. BOC, MOC and EOC are the beginning, middle and end of core fuel cycle conditions respectively. Reactor core parameters involve fast and slow dynamic modes. Fast modes are neutronic parameters such as precursors, burn-up and neutron power etc. while slow parameters are thermal parameters such as fuel temperature, and moderator / coolant temperature etc. Therefore, this is a two-time-scale problem of PWR dynamics.

The two-time-scale dynamics of PWR in state space form is given as:

$$\dot{x}_1(t) = A_{11}^j x_1(t) + A_{12}^j x_2(t) + B_1^j u(t) + B_1^j \delta(t) + B_{d_1}^j d(t) \tag{7}$$

$$\mu\dot{x}_2(t) = A_{21}^j x_1(t) + A_{22}^j x_2(t) + B_2^j u(t) + B_2^j \delta(t) + B_{d_2}^j d(t) \tag{8}$$

$$y(t) = c_1^j x_1(t) + c_2^j x_2(t) \tag{9}$$

Now, the two-time-scale dynamics of PWR can be formulated in terms of uncertain domain as:

$$M_\mu \dot{x}(t) = \sum_{j=1}^{n_2} \psi_R^j(\phi(t))[A^j x(t) + B^j u(t) + B^j \delta(t) + B_d^j d(t) \tag{10}$$

$$y(t) = \sum_{j=1}^{n_2} \psi_R^j(\phi(t)) c^j x(t) \quad (11)$$

2.3. Fractional Order ANFIS TTS SMC Modeling

The design framework of FO-ANFIS-TTS-SMC is shown in Figure 1. The proposed model is developed based on nonlinear singularly perturbed uncertain system dynamics, fractional calculus, sliding mode control and fractional order adaptive law.

The sliding mode surface for FO-ANFIS-TTS-SMC is basically a fractional order fuzzy sliding mode surface having constant design matrix satisfying invertible part with input matrix influenced by perturbation parameter within a finite time and robust performance and is defined as:

$$S(t) = GD^{1-\alpha}[M_\mu] - I^\alpha \left[G \sum_{j=1}^{n_2} \sum_{i=1}^{n_2} \psi_R^j(\phi(t)) \psi_R^j(\phi(t)).(A^j + B^j K_\mu^j) x(t) \right] \quad (12)$$

When states of uncertain two-time-scale system lies on the sliding mode surface S(t) then it holds the following condition:

$$D^\alpha S(t) = 0 \quad (13)$$

By substituting the value of $S(t)$ from equation (12) into equation (13), we get the equivalent control law for FO uncertain SMC is given as:

$$u_{eq}^{FOUSMC}(t) = \sum_{i=1}^{n_2} \psi_R^i(\phi(t)) K_\mu^i x(t) - \delta(t) = u(t) \quad (14)$$

Now, substituting the value of $u_{eq}^{FOUSMC}(t)$ from equation (14) into equation (10), the fractional order sliding mode dynamics can be calculated as:

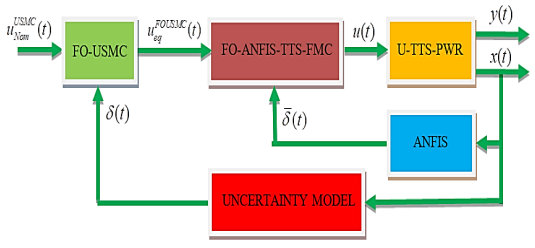

Fig. 1. Framework of FO-ANFIS-TSS-SMC for uncertain PWR dynamics.

$$M_\mu \dot{x}(t) = \sum_{j}^{n_2} \sum_{i=1}^{n_2} \psi_R^j(\phi(t)) \psi_R^i(\phi(t)) [(A^j + B^j K_\mu^I) x(t) + B_d^j d(t)] \quad (15)$$

ANFIS is used to identify the uncertainty model as:

$$\bar{\delta}(t) = \bar{\delta}_P(t) = w_P^T \theta_P(t) \quad (16)$$

The ideal neuro-fuzzy parameter is given as:

$$\tilde{w} = \tilde{w}_P = w_P - \Delta w_P \quad (17)$$

The desired control law can be deduced as:

$$u(t) = \sum_{i=1}^{n_2} \psi_R^i(\phi(t)) K_\mu^i x(t) - \tilde{w} \bar{\delta}(t) - \left(\sum_{j=1}^{n_2} \psi_R^j(\phi(t)) G B^j \right)^{-1} \cdot \frac{S(t)}{\|S(t)\|} z(t) \quad (18)$$

The $z(t)$ can be defined as:

$$z(t) = \varepsilon \left\| \sum_{i=1}^{n_2} \psi_R^j(\phi(t)) G B^j \right\| + \tau \quad (19)$$

Now, the ideal neuro-fuzzy parameter can be computed as:

$$D^\alpha \tilde{w}(t) = \rho S^T(t) \sum_{j=1}^{n_2} \psi_R^j(\phi(t)) G B^j \bar{\delta}(t) \quad (20)$$

3. RESULTS AND DISCUSSION

The closed loop functional analysis of the proposed design, performance analyses under different scenarios are discussed in the following sections.

3.1. Closed Loop Dynamic Functional Analysis of Proposed Design

The closed loop framework of reactor power transient system is shown in Figure 2. Change in reactor power will result change in neutron flux and thereby all reactivity components will change due to fissile, fertile and poison nuclides. Therefore, the reactivity due to fuel burn-up/fuel depletion dynamics will change and hence the net reactivity will change. The block diagram of closed loop framework system is shown in Figure 3. The block diagram incorporates all set-point signal, output signal, controller model, point reactor kinetics model, burn-up model, fission poison model,

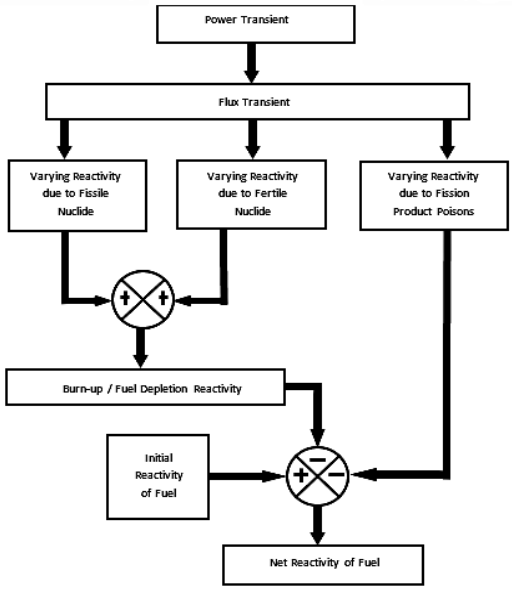

Fig. 2. Block diagram of reactor power transient framework.

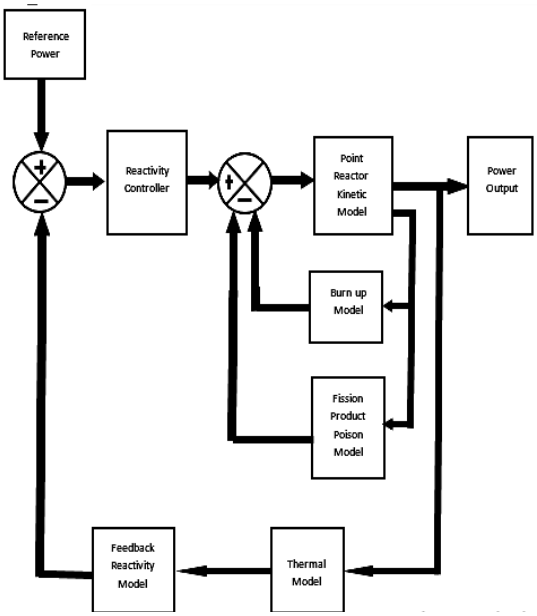

Fig. 3. Block diagram of closed loop system framework.

thermal model and reactivity model. The output of the reactivity feedback model is reactor power which is being utilized for thermal parameters.

3.2. Closed Loop Dynamic Performance Analysis of Proposed Design Under Different Scenarios

All the equations (1) through (20) are modeled in MATLAB Simulink environment and the integrated model is shown in Figure 4. The integrated simulation model is user friendly, and the operator/

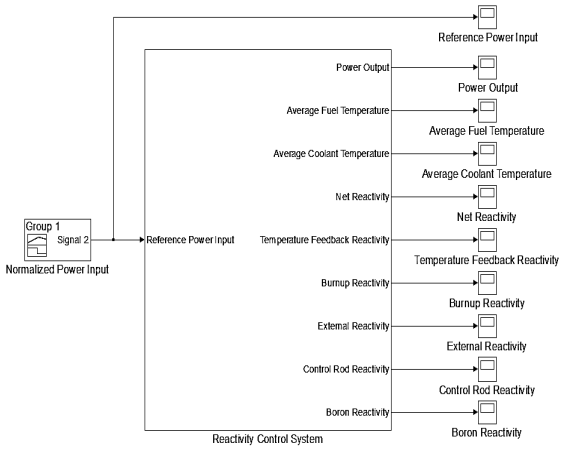

Fig. 4. Simulink closed loop model of FO-ANFIS-TTS-SMC for uncertain PWR dynamics.

designer/user set the desired target power and the designed parameters of interest are simulated and displayed accordingly. All model parameters shown in Figures (5-17) are basically reactivity components and are covered under reactor dynamics in terms of feedback so their dynamic behavior is deemed necessary for effectiveness of this research work in view of normal and stressed emergency operation of PWR.

This Simulink model shows a single block model of the reactivity control system considering all feedback. This model shows the input and outputs of the complete reactivity control system. Reference input power is the input to the control system while the normalized power output power, average fuel temperature, average coolant temperature, net reactivity, temperature feedback reactivity, burn-up reactivity, external reactivity, control rod reactivity and boron reactivity are the outputs.

The control design is attempted in two stages. In first stage, controller deals with external reactivity insertion or removal as control rod reactivity only. It has thermal reactivity feedback and to be analyzed and validated under normal load following operation and stressed emergency operation. In second stage, control system is multi-purpose control with additional feedback due to fuel burn-up and poisons. It incorporates reactivity control with Chemical Shim (Boron) as well as Control Rod as external reactivity controller and has capability of selection between the control mechanisms under specified conditions. It is to be

analyzed and validated under constant full power operation and partial low power operation with high and low power transient rate. Following configurable options are embedded in the proposed closed loop design:

1) Controller structure
2) Time domain (continuous or discrete)
3) Initial conditions and reset trigger
4) Output saturation limits
5) Signal tracking for bump-less control transfer and multi-loop control

The FO-ANFIS-TTS-SMC is the reactivity controller using Simulink environment. This controller model neither contains fuel burn-up and poison feedback reactivity nor reactivity compensation due to Boron concentration variation in the moderator. It has only thermal feedback reactivity and the control rod external reactivity. Therefore, this reactivity controller is assessed for power transients only.

The analysis of the reactivity controller with only thermal feedback is considered for two different scenarios. First scenario is normal load following operation while second scenario is stressed emergency operation. In normal load following operation, a load variation within 50–100% of nominal power at a ramp rate of 5% per minute is attempted.

Figure 5 shows the normal output power follows the normalized reference power input. Figure 6 shows the variation in temperature feedback reactivity, external reactivity and net reactivity for normal load following operation scenario. External reactivity follows the temperature profiles. Net reactivity has small non-zero values during power transient period.

Now, a stressed emergency operation is considered in which a load variation within from 100% to 30% of nominal power at a ramp rate of 15% per minute is attempted (Figures 7 and 8).

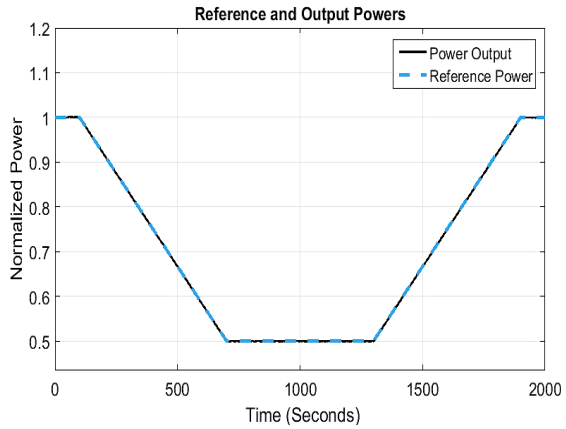

Fig. 5. Normal load following operation of PWR.

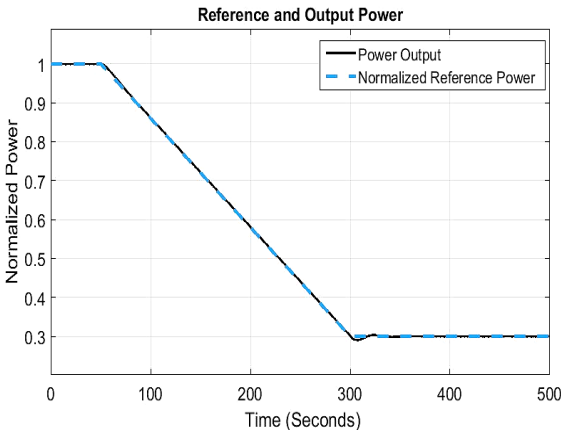

Fig. 7. Simulation of stressed emergency operation in PWR.

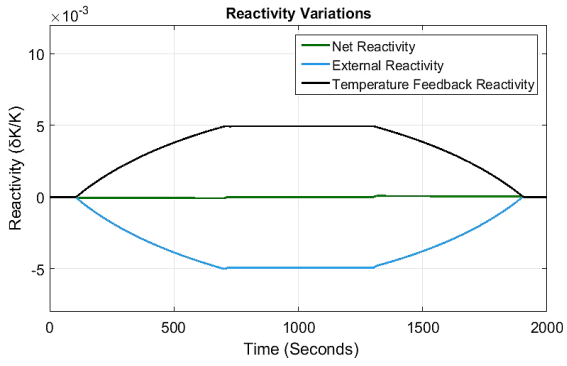

Fig. 6. Compensation of external reactivity with thermal feedback under normal load following operation in PWR.

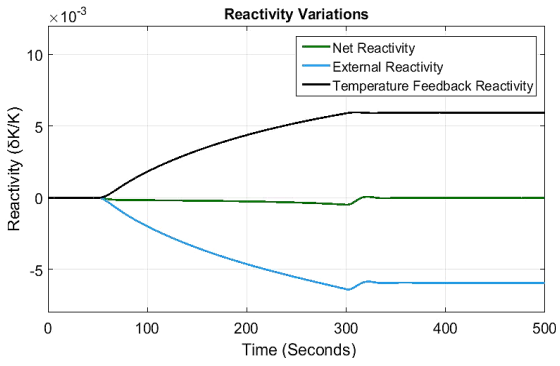

Fig. 8. Compensation of external reactivity with thermal feedback under stressed emergency operation in PWR.

Figure 9 shows the comparison of predicted boron reactivity with benchmark (FSAR). Boron reactivity model is validated by operating the reactor at constant full power for 380 days (i.e., one complete fuel cycle). Research is further extended for the reactivity controller with all feedback and both control rod reactivity and boron reactivity as external reactivity mechanisms for two different scenarios. First scenario is relatively higher power rate transient and other scenario is a lower power rate transient. During both the scenarios, reactor undergoes partial low power operation for 50 days during one complete cycle of the reactor operation.

In higher power rate transient operation, the reactor is operated at 50% power for 50 days after full power operation for 100 days. After 50 days, the reactor is again operated at full power for remaining next days of the reactor operation. The power transient rate is 10% per day. It is equivalent to 0.006944% per minute or 0.00011574% per second which is greater than lower bound i.e. 0.0000232% per second. This lower bound is the minimum power transient rate for the control rod reactivity insertion or removal and below this rate only boron will control the reactivity during the slower transient. So, the control rod must react for reactivity insertion and removal during this scenario.

Figure 10 shows the normal output power follows the normalized reference power input. Figure 11 shows the variation in all internal, external and net reactivity for higher transient rate operation scenario.

It is evident from this high-power rate transient that the burn-up reactivity for higher transient rate operation has a significant variation in it due to power transient as compared to that during full power operation. The temperature reactivity feedback has a small positive value during the transient. Control rod responded as expected during transient due to higher transient rate. Boron reactivity has a little more variation during transient than that during constant full power operation. External reactivity is the sum of the boron reactivity and control rod reactivity. Net reactivity is almost zero maintaining the reactor criticality.

In lower power rate transient operation, the reactor is operated at 90 % power for 50 days after full power operation for 100 days. After 50 days the reactor is again operated at full power for remaining next days of the reactor operation. The power transient rate is 2% per day. It is equivalent to 0.001389% per minute or 0.00023148% per second which is still lower than lower bound. So, the control rod must not react for reactivity insertion and removal during this scenario.

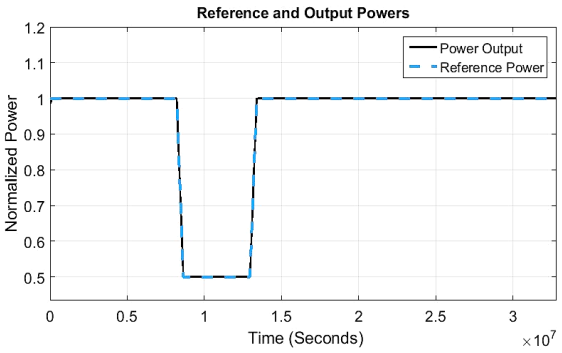

Fig. 10. Simulation of higher transient rate operation in PWR.

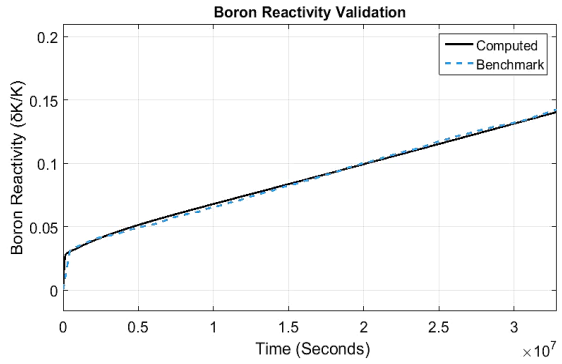

Fig. 9. Comparison of Boron reactivity with benchmark under lower rate operation in PWR.

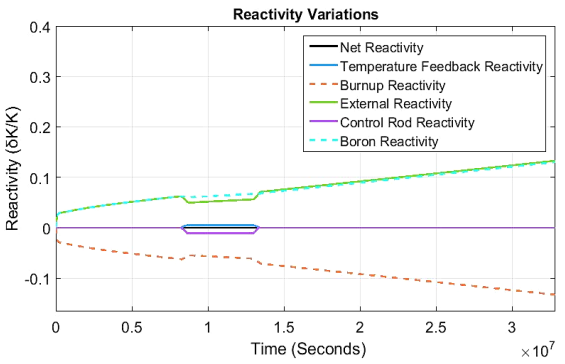

Fig. 11. Compensation of external reactivity with all feedback under higher rate operation in PWR.

Figure 12 shows the normal output power follows the normalized reference power input. Figure 13 shows the variation in all internal, external and net reactivity for lower transient rate operation scenario. It is evident from this low-power rate transient that the burn-up reactivity for lower transient rate operation has a small variation in it due to power transient as compared to that during full power operation. The temperature reactivity feedback has a small positive value during transient. Control Rod did not respond as expected during transient due to lower transient rate. Boron reactivity has a little more variation during transient than that during constant full power operation and during transient it compensates the temperature reactivity feedback because of no control action from control rod. External reactivity is the equivalent to the boron reactivity because control rod reactivity is zero. Net reactivity is almost zero maintaining the reactor criticality.

3.3. Validation of Proposed Closed Loop Design

Simulation results are validated by comparing the specific important parameters with benchmark values taken from Final Safety Analysis Report (FSAR) of PWR [4] core for same power perturbations. Validation of results for different scenarios are discussed below. Figure 14 shows comparison of steady state values of average coolant temperature for normal load following operation scenario. The range of y-axes of Figures (14-17) is so chosen to visualize the impact of both high and low power operations on same scale. The absolute error at 100% power is 0.1655% while at 50% power is 0.856%. Figure 15 shows comparison of steady state values of temperature feedback reactivity for normal load following operation scenario. This shows that there is small difference of 10 pcm in computed temperature feedback reactivity value and benchmark temperature feedback reactivity value. It is corresponded to small absolute error of 1.98%.

Figure 16 shows comparison of steady state values of average coolant temperature for stressed emergency operation scenario. The absolute error at 100% power is 0.1655% while at 30% power is 1.9%. Figure 17 shows comparison of steady state values of temperature feedback reactivity for stressed emergency operation scenario. This shows that there is small difference of 14 pcm in

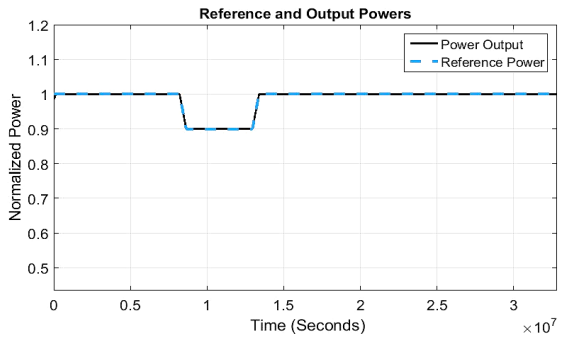

Fig. 12. Simulation of lower transient rate operation in PWR.

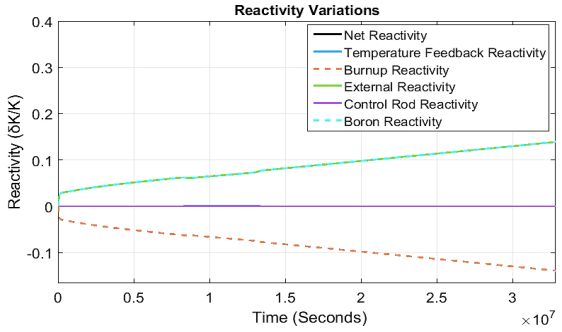

Fig. 13. Compensation of external reactivity with all Feedback under lower rate operation in PWR.

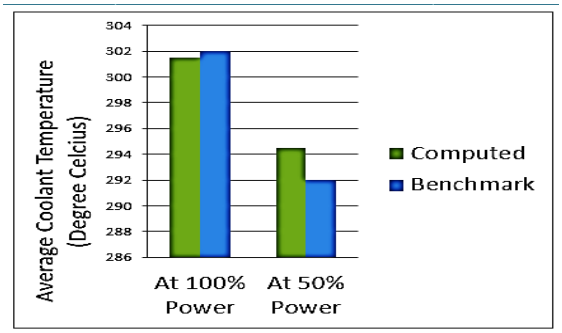

Fig. 14. Validation of average coolant temperature under normal load following operation of PWR.

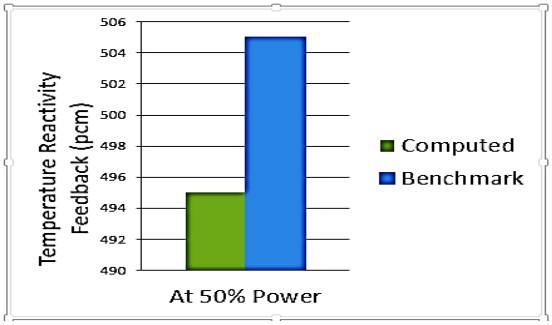

Fig. 15. Validation of thermal feedback under normal load following operation of PWR.

computed temperature feedback reactivity value and benchmark temperature feedback reactivity value. It is corresponded to a small error of 2.29%.

Figure 18 shows comparison of values of boron reactivity for constant full power operation scenario at the End of Cycle (EOC). This shows that there is a small difference of 0.003 δK/K in computed boron reactivity value and benchmark boron reactivity value. It is corresponded to an absolute error of 2.05 %. Figure 19 shows comparison of steady state values of average coolant temperature for higher transient rate operation scenario. The absolute error at 100% power is 0.1655% while at 50% power is 0.856%. Figure 20 shows comparison of steady state values of temperature feedback reactivity for higher transient rate operation scenario. There is small difference of 10 pcm in computed temperature feedback reactivity value and benchmark temperature feedback reactivity value. It is corresponded to a small absolute error of 1.98%. Figure 21 shows comparison of steady state values of average coolant temperature for lower transient rate operation scenario. The absolute error

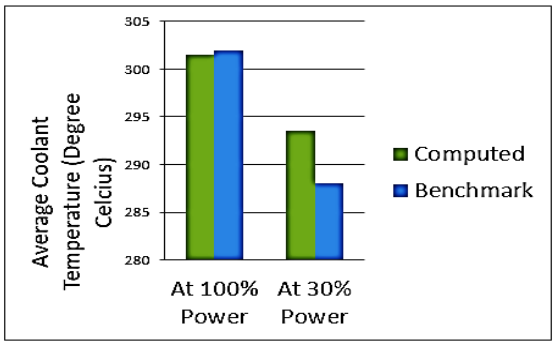

Fig. 16. Validation of average coolant temperature under stressed emergency operation of PWR.

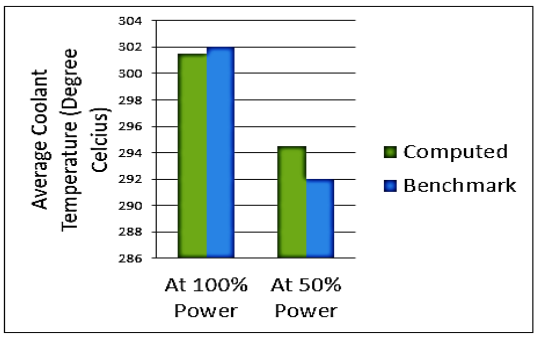

Fig. 19. Validation of average coolant temperature under high-rate operation of PWR.

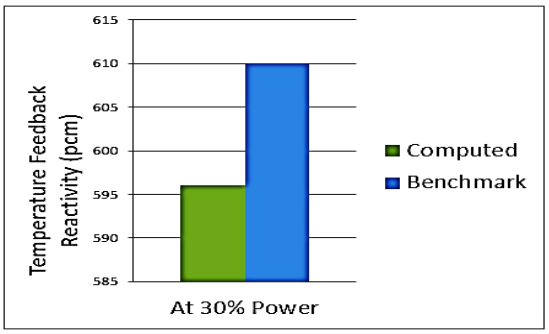

Fig. 17. Validation of thermal feedback under stressed emergency operation of PWR.

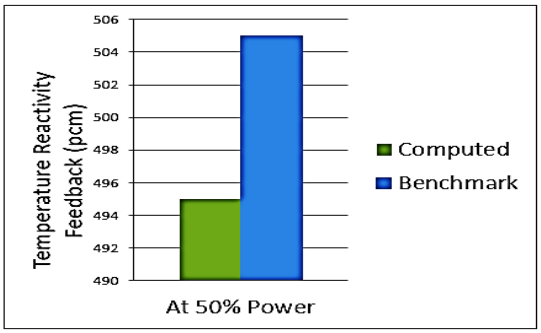

Fig. 20. Validation of thermal feedback under high-rate operation of PWR.

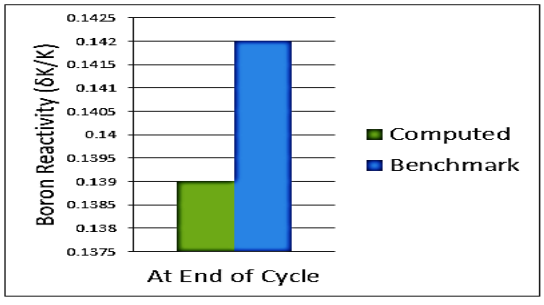

Fig. 18. Validation of Boron feedback under low-rate operation of PWR.

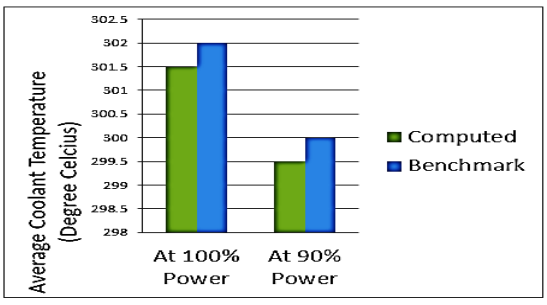

Fig. 21. Validation of average coolant temperature under low-rate operation of PWR.

at 100% power is 0.1655% while at 90% power is 0.167%. Figure 22 shows comparison of steady state values of temperature feedback reactivity for lower transient rate operation scenario. This shows that there is a difference of 6 pcm in computed temperature feedback reactivity value and benchmark temperature feedback reactivity value. It is corresponded to an absolute error of 3.87%.

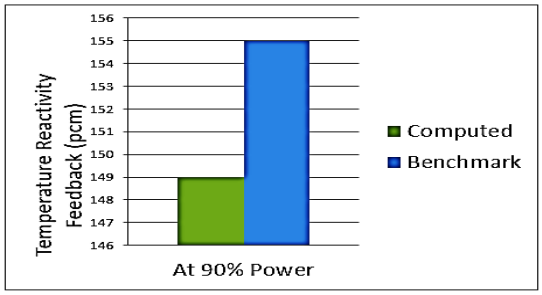

Fig. 22. Validation of thermal feedback under low-rate operation of PWR.

The desired objective of this research study is established for controlling PWR dynamics incorporating dynamic uncertainties due to fuel burn-up and thermal reactivity variation under various conditions in two-time-scale framework. The proposed scheme is proved effective by maintaining the net reactivity zero under all transient conditions. Simulation results prove that the proposed scheme is excellent in robust performance and the simulated results are most reliable as compared with benchmark results obtained from the operating PWR under the same standard conditions as mentioned in benchmark FSAR. The scope of this research work is justified after validating the results with benchmark results. The state transitions between the scales is computed and found 0.12 second. This time scale separation factor shows that dynamic behavior of reactivity components is so sharp and dynamic performance is bump less.

4. CONCLUSIONS

A lumped parameter thermo-neutronic model of PWR is developed in two-time scale framework. Fuel burn-up model is the new value addition in this research work. Fractional order ANFIS based two-time scale sliding mode external reactivity controller is designed for both control rod and boron reactivity control mechanisms and remarkable performance is observed. Simulation results prove that closed loop dynamics is robustly stable with a desired performance. The state trajectories of proposed closed loop system converge asymptotically with disturbance rejection and excellent robust stabilization is achieved in terms of settling time and overshoot. PWR dynamics model can be extended by incorporating other primary, balance of plant and secondary systems in future.

5. ACKNOWLEDGEMENTS

The support of Sindh Institute of Management and Technology, Information Support Division of KNPGS and Mehran University of Engineering and Technology, is gratefully acknowledged.

6. CONFLICT OF INTEREST

The authors declare no conflict of interest.

7. REFERENCES

1. A.S. Reddy and G.N. Reddy. An Adaptive Fractional Order Controller Design: A Realization for Liquid Level Regulation in Liquid Level Plant. *Measurement: Sensors* 31: 100977 (2024).
2. O. Safarzadeh and O. Noori-kalkhoran. A Fractional PID Controller based on Fractional Point Kinetic Model and Particle Swarm Optimization for Power Regulation of SMART Reactor. *Nuclear Engineering and Design* 377: 111137 (2021).
3. S. Ahmed, K.K. Abulraheem, A.O. Tolokonsky, and H. Ahmed. Active Disturbance Rejection Control of Pressurized Water Reactor. *Annals of Nuclear Energy* 189: 109845 (2023).
4. S. Hussain, A.I. Bhatti, A. Samee, and H. Qaiser. Estimation of Precursor Density of a Power Using Uniform Second Order Sliding Mode Observer. *Annals of Nuclear Energy* 54: 233-239 (2013).
5. H. Asgharpour-Alamdari. Optimal Fractional Order Adaptive Neuro Fuzzy Inference System based Droop Controller for DFIG Wind Turbine to Control Load Frequency of Hybrid Microgrid. *Journal of Numerical Modelling: Electronic Networks* 35: e2942 (2021).
6. N. Ullah, S. Han, and M. Khattak. Adaptive Fuzzy Fractional Order Sliding Mode Controller for a Class of Dynamical Systems with Uncertainty. *Transactions of the Institute of Measurement and Control* 38(4): 402-413 (2016).
7. X. Liang and J. Fei. Adaptive Fractional Fuzzy Sliding Mode Control of Micro-gyroscope based

on Backstepping Design. *Plos One* 14(6): e0218425 (2019).

8. J. Fei and C. Lu. Adaptive Fractional Order Sliding Mode Controller with Neural Estimator. *Journal of the Franklin Institute* 355(5): 2369-2391 (2018).
9. X. Chen, W. Liang, H. Zhao, and A.A. Mamun. Adaptive Fractional Order Sliding Mode Controller with Neural Network Compensator for an Ultrasonic Motor. *ArXiv Preprint ArXiv:2103.12327* (2021).
10. H.B. Kirgni, J. Wang, and A. Asif. Static output Feedback H_∞ based Integral Sliding Mode Control Law Design for Nuclear Reactor Power Level. *Progress in Nuclear Energy* 150*:* 104296 (2022).
11. P.V. Surjagade, J. Deng, V. Vajpayee, V.M. Becerra, S.R. Shimjith, and A.J. Arul. Fractional Order Integral Sliding Mode Control of PWR Nuclear Power Plant. *European Control Conference, (12th – 15th July 2022), London, United Kingdom* (2022).
12. D. Zhang, L. Cao, and S. Tang. Fractional Order Sliding Mode Control for a Class of Uncertain Nonlinear Systems based on LQR. *International Journal of Advanced Robotic Systems* 14(2): 1-15 (2017).
13. A. Boubakir, F. Boudjema, and S. Labiod. A Neuro-Fuzzy Sliding Mode Controller Using Nonlinear Sliding Surface Applied to the Coupled Tanks System. *International Journal of Automation and Computing* 6: 72-80 (2009).
14. J. George and G. Mani. A Portrayal of Sliding Mode Control through Adaptive Neuro Fuzzy Inference System with Optimization Perspective. *IEEE Access* 12: 3222-3239 (2024).
15. K. Akbari, B. Rezaie, and S. Khari. Designing Full order Sliding Mode Controller based on ANFIS Approximator for Uncertain Nonlinear Chaotic Systems. *International Journal of Industrial Electronics, Control and Optimization* 2(1): 39-46 (2019).
16. J. Fei and X. Liang. Adaptive Backstepping Fuzzy Neural Network Fractional Control of Micro-gyroscope using a Nonsingular Terminal Sliding Mode Controller. *Complexity* 2018: 246074 (2018).
17. Y. Fang, F. Chen, and J. Fei. Multiple Loop Fuzzy Neural Network Fractional Order Sliding Mode Control of Micro Gyroscope. *Mathematics* 9(17): 2124 (2021).

Proceedings of the Pakistan Academy of Sciences: A Physical and Computational Sciences 61(4): 373-379 (2024)

ISSN (Print): 2518-4245; ISSN (Online): 2518-4253
http://doi.org/10.53560/PPASA(61-4)683

Pakistan Academy of Sciences

Research Article

Resilience of Antibiotic Usage and Vital Signs in COVID-19 Patients: A Post-Pandemic Analysis in Pakistan

Muhammad Islam[1*], Imtiaz Ahmed[2], Muhammad Shehzad[3], and Kashif Nadeem[4]

[1]Crop Reporting Service (Bahawalpur), Agriculture Department, Punjab, Pakistan

[2]Punjab Land Records Authority (Bahawalpur Saddar), Board of Revenue Punjab, Pakistan

[3]Crop Reporting Service Lahore (Admin. Branch), Agriculture Department, Punjab, Pakistan

[4]Crop Reporting Service (Rahim Yar Khan), Agriculture Department, Punjab, Pakistan

Abstract: COVID-19 has had a profound global impact, wreaking havoc on economies and causing a significant loss of lives. Pakistan has also faced severe consequences from the pandemic. To combat the virus, antibiotics such as Azithromycin, Ceftriaxone, Cefixime, Clarithromycin, Levofloxacin, Moxifloxacin, Meropenem, Tazobactam, Tienam, and Vancomycin have been administered to COVID-19 patients. Various vital signs such as temperature, respiratory rate, oxygen saturation, pulse rate, and blood pressure have been closely linked to the symptoms of COVID-19. This study examines the impact of antibiotic usage and vital signs on the survival and mortality of COVID-19 patients using a dataset collected from four major hospitals in Pakistan. The analytical approach includes descriptive analysis, a t-test, and a chi-square test of independence. The originality of this research lies in its comprehensive exploration of the relationship between specific antibiotics and the monitoring of vital signs in the context of COVID-19. It offers a systematic analysis of existing information to derive meaningful insights. Azithromycin emerged as the predominant antibiotic used to treat COVID-19 patients in Pakistan, with other antibiotics showing varying usage patterns. Strong, significant associations were identified between Azithromycin, Tazobactam (Tanzo), and the binary response variable (died/alive). Regarding vital signs, significant relationships were observed for patient age, systolic blood pressure, and diastolic blood pressure when compared to the response variable. This study's findings underscore the importance of Azithromycin and Tazobactam in COVID-19 treatment and highlight the role of vital signs in predicting patient outcomes.

Keywords: Antibiotic Levels, Vital Signs, Survival and Mortality, Post COVID Patients Analysis.

1. INTRODUCTION

The year 2020 is not as fanciful due to the spreading and overwhelming figures of Coronavirus disease (COVID-19) [1, 2]. Millions of people have been affected due to the horrible threat of COVID-19 around the world [3]. It is a drastic fact that the COVID-19 pandemic has remodeled the fabric of society, clipped the human psyche, influenced public policies, redefined business horizons, and redesigned interpersonal relations around the globe. The COVID-19 has severely affected the world economies. The outbreak of COVID-19 was first experienced in Wuhan, China at the end of December 2019 and then it rapidly spread worldwide in almost 209 countries in America, Europe, Australia, Africa, and Asia [4, 5]. Worldwide, COVID-19 is responsible for a huge no. of deaths. COVID-19 is also a heinous issue for the Pakistan's healthcare sector. Pakistan's economy was vulnerable to offer the high level of COVID-19 treatment set by the World Health Organization (WHO) [5, 6]. COVID-19 is a virus that most frequently attacks the human respiratory system. The WHO had classified the COVID-19 epidemic in Pakistan as the Sixth Public Health of Emergency Services (SPHEC). Pakistan has made strong efforts to eradicate the spread of COVID-19 by creating special laboratories, hospital wards, quarantine, awareness campaigns, and lockdowns.

Received: October 2024; Revised: November 2024; Accepted: December 2024
* Corresponding Author: Muhammad Islam <mislam6667@gmail.com>

Coronavirus is a contagious disease attributed to the most recently discovered severe acute respiratory syndrome coronavirus-2 (SARs-COV-2). Arshad *et al.* [7] emphasized trials to study the combination impact of hydroxychloroquine and azithromycin for the treatment of positive COVID-19 patients and they reported that the combination of hydroxychloroquine and azithromycin was associated with reduced mortality. Miranda *et al.* [8] highlighted that the absence of reliable statistics on antimicrobial usage during the COVID-19 pandemic poses a significant challenge to effective public health policy formulation and strategic planning. Gautret *et al.* [9] reported that the COVID-19 virus was significantly eliminated when azithromycin was added to hydroxychloroquine in a clinical trial. Echeverria-Esnal *et al.* [10] revealed that azithromycin behaved well against a different viral cycle of SARS-CoV-2 and it reduced the risk of mortality as well as the ventilation period. Gonzalez-Zorn [11] reported that the use of four antibiotics i.e. amoxicillin, erythromycin, cefixime, and levofloxacin was significant in curing the COVID-19 pandemic. Langford *et al.* [12] reported that unnecessary use of antibiotics was likely to be high in COVID-19 patients. The different vital signs (physiological measurements) i.e. Temperature, Respiratory rate, Oxygen saturation, Pulse rate, blood pressure, and Level of consciousness are associated with the symptoms of COVID-19. Different antibiotics i.e. Azithromycin, Ceftriaxone, Cefixine, Chlathromycin, Levofloxacin, Moxifloxacin, Meranum, Tanzo, Tienum, and Vancomycin had been administered in Pakistan for the treatment of COVID-19.

In Pakistan, different antibiotics such as Azithromycin, Ceftriaxone, Cefixime, Clarithromycin, Levofloxacin, Moxifloxacin, Meropenem, Tanzo, Tienam, and Vancomycin were administered to treat COVID-19 patients in different hospitals. However, there is a lack of detailed post-COVID-19 studies in Pakistan showing which level/dose of antibiotics are significantly associated with survival and mortality of COVID-19 patients, which level can prevent the patient from major casualties, and which level/dose of antibiotics can be helpful for better treatment. Vital signs (physiological measurements) such as temperature, respiratory rate, oxygen saturation, pulse rate, and blood pressure are closely linked to COVID-19 symptoms. In Pakistan, no post-COVID-19 study has been carried out which is evident whether vital signs (physiological measurements) are statistically associated and helpful for detecting COVID-19 pandemic symptoms. The absence of post-COVID-19 studies in Pakistan focusing on antibiotic levels and vital signs makes this research highly original and impactful. This research seeks to address these critical gaps in understanding for more effective patient management and treatment. This study is based on cross-sectional statistical analysis to elaborate:

1. Which level/ dose of antibiotics are significantly associated with survival and mortality of COVID-19 patients, which level can prevent major casualties, and which level of antibiotics can ensure better treatment measures for the patients admitted in the hospitals of Pakistan?
2. Whether vital signs (physiological measurements) i.e. temperature, respiratory rate, oxygen saturation, pulse rate, and blood pressure are associated and helpful for detecting COVID-19 symptoms.
3. To layout some recommendations about the usefulness of different antibiotics and the effects of vital signs (physiological measurements) for detecting COVID-19 symptoms.

2. MATERIALS AND METHODS

2.1. Data Collection and Variables Descriptions

This study utilizes secondary data collected from four major hospitals in Rawalpindi and Islamabad, including the Pakistan Institute of Medical Sciences Hospital, Pakistan Air Force Hospital, Benazir Bhutto Shaheed Hospital, and Holy Family Hospital. The dataset comprises information from 1806 COVID-19 patients spanning from February to August 2020. The data includes vital medical signs such as temperature, respiratory rate, oxygen saturation, pulse rate, systolic blood pressure, and diastolic blood pressure, as well as the administration of various levels of antibiotics, including Azithromycin, Ceftriaxone, Cefixime, Clarithromycin, Levofloxacin, Moxifloxacin, Meropenem, Tanzo, Tienam, and Vancomycin. Patient status (alive/died) is also recorded for analysis. Vital medical signs are treated as quantitative measures, while antibiotics are categorized into three levels for examination.

A_0 = when no antibiotics are given to COVID-19

patients.
A_l = when a low dose of antibiotics is given to COVID-19 patients.
A_h = when a high dose of antibiotics is given to COVID-19 patients.

2.2. Statistical Data Analysis

The statistical analysis is carried out in the following steps:

1. Descriptive statistical analysis is performed using counts, percentages, mean, and standard deviation for the variables of interest.
2. The chi-square (χ^2) test is used to determine whether there is a significant association between two categorical variables i.e. died/alive against different antibiotics levels.

$$\chi 2 = \sum \frac{(O_i - E_i)^2}{E_i} \quad (1)$$

Where "O_i" defined the observed values and "E_i" defined the expected values in the datasets of interest. The hypothesis is set as:
H_0: There is no significant difference existing for died/alive against different levels of antibiotics applied.
H_1: There is a significant difference existing for dead/alive against different levels of antibiotics applied.

3. T-test is applied to measure the significance of died/alive against different vital signs (physiological measurements) i.e. respiration rate, body temperature, oxygen saturation level, pulse rate, and blood pressure.

$$t_{\bar{\theta}} = \frac{\phi - \theta}{\frac{s}{\sqrt{n}}} \quad (2)$$

Where "ϕ" is the mean of sample data, "θ" overall mean of the dataset, "s" is the standard deviation, and "n" stands for the sample size. The hypothesis set as:
H_0: There is no significant difference between dead/alive against different vital signs.
H_1: There is a significant difference between dead/alive against different vital signs.

3. RESULTS

3.1. Significance of Different Levels of Antibiotics and Died/Alive

Table 1 shows the association for different levels of antibiotics against the response variable died/alive. For azithromycin 208 (11.5%) patients were treated with "A_o", 113 (6.3%) with "A_l" and 1485 (82.2%) with "A_h". For azithromycin, 143 (69%) were alive and 65 (31%) have died for level "A_0", 74 (65%) were alive and 39 (35%) died from level "A_l", 1124 (76%) were alive and 361 (24%) were died of level "A_h". For the Ceftriaxone 1380 (76.4%) patients were treated with "A_0", 214 (11.8%) with "A_l" and 212 (11.7%) with "A_h". For Cefatriaxone, 1021 (74%) were alive and 359 (26%) died for level "A_0", 166 (78%) were alive and 48 (22%) died from level "A_l", 154 (73%) were alive and 58 (27%) were died for level "A_h". Figure 1 illustrates that the maximum number of patients are given high levels of antibiotics "A_h" for azithromycin, while it is found vice versa for all other antibiotics. The Chi-square and p-value found 9.44 and 0.009 for azithromycin, 7.32 and 0.026 for Tanzo. There is a strong association exist between the antibiotic Azithromycin and Tanzo with the binary response variable died/alive. For Tienum, Moxifloxacin, Cefixine, Levofloxacin, Vancomycin, Chlathromycin, and Meranum, the p-value reported as 0.322, 0.147, 0.446, 0.969, 0.712, 0.922 and 0.877. All these p-values found greater than 5% level of significance. There is no association exists between Tienum, Moxifloxacin, Cefixine, Levofloxacin, Vancomycin, Chlathromycin, and Meranum for response variable died/alive, while it is reported statistically strong associations between Azithromycin and Tanzo with response variable died/alive.

3.2. Significance of Different Vital Signs and Response Variable Died/Alive

Table 2 shows the degree of relation between different vital signs (physiological measurements) and the response variable died/alive. The mean age of patients was found to be 47.38 with a standard deviation of 17.17. For patients' age high value of standard deviation indicates a larger variation among the ages of COVID-19 patients, while found lowest for body temperature. For the respiratory rate, 24.14 breaths per minute indicates a very serious condition [13, 14]. The average temperature of the human body was found 99.15 with the lowest standard deviation of 1.20, which indicates the temperature of COVID-19 patients varies in the normal range. The 88.48% saturation oxygen level with a standard deviation of 12.54 is considered a low oxygen level.

Table 1. Significance of different levels of antibiotics and response variable died/alive.

Antibiotics	Levels	Count (%)	Alive	Died	Chi-Sq	p-Value
Azithromycin	None (A_0)	208(11.5)	143 (69)	65 (31)	9.44	0.009
	Low (A_l)	113(6.3)	74 (65)	39 (35)		
	High (A_h)	1485(82.2)	1124 (76)	361 (24)		
Cefatriaxone	None (A_0)	1380(76.4)	1021 (74)	359 (26)	1.57	0.456
	Low (A_l)	214(11.8)	166 (78)	48 (22)		
	High (A_h)	212(11.7)	154 (73)	58 (27)		
Tienum	None (A_0)	1643(91)	1227 (75)	416 (25)	2.26	0.322
	Low (A_l)	39(2.2)	29 (74)	10 (26)		
	High (A_h)	124(6.9)	85 (69)	39 (31)		
Tanzo	None (A_0)	1509(83.6)	1104 (73)	405 (27)	7.32	0.026
	Low (A_l)	97(5.4)	82 (85)	15 (15)		
	High (A_h)	199(11)	154 (77)	45 (23)		
Moxifloxacin	None (A_0)	1783(98.7)	1328 (74)	455 (26)	3.83	0.147
	Low (A_l)	16(0.9)	9 (56)	7 (44)		
	High (A_h)	7(0.4)	4 (57)	3 (43)		
Cefixine	None (A_0)	1798(99.6)	1336 (74)	462 (26)	0.58	0.446
	Low (A_l)	8(0.04)	5 (63)	3 (38)		
	High (A_h)	0	0	0		
Levofloxacin	None (A_0)	1785(98.8)	1325 (74)	460 (26)	0.06	0.969
	Low (A_l)	9(0.5)	7 (78)	2 (22)		
	High (A_h)	12(0.7)	9 (75)	3 (25)		
Vancomycin	None (A_0)	1794(99.3)	1331 (74)	463 (26)	0.68	0.712
	Low (A_l)	11(0.6)	9 (82)	2 (18)		
	High (A_h)	1(0.1)	1 (100)	0		
Chlathromycin	None (A_0)	1772(98.1)	1316 (74)	456 (26)	0.16	0.922
	Low (A_l)	17(0.9)	12 (71)	5 (29)		
	High (A_h)	17(0.9)	13 (76)	4 (24)		
Meranum	None (A_0)	1744(96.6)	1294 (74)	450 (26)	0.26	0.877
	Low (A_l)	48(2.7)	37 (77)	11 (23)		
	High (A_h) (	14(0.8)	10 (71)	4(29)		

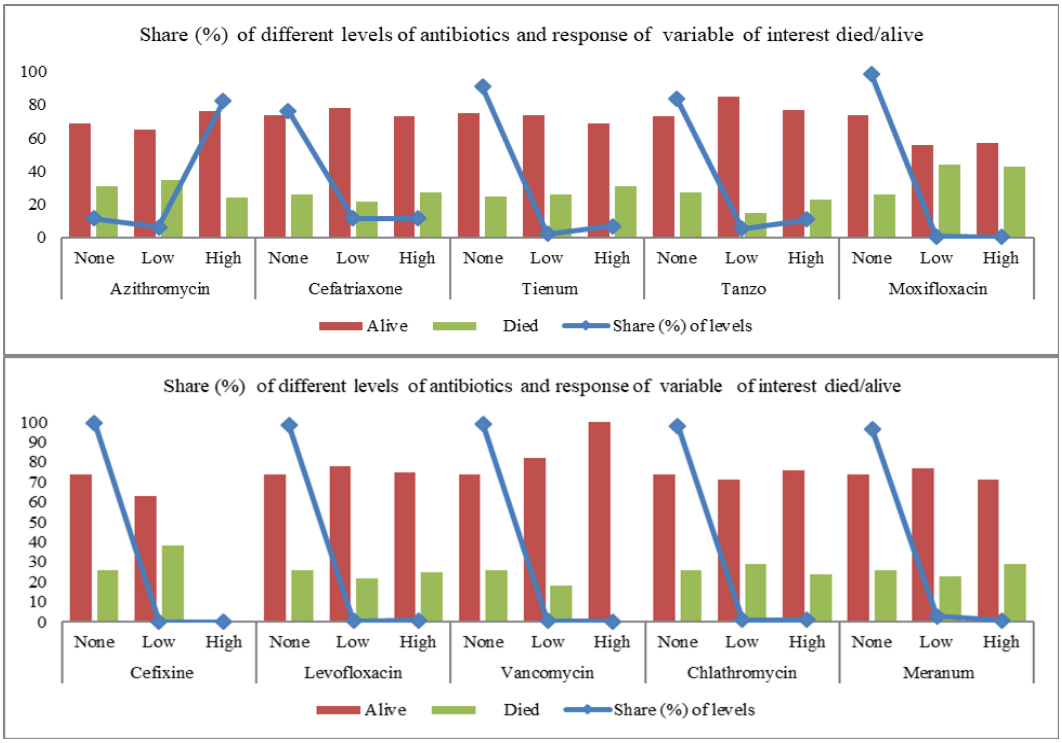

Fig. 1. Share (%) of different antibiotic levels and the response of variable died/alive.

Table 2. Relation between the vital signs and response variable died/alive.

Vital signs	Mean	Standard deviation	t-value	p-value
Age of patients	47.38	17.17	18.723	0.00
Respiratory Rate	24.14	8.95	-0.707	0.476
Body Temperature	99.15	1.20	0.717	0.476
Oxygen saturation level	88.48	12.54	1.344	0.179
Systolic blood pressure	120.09	18.70	-2.117	0.034
Diastolic blood pressure	77.28	12.53	-2.116	0.035
Pulse rate	89.48	14.74	0.559	0.576

The value of standard deviation was found 18.70, 12.53, and 14.74 respectively for systolic blood pressure, diastolic blood pressure, and pulse rate, which are considerably large variations. The p-value was found less than 0.05 for the age of the patient, systolic blood pressure, and diastolic blood pressure, which indicates there is statistically significant relation exists for these variables against response variables died/alive, while all other vital signs yield statistically insignificant relation for the response variable died/alive.

4. DISCUSSION

Several studies have examined the application pattern of antibiotics in COVID-19 patients. Estrada *et al.* [15], Fiol *et al.* [16], Akhtar *et al.* [17], Mansoor *et al.* [18], Saeed *et al.* [19], and Alvi *et al.* [20] conducted similar investigations. They found that bacterial co-infections were infrequent among COVID-19 patients, yet the utilization of antibiotics was widespread. There was promising evidence suggesting that azithromycin could serve as a potential treatment for COVID-19. Clear and specific guidelines are essential for establishing a targeted treatment to minimize associated risks and inappropriate use of antibiotics. Mustafa *et al.* [21], and Farooqui *et al.* [22] also confirmed the alarming issue of suboptimal antibiotic usage and its consequential contribution to antibiotic resistance. Their research reveals a worrisome trend of excessive antibiotic consumption among hospitalized patients with suspected or confirmed COVID-19 patients in Pakistan. Gul *et al.* [23] also emphasized the urgent need for pharmacist and pharmacy technician programs to curb antibiotic misuse and combat antimicrobial resistance (AMR). Urgent attention is needed to combat the unnecessary prescription of antibiotics in the context of COVID-19 infection. This research examined the three levels of ten different antibiotics and confirmed that the majority of patients received high level antibiotics in the case of azithromycin, while the pattern was reversed for all other antibiotics i.e. Ceftriaxone, Cefixine, Chlathromycin, Levofloxacin, Moxifloxacin, Meranum, Tanzo, Tienum, and Vancomycin Furthermore, a strong association was identified between the use of azithromycin and Tanzo with the binary response variable died/alive. Haq *et al.* [24] found that COVID-19 mortality in Pakistani hospitalized patients was linked to demographic factors, clinical lab characteristics, oxygen saturation, and late admission. Aksel *et al.* [25], and Qureshi *et al.* [26] applied a similar study and found that vital signs significantly influenced the survival and mortality of COVID-19. Similarly, Jeong *et al.* [27] identified that cough, fever, nasal congestion, and diarrhea are key symptoms for establishing comprehensive COVID-19 screening criteria. This study extended the vital signs (physiological measurements) to temperature, respiratory rate, oxygen saturation, pulse rate, and blood pressure with the survival and mortality of COVID-19 patients, which had not been studied earlier. The mean age of patients indicates a larger variation while the temperature of COVID-19 patients varies within the normal range. The 88.48% saturation oxygen level with a standard deviation of 12.54 was considered a low oxygen level. Large variations were found for blood pressure and pulse rate. The age of the patient and blood pressure were found to be statistically significant.

5. CONCLUSIONS

The year 2020 is not as fanciful due to the spreading figures of COVID-19. Worldwide, COVID-19

was responsible for significant casualties and posed a severe challenge for Pakistan. Different vital signs (physiological measurements) i.e. temperature, respiratory rate, oxygen saturation, pulse rate, and blood pressure are associated with the symptoms of COVID-19 and different antibiotics i.e. Azithromycin, Ceftriaxone, Cefixine, Chlathromycin, Levofloxacin, Moxifloxacin, Meranum, Tanzo, Tienum, and Vancomycin had been administrated to treat the COVID-19. No detailed post-COVID-19 research has been conducted in Pakistan to study the significance and associations of antibiotic levels and vital signs with survival and mortality in COVID-19 patients.

This study provides evidence of which antibiotic levels and vital signs significantly influence the survival and mortality of COVID-19 patients. The secondary data of 1806 COVID-19 patients are used and three levels of antibiotics are studied. Descriptive statistical analysis, chi-square, and t-test are applied to assess the significance of died/alive against antibiotics levels and vital signs. Maximum numbers of patients were given high levels of antibiotics for azithromycin, while it is found vice versa for all other antibiotics. The strong significant associations reported for Azithromycin and Tanzo with the binary response variable died/alive, while all other antibiotics levels yield statistically insignificant results. For vital signs, a high standard deviation was found for the ages of COVID-19 patients. The temperature of COVID-19 patients varies in a normal range. High standard deviations were found for systolic blood pressure, diastolic blood pressure, and pulse rate. Statistically significant relation exists for the age of the patient, systolic blood pressure, and diastolic blood pressure against response variables died/alive, while all other vital signs yield insignificant results. This study provides a foundation for formulating enhanced recommendations and identifying future research areas by leveraging predictive modeling through machine learning and statistical techniques. It focuses on the interplay between antibiotic levels and vital signs to effectively detect and monitor the deterioration of patients afflicted with various severe diseases.

6. CONFLICT OF INTEREST

All authors affirm that they have no conflict of interest.

7. REFERENCES

1. J.I.F. Salluh, T. Lisboa, and F.A. Bozza. Challenges for the care delivery for critically ill COVID-19 patients in developing countries: The Brazilian perspective. *Critical Care* 24: 593 (2020).
2. D.M. Morens, J.K. Taubenberger, and A.S. Fauci. A centenary tale of two pandemics: The 1918 influenza pandemic and COVID-19, part I. *American Journal of Public Health* 111(6): 1086-1094 (2021).
3. S.A. Lee and R.A. Neimeyer. Pandemic Grief Scale: A screening tool for dysfunctional grief due to a COVID-19 loss. *Death Studies* 46(1): 14-24 (2022).
4. A. Waris, U.K. Atta, M. Ali, A. Asmat, and A. Baset. COVID-19 outbreak: current scenario of Pakistan. *New Microbes and New Infections* 35: 100681 (2020).
5. M. Atif and I. Malik. Why is Pakistan vulnerable to COVID-19 associated morbidity and mortality? A scoping review. *The International Journal of Health Planning and Management* 35(5): 1041-1054 (2020).
6. O.D. Williams. COVID-19 and private health: market and governance failure. *Development* 63(2): 181-190 (2020).
7. S. Arshad, P. Kilgore, Z.S. Chaudhry, G. Jacobsen, D.D. Wang, K. Huitsing, I. Brar, J.G. Alangaden, M.S. Ramesh, J.E. McKinnon, W.O. Neill, and M. Zervos. Treatment with hydroxychloroquine, azithromycin, and combination in patients hospitalized with COVID-19. *International Journal of Infectious Diseases* 97: 396-403 (2020).
8. C. Miranda, V. Silva, R. Capita, C. Alonso-Calleja, G. Igrejas, and P. Poeta. Implications of antibiotics use during the COVID-19 pandemic: present and future. *Journal of Antimicrobial Chemotherapy* 75(12): 3413-3416 (2020).
9. P. Gautret, J. Lagier, P. Parola, V.T. Hoang, L. Meddeb, M. Mailhe, B. Doudier, J. Courjon, V. Giordanengo, V.E. Vieira, H.T. Dupont, S. Honore, P. Colson, E. Chabriere, B.L. Scola, J.M. Rolain, P. Brouqui, and D. Raoult. Hydroxychloroquine and azithromycin as a treatment of COVID-19: results of an open-label non-randomized clinical trial. *International Journal of Antimicrobial Agents* 56(1): 105949 (2020).
10. D. Echeverria-Esnal, C. Martin-Ontiyuelo, M.E. Navarrete-Rouco, M.D.A. Cusco, O. Ferrandez, J.P. Horcajada, and S. Grau. Azithromycin in the treatment of COVID-19: A review. *Expert Review of Anti-Infective Therapy* 19(2): 147-163 (2021).
11. B. Gonzalez-Zorn. Antibiotic use in the COVID-19

crisis in Spain. *Clinical Microbiology and Infection* 27(4): 646-647 (2020).
12. B.J. Langford, M. So, S. Raybardhan, V. Leung, J.P.R. Soucy, D. Westwood, N. Daneman, and D.R. MacFadden. Antibiotic prescribing in patients with COVID-19: rapid review and meta-analysis. *Clinical Microbiology and Infection* 27(4): 520-531 (2021).
13. M.H. Hussein, E.A. Toraih, A.S. Attia, N. Burley, A.D. Zhang, J. Roos, A. Houghton, N. Aniemeka, M. Omar, M. Aboueisha, M.A. Shama, J. Duchesne, and E. Kandi. Asthma in COVID-19 patients: An extra chain fitting around the neck. *Respiratory Medicine* 175: 106205 (2020).
14. R. Irizarry, D. Sukato, R. Kollmar, S. Schild, J. Silverman, K. Sundaram, S. Stephenson, and M. Stewart. Seizures induce obstructive apnea in DBA/2J audiogenic seizure-prone mice: Lifesaving impact of tracheal implants. *Epilepsia* 61(2): 13-16 (2020).
15. A.D.B. Estrada, J.C. Parra, E.F. Carracedo, A.M. Miguez, A.R. Martínez, E.M. Rubio, M.R. Rivas, P. Agudo, F.A. Fernandez, V.E. Perez, M.L.T. Martinez, A.C. Vieitez, P.M.P. Fontan, M. Bustamante, S.J. Freire, I.O. Bermudez, A. Artero, J.O. Sierra, M.A. Manrique, H.F.J.C. Sanchez, V.C. Vento, G.M. Garcia, P.C. Morais, J.M.C. Rojo, and J.M.N. Cortes. Inadequate use of antibiotics in the covid-19 era: effectiveness of antibiotic therapy. *BMC Infectious Diseases* 21: 1144 (2021).
16. F.D.S.D. Fiol, C.D.C Bergamaschi, I.P.D. Andrade Jr, L.C. Lopes, M.T. Silva, and S. Barberato-Filho. Consumption trends of antibiotics in Brazil during the COVID-19 pandemic. *Frontiers in Pharmacology* 13: 844818 (2022).
17. H. Akhtar, S. Akhtar, F.U. Rahman, M. Afridi, S. Khalid, S. Ali, N. Akhtar, Y.S. Khader, H. Ahmad, and M.M. Khan. An overview of the treatment options used for the management of COVID-19 in Pakistan: Retrospective observational study. *JMIR Public Health and Surveillance* 7(5): e28594 (2021).
18. A. Mansoor, M.T. Khan, A. Hussain, E. Mansoor, A. Gul, and A. Saleem. Comparison of different treatment strategies combating COVID-19 in Pakistan. *Pakistan Armed Forces Medical Journal* 72(5): 1752-1756 (2022).
19. F. Saeed, M. Zubair, M. Jawad, F. Ullah, M.N. Uddin, U. Siddique, A. Wahab, and A. Rizwan. Epidemiological, clinical characteristics and possible treatment of coronavirus disease (Covid-19) during early situation in population of district Karak, Khyber Pakhtunkhwa, Pakistan. *Pak-Euro Journal of Medical and Life Sciences* 4(4): 337-346 (2021).
20. M.Z. Alvi, M. Sattar, F.A. Cheema, U.A. Awan, M.N. Aftab, Z.A. Shah, and M.S. Afzal. COVID-19 and emergence of antimicrobial resistance: a most neglected aspect of health emergency in Pakistan. *Diabetes & Metabolic Syndrome* 15(4): 102179 (2021).
21. Z.U. Mustafa, M.S. Saleem, M.N. Ikram, M. Salman, S.A. Butt, S. Khan, B. Godman, and R.A. Seaton. Co-infections and antimicrobial use among hospitalized COVID-19 patients in Punjab, Pakistan: findings from a multicenter, point prevalence survey. *Pathogens and Global Health* 116(7): 421-427 (2022).
22. M. Farooqui, Z. Iqbal, A. Sadiq, A. Raziq, M.S. Alshammari, Q. Iqbal, S. Haider, and F. Saleem. Hospital pharmacists' viewpoint on quality use of antibiotics and resistance: A qualitative exploration from a tertiary care hospital of Quetta city, Pakistan. *Antibiotics* 12(8): 1343 (2023).
23. B. Gul, M. Sana, A. Saleem, Z.U. Mustafa, M. Salman, Y.H. Khan, T.H. Mallhi, T.M. Sono, J.C. Meyer, and B.B. Godman. Antimicrobial dispensing practices during COVID-19 and the implications for Pakistan. *Antibiotics* 12(6): 1018 (2023).
24. Z.U. Haq, M. Shahzad, M.I. Khattak, S. Fazid, N. Ullah, A. Sherin, N.U. Haq, A. Azhar, U. farooq, N.M. Darwesh, M. Asim, M.A. Gohar, A. Ashraf, S.I. Khattak, S. Ashraf, S. Akbar, M. Fawad, M.I. Khan, A. Amanullah, M. Siddiq, and A.H. Aamir. Clinical characteristics, mortality and associated risk factors in COVID-19 patients reported in ten major hospitals of Khyber Pakhtunkhwa, Pakistan. *Journal of Ayub Medical College Abbottabad* 32(Suppl. 1): 633-639 (2020).
25. G. Aksel, M.M. Islam, A. Algın, S.E. Eroglu, G.B. Yaşar, E. Ademoglu, and U.C. Dolek. Early predictors of mortality for moderate to severely ill patients with Covid-19. *The American Journal of Emergency Medicine* 45: 290-296 (2021).
26. M.A. Qureshi, K.U Toori, and R.M. Ahmed. Predictors of Mortality in COVID-19 patients: An observational study. *Pakistan Journal of Medical Sciences* 39(1): 241-247 (2023).
27. T.H. Jeong, C. Pak, M. Ock, S.H. Lee, J.S. Son, and Y.j. Jeon. Real asymptomatic SARS-CoV-2 infection might be rare: importance of careful interviews and follow-up. *Journal of Korean Medical Science* 35(37): e333 (2020).

Proceedings of the Pakistan Academy of Sciences: A Physical and Computational Sciences 61(4): 381-390 (2024)

ISSN (Print): 2518-4245; ISSN (Online): 2518-4253
http://doi.org/10.53560/PPASA(61-4)673

Pakistan Academy of Sciences

Research Article

Geostatistical Model Development and Assessment of Tidal Stream Energy Resources: A Case Study of Indus Delta, Pakistan

Mirza Salman Baig[1*], Ambreen Insaf[1], Saba Javaid[2], and Zaheer Uddin[3]

[1]Department of Applied Physics, University of Karachi, Karachi, Pakistan
[2]Department of Physics, NED University of Engineering and Technology, Karachi, Pakistan
[3]Department of Physics, University of Karachi, Karachi, Pakistan

Abstract: In this paper, an approach is applied by using the Geographical Information System for the development of geostatistical models to assess available tidal stream energy resources of the Indus Delta Creek system. The mean spring tidal current of twelve different locations in the Indus Delta Creek system (Pakistan) is utilized to develop geostatistical models for the prediction of tidal currents at different locations where no data was available. Models are validated and an investigation of prediction error is carried out to select the best model. For the prediction of tidal stream data, various models are collated namely (i) Circular (ii) K-Bessel (iii) Stable, and (iv) Exponential. These models show the range of mean spring ebb current between 1.9 m/s and 2.12 m/s and the range of mean spring flood current between 1.4 m/s and 1.65 m/s. The stable model for mean spring flood current and circular model for mean spring ebb current agreed with the observed ones. Furthermore, the tidal kinetic power density model and bathymetry model are also developed for the selection of potential sites within the study area. Based on results achieved from geostatistical and bathymetry models; deployment of the suitable turbine at the study area is proposed and generation of 2754.7 MW electric power is estimated.

Keywords: Tidal Energy Resources, Tidal Current Turbines, Tidal Stream Energy, Power Density, Tidal Current Meter, Indus Delta, Karachi Coast.

1. INTRODUCTION

The economy of Pakistan has been shrinking since the start of the COVID-19 pandemic in 2019 and the impact of this crisis has seriously distressed the life of common people. Moreover, high inflation, fewer exports, high international market prices, and the worst energy crises have also encumbered the economy. These days, Pakistan is encountering extreme energy crises and the energy demand and supply gap is growing continuously [1]. Additionally, the rising energy demand has increased its cost and the situation has become worse after "the Russia-Ukraine conflict which has so far driven the prices for energy and fuel even higher and caused the price of oil to jump to a high level in almost 14 years, while wholesale gas prices have more than doubled" [2]. During 2020, peak electricity demand reached 25 GW besides 22 GW of electricity production [3] and this shortfall of electricity in the country has not only caused a worse situation in the agricultural industry but has also shut down many industrial plants [4]. Consequently, an increase in the unit price of electricity occurred. The Government of Pakistan is developing policies to reduce fossil fuel dependency by adopting Renewable Energy (RE) sources [5]. Presently, wind and solar energy farms have been deployed in the country [6] but besides having a nearly 1000 km long coastline, the Tidal Stream Energy (TSE) exploration has been neglected so far. TSE is a clean, most predictable, low visual impact, and easily available solution for the existing energy scenario in Pakistan. The Indus Delta region of Pakistan consists of an intricate network of creeks that could be exploited for the deployment of Marine Current Turbines (MCT). However, so far, the Indus Delta creek system has been neglected for the exploration

Received: December 2023; Revised: November 2024; Accepted: December 2024
* Corresponding Author: Mirza Salman Baig <mirza_salmanbaig@hotmail.com>

of TSE resources. Therefore, a comprehensive study is required to assess the potential of TSE resources. Marine Current Turbines (MCTs) are intended for installation in natural streams, tidal estuaries, and other flowing water facilities; optimized for a specific velocity [7-9]. To increase power production from MCTs, a multiunit array arrangement can be deployed like wind turbine farms [9-11]. Many scholars have worked on array arrangements for TSE extraction [12-15]. The array arrangement using MCT depends on the number of MCTs, dimension of MCT, efficiency of MCT, and the Tidal Kinetic Power Density (TKPD) within the Area of Interest (AOI). The Kinetic Energy (KE) of a tidal stream is calculated by [16]:

$$KE = (1/2)\ \rho A V^3 \quad (1)$$

Where ρ is the density of seawater kg/m^3, A is the cross-sectional area in m, and V is the magnitude of the velocity of seawater in m/s. TKPD is then derived from [17, 18]:

$$P_{KE} = 0.212\ \rho V^3 \quad (2)$$

It represents the average KE per unit area of MCT aperture. Whereas, more practically, all of this power cannot be harnessed because of Betz's law and the mechanical losses in MCT [17]. Hence, the effective TKPD that MCT can extract is [16]:

$$P_{e.ke} = 0.212\ C_P\ \rho V^3 \quad (3)$$

Here C_P is the power coefficient and limits the MCT's efficiency. The requirements for the assessment of TSE resources with multiunit array arrangement have been narrated by the researchers [12-15, 19]:

- Selection of suitable sites for MCT depending on water current and suitable depth
- Identification of appropriate type of MCT and its dimensions
- Opting best MCT arrangement for the region
- Investigation of the effect of MCT on the tidal downstream

Aforesaid in view, this study aims to investigate and estimate the TSE resources of the creek region of the Indus Delta, which are so far unexploited and neglected. To assess TSE resources for the study area, tidal stream data was acquired and evaluated for the first time. Since the Area of Interest (AOI) is comprised of a large area and due to the limitation of available tidal data, an approach using a geostatistical model is applied to predict the tidal data at unobserved locations. Moreover, the TKPD model is developed for the first time for the entire Indus Delta region.

2. STUDY AREA AND METHODOLOGY

Figure 1 represents the methodology of the research study carried out for the assessment of TSE resources in the creek region of the Indus Delta, Pakistan [20]. Indus Delta region is found

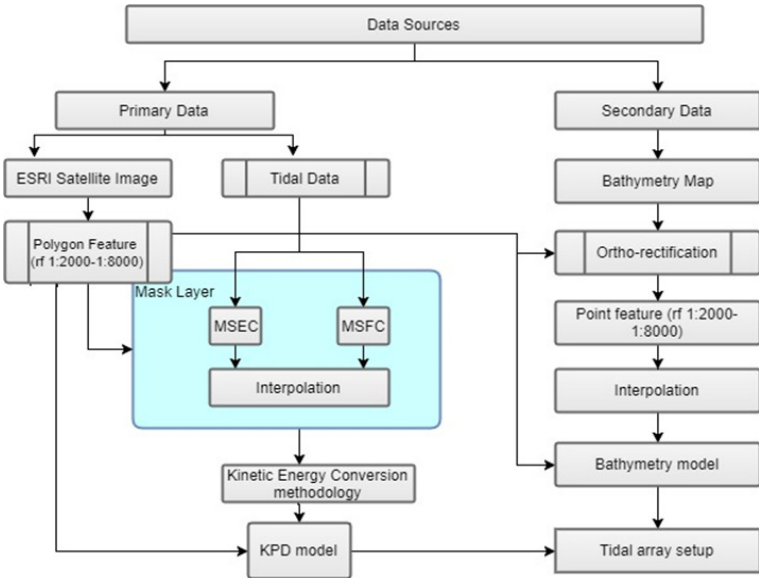

Fig. 1. Methodological framework.

to be the most potential site for TSE resources in Pakistan which is around 190 km long, including 17 primary and a large number of secondary creeks extending from Korangi Creek near Karachi to Sir Creek near the Pakistan-India border with an area of 30,000 km^2 [21, 22] as shown in Figure 2. For the development of the TKPD model, 12 sites are considered (see Figure 3) and assigned station IDs. Tidal observations were available only for these sites; therefore these are selected for the TKPD model.

This methodology consists of the acquisition and processing of data, different techniques for assessment of models, model selection, tidal data estimation at an unobserved location, TKPD model development, turbine selection, and power generation from selected turbines. Tidal stream data was acquired from the Hydrography Department, Pakistan, using a Tidal Current Meter (TCM). Tidal data includes the Mean Spring Ebb Current (MSEC) and Mean Spring Flood Current (MSFC) of 12 sites for the duration of 9 years (2005 to 2014) as shown in Table 1. Satellite and bathymetry data acquisition and processing were carried out as mentioned by Insaf *et al.* [23].

For the GIS model setup; the AOI Land digitization layer, tidal stream data, and socioeconomic layer were transported to the geodatabase for processing in the GIS environment. The prediction model of TS data was created by using ArcGIS (v.10.2) and Geostatistical Analyst extension. Geostatistical techniques can interpolate

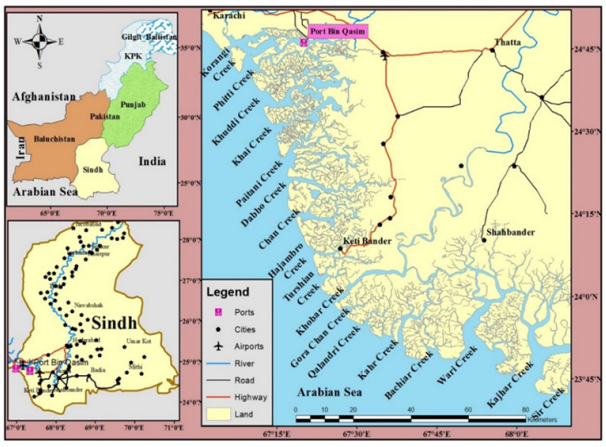

Fig. 2. Map of the study area.

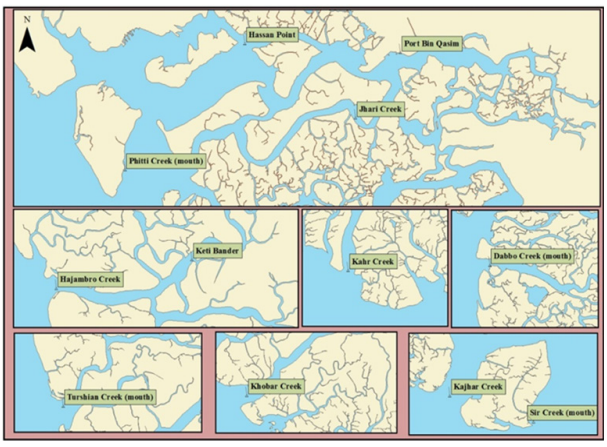

Fig. 3. Locations considered for study area.

Table 1. Acquired tidal current data of twelve sites with name, geographical location, and ID (TCS = Tidal Current Site).

Station IDs	Longitude (E)	Latitude (N)	Site names	Mean spring current (m/s)	
				Flood	Ebb
TCS1	67.352	24.775	Port bin Qasim	1.543	2.058
TCS2	67.142	24.698	Phitti Creek	1.4	1.9
TCS3	67.233	24.783	Hassan Point	1.45	2
TCS4	67.317	24.733	Jhari Creek	1.543	2.058
TCS5	67.367	24.133	Hajambro Creek	1.65	2.1
TCS6	67.45	24.15	Keti Bander	1.543	2.058
TCS7	67.301	24.353	Dabbo Creek	1.543	2.058
TCS8	67.389	24.057	Turshian Creek	1.543	2.058
TCS9	67.436	23.993	Khobar Creek	1.543	2.058
TCS10	68.04	23.754	Kajhar Creek	1.5	1.9
TCS11	68.168	23.715	Sir Creek	1.65	2.12
TCS12	67.635	23.856	Kahr Creek	1.45	2.058

continuous surfaces by taking sample points from various locations, showing an indication of better predictions. Geostatistical methods; Kriging Ordinary (KO), Kriging Simple (KS), and Kriging Universal were assessed. These models with governing equations are explicated by [24]. Results obtained from the KO method were more appropriate than the other two interpolators.

3. RESULTS AND DISCUSSION

Four different semi-variogram models; stable (STB), K-Bessel (KB), circular (CIR), and exponential (EXP) were tested for each parameter of the dataset, and model results were assessed for the best-estimated values. Estimation performance was evaluated by cross-validation method.

For the model accuracy, a cross-validation method and error estimation equations were applied [23]. The cross-validation method determines the best prediction model by evaluating that Mean Standardized Error (MSE) and Mean Prediction Error (MPE) must be minimal (approaching to zero), the Root-Mean-Square Prediction Error (RMSPE) and Average Standard Prediction Error (ASPE) should also be as minimum as possible (suitable for model comparisons), and the Root-Mean Square Standardized Prediction Error (RMSSPE) near to 1.

Figure 4 represents the outcomes of four different models STB, KB, CIR, and EXP showing an overall range of MSEC from 1.9 m/s to 2.12 m/s. It indicates that MSEC rises gradually from the creek mouth towards land and it also rises in a southeast direction (from Karachi towards Sir Creek). A comparison between the observed and estimated MSEC values are shown in Figure 5 for four models. According to this comparison, the STB model generates the lowest MSEC at TC2 (1.988 m/s) and the highest MSEC at TC9 (2.071 m/s). The CIR model yields the lowest MSEC at TC10 (1.908 m/s) and the highest MSEC at TC7 (2.075 m/s). EXP model produces the lowest MSEC at TC2 (1.980 m/s) and the highest MSEC at TC7 (2.072 m/s). KB model estimates the lowest MSEC at TC2 (1.996 m/s) and the highest MSEC at TC7 (2.074 m/s).

Analysis of Prediction Error Statistics (PES) is performed for the acceptability and the selection of a best-fitted model for MSEC. For the model validation, all PES parameters (ME, RMSE, MSE, RMSSE, and ASE) are summarized together and presented in Figure 6 for all models. Considering the conditions of validation, results obtained from the CIR model are found most appropriate and best fitted.

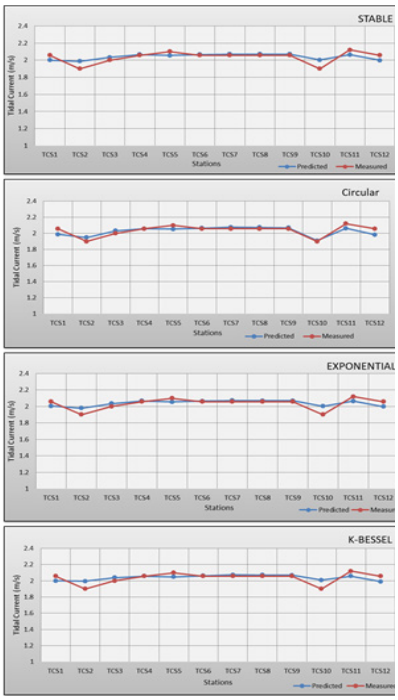

Fig. 5. Observed and predicted MSEC using different models.

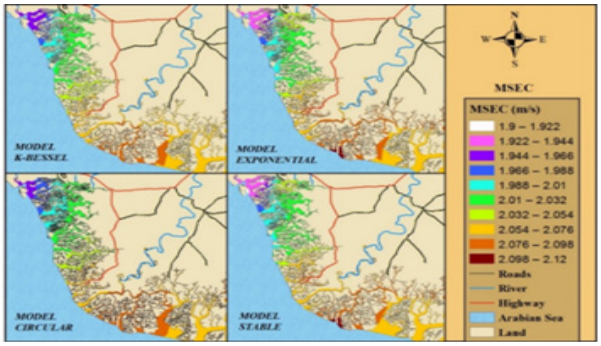

Fig. 4. MSEC models.

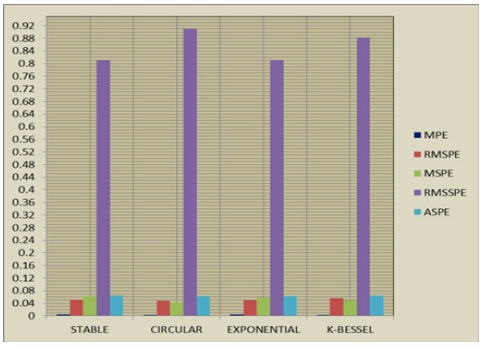

Fig. 6. Analysis for error estimation for MSEC.

Figure 7 represents results obtained from the same four models STB, KB, CIR, and EXP representing the overall range of MSFC from 1.4 m/s to 1.65 m/s. Figure 7 indicates that MSFC rises gradually from the creek mouth towards land and it also rises in a southeast direction (from Karachi towards Sir Creek). Assessment of the observed and estimated MSFC values is shown in Figure 8 for four models. According to the assessment, the STB model generates the lowest MSFC at TC2 (1.447 m/s) and the highest MSFC at TC11 (1.587 m/s). The CIR model yields the lowest MSFC at station TC1 (1.461 m/s) and the highest MSFC at TC7 (1.587 m/s). EXP model produces the lowest MSFC at TC1 (1.471 m/s) and the highest MSFC at TC7 (1.577 m/s). KB model estimates the lowest MSFC at TC1 (1.464 m/s) and the highest MSFC at TC7 (1.584 m/s).

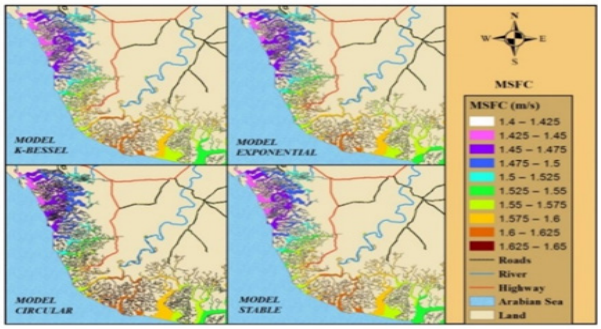

Fig. 7. MSFC models.

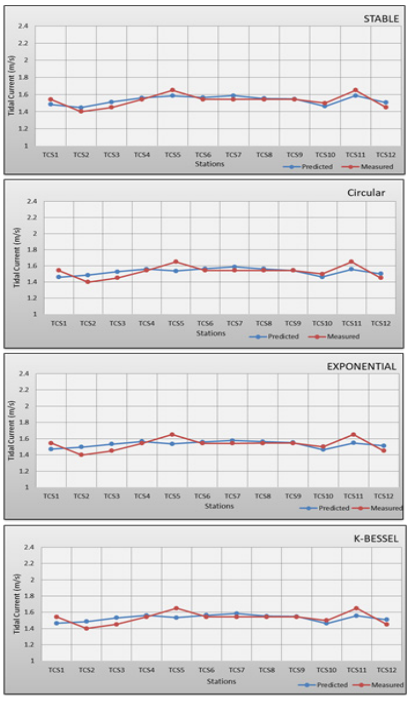

Fig. 8. Observed and predicted MSFC using different models.

Analysis of PES is performed for the acceptability and the selection of the best-fitted model for MSFC. For the model validation, all PES parameters (ME, RMSE, MSE, RMSSE, and ASE) are summarized together and presented in Figure 9 for all models. The comparative analysis shows that results obtained from the STB model are found most appropriate and best fitted.

The KO predictor is employed for the estimation of MSEC and MSFC at unobserved sites within AOI. For the prediction of data, seven more potential sites were considered where there was unavailability of data (see Figure 10). The best-fitted model is chosen (discussed and validated in the previous section) for the estimation of MSEC and MSFC. Table 2 represents estimated values of MSEC and MSFC at unobserved sites with their geographical locations.

Different layers were integrated into ArcGIS for the development of the TKPD model. These layers include MSEC and MSFC layers generated through geostatistical analysis, socioeconomic

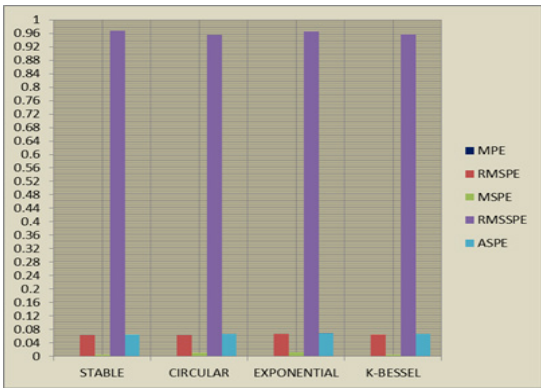

Fig. 9. Analysis of error estimation for MSFC.

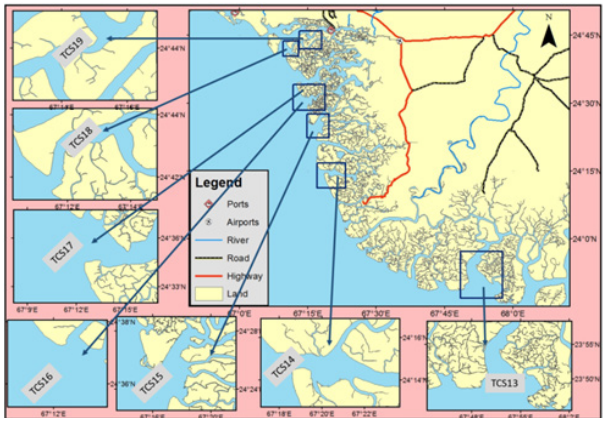

Fig. 10. Map of unobserved sites.

Table 2. Predicted MSEC and MSFC at unobserved sites.

Site (Predicted)	ID	Longitude (E)	Latitude (N)	MSFC (m/s)	MSEC (m/s)
Wari Creek	TCS13	67.85	23.9	1.588	2.078
Chan Creek	TCS14	67.3	24.24	1.51	2.035
Paitani Creek	TCS15	67.24	24.38	1.461	2.009
Khuddi 1 Creek	TCS16	67.2	24.59	1.438	1.984
Khuddi 2 Creek	TCS17	67.2	24.6	1.437	1.982
Chhan Waddo Creek	TCS18	67.2	24.7	1.446	1.969
Rakchal Creek	TCS19	67.24	24.73	1.464	1.978

layer, and Equation (2). Figure 11 represents the final TKPD model for MSEC and MSFC masked over the water surface which shows that the region south of Indus Delta has substantial TKPD. Furthermore, TKPD decreases from the tail of creeks towards the mouth near the Arabian Sea. The remaining AOI is classified as having moderate TKPD.

TKPD for MSEC ranges from 1.1 to 1.6 MW/m^2 and for MSFC it ranges from 0.6 to 0.98 MW/m^2. This model is lucrative in exploring sites with prominent TKPD. Table 3 incorporates TKPD values along with the geographical locations of observed and unobserved sites.

The bathymetry model is a very essential part of tidal turbine deployment. Thus, a complete model for the best visualization of bathymetry within the study area is developed and found useful for the installation of proposed tidal turbines at a region of interest. This model shows adequate water depths at proposed sites for deployment of the tidal array structure shown in Figure 12. Regions of interest are found with depths greater than 9m. Results also show that water depths increase rapidly when moving away from creek structure that is, the mouth of creeks has larger depths than the tail of creeks.

The next step in the assessment of TSE resources in the creek region of the Indus Delta is the site selection. Criteria for site selection for TSE evaluation include the following considerations:

i. There must be significant tidal stream current which can be observed from MSEC and MSFC models.
ii. Adequate bathymetry and dimensions of the creek for deployment of MCT are required (sites with bathymetry greater than 9m are considered adequate for installation of MCT due to the size of the rotor and rated velocity of proposed MCT).
iii. The proposed site must not be a major shipping port.

In view, thirteen sites are proposed for TSE assessment by considering the above criteria. Table 4 shows the geographical locations of the proposed sites along with the dimensions of the intended creeks and their identification numbers.

To deploy an appropriate MCT that could best fit in proposed sites within AOI for power extraction; an effort was made to collect all essential information about the status of modern MCT

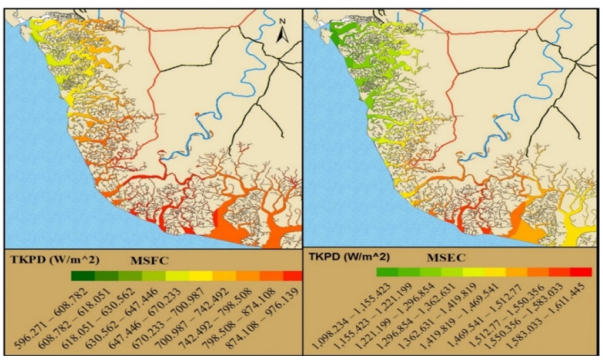

Fig. 11. TKPD model for MSEC and MSFC.

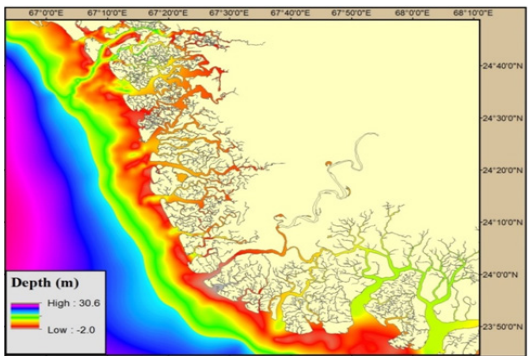

Fig. 12. Bathymetry of study area.

Table 3. TKPD (W/m^2) at observed and unobserved sites.

ID	Latitude N	Longitude E	TKPD (W/m^2)	
			(MSEC)	(MSFC)
TCS1	24.78	67.35	1420.06	798.75
TCS2	24.698	67.14	1098.23	596.27
TCS3	24.78	67.23	1260.34	662.47
TCS4	24.73	67.32	1419.79	798.28
TCS5	24.13	67.37	1581.18	976.14
TCS6	24.15	67.45	1419.79	798.28
TCS7	24.35	67.30	1419.79	798.28
TCS8	24.06	67.389	1420.09	798.80
TCS9	23.99	67.44	1420.09	798.80
TCS10	23.75	68.04	1176.68	733.39
TCS11	23.72	68.17	1611.44	976.14
TCS12	23.86	67.64	1334.21	662.47
TCS13	23.9	67.85	1521.39	873.23
TCS14	24.24	67.3	1345.19	752.8
TCS15	24.38	67.24	1251.23	680.58
TCS16	24.59	67.2	1200.72	648.39
TCS17	24.6	67.2	1198.1	647.32
TCS18	24.7	67.2	1176.65	659.06
TCS19	24.73	67.24	1218.58	684.3

Table 4. Locations where the extraction of TKE is projected.

Site ID	Latitude (N)	Longitude (E)	Length (Km)	Breadth (Km)
TCS4	24.71	67.24	4	0.23
TCS5	24.133	67.367	3	0.3
TCS6	24.15	67.45	1	0.2
TCS8	24.057	67.389	1	1.2
TCS10	23.754	68.04	4	2
TCS12	23.8556	67.635	3	2
TCS13	23.9	67.85	3	1.21
TCS14	24.24	67.3	1.9	0.148
TCS15	24.38	67.24	2	1
TCS16	24.59	67.2	5	1
TCS17	24.6	67.2	2	0.7
TCS18	24.7	67.2	4	0.58
TCS19	24.73	67.24	2	0.25

technology and their technical specifications. Some MCTs are found appropriate and compatible with site characteristics (rated velocity, bathymetry, etc.) These suitable MCTs with turbine specifications are shown in Table 5. Accordingly, a tidal array arrangement is planned with the following characteristics, as explained by [25]:

i. The lateral gap between devices was maintained at two and a half times the rotor diameter (2.5d).

ii. A row spacing of 10d was chosen. This separation is necessary to prevent adverse impacts on the downstream device's performance due to flow disturbances generated by the upstream device.

The number of MCTs needed to be installed in tidal array arrangement at proposed locations and the calculated Mean Spring Power (MSP) is determined by considering the turbine's effectiveness, seawater density, and the values of MSEC and MSFC obtained from the model findings (refer to Table 2). MSPs generated from proposed MCTs are shown in Table 6. The evaluated Mean Spring Power (MSP) produced by Verdant Power's KHPS-5 turbine is identified as the highest, reaching 2754.7 MW when compared with MSP generated from T-1 (1380 MW) and Hydro-Gen-20 turbines (2190 MW). To conclude, Verdant Power's KHPS-5 turbine is ultimately advised for deployment at the proposed locations. The Roosevelt Island Tidal Energy (RITE) Project, developed by Verdant Power in New York City's East River, was licensed for a capacity of up to 1 MW. This capacity was to be achieved through the staged installation of up to 30 turbines mounted on 10 TriFrames [26]. The MeyGen Tidal Energy Project in Scotland is a prominent tidal energy initiative with significant power generation capabilities. The project has been developed in phases, with Phase 1A involving the installation of four 1.5 MW turbines, totalling 6 MW of installed capacity. The long-term goal is to expand the project to a capacity of up to 398 MW [27].

The Indus Delta's estimated power generation capacity of 2754.7 MW far surpasses the current operational capacities of MeyGen and RITE. This is significantly higher due to the larger scale of tidal stream energy resources in the Indus Delta and the favorable tidal conditions in the region. This highlights its potential as a major tidal energy resource. While MeyGen leads in technology deployment and future scalability, and RITE demonstrates urban feasibility, the Indus Delta Creek system offers a unique opportunity for large-scale renewable energy development.

Table 5. Marine current turbines (MCTs) suggested for extraction of TKE at designated locations.

Manufacturer	MCT type	Rated velocity (m/s)	Rotor diameter (m)	Efficiency (%)	Rated power (MW)
Verdant Power	KHPS-5	2	5	44	0.035
Tocardo	T-1	2	6.3	35	0.042
Hydro-Gen	Hydro-Gen-20	2	5	35	0.020

Table 6. Projected power output from KHPS-5 marine current turbine (MCT).

ID	No. of rows	MCTs in a row	Total turbines in array	Assessed MSP (MW) using KHPS-5
TCS4	80	18	1432	68.7
TCS5	60	24	1410	77.6
TCS6	20	16	310	17.4
TCS8	20	96	1910	106.3
TCS10	80	160	12760	709.9
TCS12	60	160	9570	567
TCS13	60	97	5778	331.7
TCS14	38	12	431	22.63
TCS15	40	80	3180	157.9
TCS16	100	80	7950	379.2
TCS17	40	56	2220	105.6
TCS18	80	46	3672	173.1
TCS19	40	20	780	37.5
Total estimated output power (MW)				2754.7

4. CONCLUSIONS

This study is carried out for the exploration and estimation of TSE harnessing techniques by developing geostatistical models using GIS. AOI has so far not explored for utilization of TSE. Therefore, this research study is an initial resource estimation of TSE resources. KO method is utilized in the development of MSEC and MSFC models. Tidal stream current and satellite data are integrated with GIS to develop the TKPD model. Developed four different models show the range of MSEC varies between 1.9 to 2.12 m/s and the range of MSFC varies between 1.4 to 1.65 m/s. The geostatistical Analysis technique is utilized to analyze different interpolation methods for the prediction of MSEC and MSFC at unobserved locations. Four different models (STB, KB, CIR, and EXP) are assessed for tidal stream data. These models are evaluated and cross-validated to choose the best-fitted model for predictions of MSEC and MSFC at unobserved locations. After the evaluation of cross-validation results, a stable model is selected for MSFC, and a circular model is selected for MSEC.

The bathymetry model was developed in an ArcGIS environment to visualize and identify locations with adequate water depth for the deployment of MCT. Thirteen sites are proposed for deployment of MCT. Assessed MSP generated from Verdant Power (KHPS-5) is found highest (i.e. 2754.7 MW) when compared with MSP generated from T-1 and Hydro-Gen-20 turbines (see Table 5 and Table 6), therefore Verdant Power (KHPS-5) is finally recommended for installation at suggested sites.

5. ACKNOWLEDGEMENT

The authors would like to acknowledge Hydrography Department, Pakistan, for providing valuable support for this research study.

6. CONFLICT OF INTEREST

The authors do not have any conflict of interest.

7. REFERENCES

1. A. Rehman, H. Ma, M. Radulescu, C.I. Sinisi, and Z. Yousaf. Energy crisis in Pakistan and economic progress: decoupling the impact of coal energy consumption in power and Brick Kilns. *Mathematics* 9(17): 2083 (2021).
2. L. Jones. Five ways the Ukraine war could push up prices. (2022). https://www.bbc.com/news/business-60509453.
3. NEPRA. State of Industry Report 2020. *National Electric Power Regulatory Authority (NEPRA), Islamabad, Pakistan* (2020). https://nepra.org.pk/publications/State%20of%20Industry%20Reports/State%20of%20Industry%20Report%202020.pdf.
4. M.O. Finance. Pakistan economic survey (2022) https://www.finance.gov.pk/survey_1213.html
5. J. Tao, M. Waqas, M. Ali, M. Umair, W. Gan, and H. Haider. Pakistan's electrical energy crises, a way forward towards 50% of sustain clean and green electricity generation. *Energy Strategy Reviews* 40: 100813 (2022).
6. M. Kamran. Current status and future success of renewable energy in Pakistan. *Renewable and Sustainable Energy Reviews* 82(1): 609-617 (2018).
7. T.A. Adcock, S. Draper, R.H.J. Willden, and C.R. Vogel. The fluid mechanics of tidal stream energy conversion. *Annual Review of Fluid Mechanics* 53: 287-310 (2021).
8. M. Güney and K. Kaygusuz. Hydrokinetic energy conversion systems: A technology status review. *Renewable and Sustainable Energy Reviews* 14(9): 2996-3004 (2010).
9. L. Lago, F. Ponta, and L. Chen. Advances and trends in hydrokinetic turbine systems. *Energy for Sustainable Development* 14(4): 287-296 (2010).
10. M. Khan, M. Iqbal, and J. Quaicoe. River current energy conversion systems: Progress, prospects and challenges. *Renewable and Sustainable Energy Reviews* 12(8): 2177-2193 (2008).
11. M.I. Yuce and A. Muratoglu. Hydrokinetic energy conversion systems: A technology status review. *Renewable and Sustainable Energy Reviews* 43: 72-82 (2015).
12. W. Pangastuti. Study of tidal use in Seribu Islands Area. B.Sc. Final Year Project. *Bandung: Bandung Institute of Technology, Indonesia* (2005).
13. A. Bahaj and L. Myers. Analytical estimates of the energy yield potential from the Alderney Race (Channel Islands) using marine current energy converters. *Renewable Energy* 29(12): 1931-1945 (2004).
14. L. Blunden and A. Bahaj. Initial evaluation of tidal stream energy resources at Portland Bill, UK. *Renewable Energy* 31(2): 121-132 (2006).
15. N.S. Aziz. Tidal energy resources assessment in Indonesia: A case study in Alas Strait. Master Thesis.

Department of Coastal and Marine Engineering and Management, University of Southampton, England (2009).
16. R. Carballo, G. Iglesias, and A. Castro. Numerical model evaluation of tidal stream energy resources in the Ría de Muros (NW Spain). *Renewable Energy* 34(6): 1517-1524 (2009).
17. A. Rashid. Status and potentials of tidal in-stream energy resources in the southern coasts of Iran: A case study. *Renewable and Sustainable Energy Reviews* 16(9): 6668-6677 (2012).
18. J. Twidell and A.D. Weir (Eds.). Renewable energy resources. *Taylor & Francis* (2006).
19. L. Blunden and A. Bahaj. Tidal energy resource assessment for tidal stream generators. *Proceedings of the Institution of Mechanical Engineers, Part A: Journal of Power and Energy* 221(2): 137-146 (2007).
20. M.S. Baig, Z. Uddin, and A. Insaf. GIS-linked tidal range energy resource assessment. *Arabian Journal of Geosciences* 14(6): 1-16 (2021).
21. G.A. Mahar. Geomorphic Degradation of Indus Delta and Its Demographic Impact. Ph.D. Thesis. *University of Karachi, Karachi, Pakistan* (2010).
22. A. Abbasi. Restoration of Sindh's primary rights over River Indus. 18th convention of SANA. July 4-7, 2002. *Cherry Hill, New Jersey* pp. 4-7 (2002).
23. A. Insaf, M.S. Baig, and Z. Uddin. Tidal range energy resource assessment and power generation at Hawke's Bay and Ghizri. *Arabian Journal of Geosciences* 15(10): 1-15 (2022).
24. M.S. Baig. Estimation of Tidal Energy Utilizing Different Harnessing Techniques through Geographical Information System within Creek Area of Indus Delta, Sindh Province, Pakistan. Ph.D. Thesis. *Department of Applied Physics, University of Karachi, Karachi, Pakistan* (2019).
25. C. Legrand. Assessment of Tidal Energy Resource: Marine Renewable Energy Guides. *European Marine Energy Centre, British Library Cataloguing in Publication Data* (2009). https://www.emec.org.uk/assessment-of-tidal-energy-resource/.
26. V. Power. Roosevelt Island Tidal Energy Environmental Assessment Project, Final Report. *New York State Energy Research and Development Authority* (2020).
27. L.T.D. Meygen. Meygen tidal energy project phase 1: Environmental Statement. Technical Report. *MeyGen* (2012). https://marine.gov.scot/datafiles/lot/Meygen/Environmental_statement/Complete%20ES.pdf.

Proceedings of the Pakistan Academy of Sciences: A Physical and Computational Sciences 61(4): 391-399 (2024)

ISSN (Print): 2518-4245; ISSN (Online): 2518-4253
http://doi.org/10.53560/PPASA(61-4)878

Pakistan Academy of Sciences

Research Article

Investigating the Effects of Horizontal Transition with Student-Preferred Learning Materials in a Virtual Biology Laboratory

Asad Ullah Khan, Aftab Alam, Shah Khalid*, Sehat Ullah, and Fakhr ud Din

Department of Computer Science and IT, University of Malakand, Chakdara, Pakistan

Abstract: Adaptive Virtual Learning Environments (VLEs) present customized teaching materials to individual students which help them to achieve their learning goals and serve quite a vital role in virtual learning environments. In this paper, we present a new student-centered learning approach in a three-dimensional (3D) virtual biology laboratory (VBIOLAB). The approach is based on the concept of horizontal transition with student preference (HTWSP) implemented with the help of VBIOLAB. The HTWSP is based on the concept of allowing students to choose their preferred learning styles according to their needs and pace instead of automatically adapted aids. HTWSP allows students to stay in a certain module and attain more information about that learning module through various aids of their choice. To go to the next learning module there is a mechanism of vertical transition which allows a student to make quick progress by skipping the details about a certain module. Intermediate-level students participated in experiments that compared the proposed system with an adaptive virtual laboratory. Experimental results indicated that 75% of students improved their examination scores through the use of VBIOLAB. Data from the system usability scale (SUS) and the subjective rating supported greater participation, motivation, and effectiveness in learning using VBIOLAB. The experimental results reveal that this approach is effective and vital to utilize to enhance students' learning in 3D-VLEs.

Keywords: Virtual Reality, Virtual Learning Environment, Virtual Biology Laboratory, Learning Approach, Student Learning Styles, Horizontal Transition, Vertical Transition.

1. INTRODUCTION

Virtual Reality (VR) technologies allow users to immerse themselves in the interactive simulation system through visual, auditory, and tactile feedback. VR uses 3D graphics and sensors to generate realistic virtual environments and get objects that are processed and controlled by computers [1]. The multi-sensory interactive nature of VR allows it to be widely used in various fields, i.e. Artificial Intelligence and machine learning, education and E-Learning, healthcare and medicine, software development, edutainment, robotics, and autonomous systems and training. Numerous concepts are taught through VR applications [2]. For gaining scientific knowledge, laboratories are imperative in every field of science. Laboratories provide opportunities for building skills and learning experimental work. Physical labs need many resources i.e. place, apparatuses, and workforce. Virtual labs eliminate all these requirements. Laboratories provide replicas of physical labs and help to increase learning experiences [3]. Virtual laboratories allow students to perform experiments similar to conventional labs and to gain experience in laboratory work. Students are permitted to perform experiments without any fear of making mistakes because they can fix them by revising the experiment and thus their inquisition and commitment to learning is increased [4].

The continued development in computer graphics and virtual reality can provide the opportunity to rapidly expand the use of virtual laboratory applications which ultimately decrease the need for real-world laboratories [5]. Customized

Received: October 2024; Revised: Novemebr 2024; Accepted:December 2024
* Corresponding Author: Shah Khalid <khaliddir@gmail.com>

teaching materials for different students result in enhanced learning which improves students' performance in 3D-VLEs [6]. Adaptive 3D-VLE can alter its materials for different students because their learning strategies vary, which contributes to improving their learning [7]. Changing the contents of 3-Dimensional Virtual Learning Environments is a difficult task because of no clear strategy for specific learners [8].

In anatomy teaching, it is observed that with the traditional approach, students do not get enough opportunities to achieve learning objectives. Theoretical, 2D PowerPoint presentations and other traditional aids are not sufficient for their future learning provisions. 3D-VLEs about anatomy provide innovation and ease of interactivity with bones, muscles, and other organs. Users can manipulate them and it contributes to increasing their performance significantly [5]. Various studies conclude that students, who were taught through 3D animated programs of various body parts, took decent grades in contrast with 2D PowerPoint presentations [9]. Seo *et al.* [10] developed the Anatomy Builder VR application, to examine how a constructivist method can support anatomy education while using VR technology actively and experimentally. Traditional VLEs are not capable of properly administering the diverse requirements of students and this issue can be solved by adaptability. Adaptive 3D-VLEs can alter their materials for different students because their learning strategies vary the adaptivity contributes to improving their learning [7]. Byukusenge *et al.* [11] investigate the effect of virtual laboratories on student performance in learning Biology education. The results show significant improvement in upper secondary students' attitudes and performance in challenging biology topics.

Customized teaching materials for individual students prevent them from amiss steering in the virtual world and provide a means of differentiation between knowledge and merriment [12]. Designing a system in which the adaptivity of the learning material of considering the student's properties is still a challenging job [7]. For teaching anatomy in a 3D VLE, direct manipulation is better than passively viewing a certain structure. The result of the two groups suggests that direct manipulation through a haptic virtual device group achieved higher grades as compared to the passive viewer group [13]. Students learn better when their learning style matches with their teacher's style [7]. According to Cristina *et al.* [14], simulations in virtual laboratories are deemed most effective as preparatory tools rather than replacements for traditional labs.

There are substantial connections between students' achievements and their learning techniques [12]. An and Carr [15] present individual differences as the alternative solution to learning styles and suggest teachers consider the various variables of individual differences, i.e., verbal and visual skills, expertise, self-regulation, etc. The study conducted by Tsirulnikov *et al*. [16] found that immersive virtual reality laboratory simulations using head-mounted displays effectively enhanced undergraduate students' learning outcomes and motivation. Reisoglu *et al.* [17] compared various learning strategies inside a VLE and concluded that learners prefer collaborative learning strategy and exploration-based learning strategy. Other strategies were role-playing; problem-based learning, learning by doing, etc. They asserted that collaborative and exploration-based learning strategies were preferred in learning support environments. The Traditional educational methods of learning are teacher-centered and students have different knowledge levels individually and usually, they are incapable of obtaining the effective usage of the teaching methods to upsurge their knowledge alike. Very little attention is given to resolving the concentration issues that arise during the delivery of learning materials for each student. Gunathilaka *et al.* [18], worked on an approach that they call the Individual learning path personalization approach. The learning materials are changed dynamically according to the knowledge levels of the learner and learning styles in a VLE. They distributed the learning materials in personalized paths and in a student-preferred way. They calculated their preferences in terms of knowledge levels, and dynamic and static learning behavior of the student, and lesson contents are delivered accordingly. It is observed that the learning path personalization according to the knowledge level and the style affects learning positively and their performance increases as compared to the group who did not use this VLE. Alshammari [19] worked on an adaptive approach that incorporates learning style and student performance to produce personalized learning paths as the main adaptive feature. These variables were

identified through questionnaires from students to determine the value and type in the learning style dimension for each student. To represent the perception dimension of learning style in the student model, they assigned the students to one of the defined four stereotypes; students having strong or moderate sensory style, mild sensory style, mild intuitive style, and strong or moderate intuitive style. They tracked the students' performance through quizzes and dynamic student-system interaction which classified the knowledge level into one of four degrees including: unknown, partially learned, learned, and mastered. They experimented with two groups, one with the traditional approach and the other with their proposed approach, and concluded that the adaptive approach was effective. Alam and Ullah [7] presented the idea of horizontal transition for adaptive VLE in which information is presented in the form of figures, graphs, or tables. It provides an opportunity for students to realize the required learning topics by providing additional information about a certain topic and staying more in a learning module, consequently, a weak learner can benefit from this. Also, there is a mechanism of vertical transition which is for good learners to quickly progress by providing the next module with less detail. These transitions are decided by a learning decision function (LDF) that takes a student's score, no. of errors, and time as input and automatically decides the next step of learning for the student. Teaching materials at the next level occur according to the previous performance of the student [6]. The system provides detailed information in customized paths through figures, graphs, or tables. It provides detailed information to weak students and stays in the same learning module. For good students, it shows abstract information in the next module. A good learner may need more information at the next level and may face problems as the adaptive criteria "learning skill" does not handle this situation. There is a need for a proper framework to improve horizontal transition; also there is a need for different learning styles and materials. Most importantly, students should be allowed to make transitions according to their needs and preferred learning styles.

Current approaches are based on automatic adaptation based on performance or by predefined stereotypes. However, these approaches prevent the independence of students from regulating transition and their learning trajectories. Students have problems with automatic adaptations that are not based on their preferences and requirements. In this paper, we developed a new learning approach called Horizontal Transition with Student Preference (HTWSP). The proposed HTWSP presents customized teaching materials to each student as per his/her preference and pace. HTWSP provides an opportunity for students to obtain information following their favored learning styles in the Virtual Biology Laboratory (VBIOLAB). Horizantal Transition (HT) had the learning skill as the transition strategy to the next level which was decided automatically by students' performance in the previous level. We have noticed that students have problems with its automatic adaptation. In our approach, the student has the facility to adaptively perform transition to the next level as per their needs.

2. MATERIAL AND METHODS

2.1. Virtual Biology Laboratory (VBIOLAB)

VBIOLAB is a 3D virtual environment that extends the advantages and benefits of HTWSP. In VBIOLAB we have added more learning materials i.e. text, 3D models, graphical information, and animated videos. Students get detailed information about the experiment through these aids and make transitions according to their preference, which improves their learning proficiencies.

VBIOLAB is a desktop application made with Unity 3D which uses a mouse and keyboard for navigation in the VE. User can select their choice of aids for experimenting and move around through the keyboard. It is a game-like environment in which the mouse has the camera viewpoint. The proposed simulated environment is shown in Figure 1.

Fig. 1. The inside scenario of VBIOLAB.

Our VBIOLAB provides some advantages over previous virtual applications:

- Unlike PowerPoint presentations, it provides a 3D interactive environment that enables the user to experience more immersion.
- It provides the facility of different learning styles to ease students learning during the experiment.
- Through various learning aids; text, 3D virtual models, graphical information, and animated videos, students can easily perform experiments in VBIOLAB.
- The learning approach HTWSP helps students to perform the experiments in VBIOLAB according to their preference.
- It resolves the issues of HT by providing the transition facility to the students instead of the automatic allocation of aids.

2.2. VBIOLAB Implementation

The VBIOLAB was implemented in Unity3D 5.6.1f1 using C# on an HP Corei3 Laptop having a specification 2.9 GHz processor, 4 GB RAM, Intel (R) HD Graphics card, and Windows 7 (64-bits) operating system. We used a Mouse and keyboard for interaction with the environment. The proposed system works on the learning approach HTWSP. To investigate the efficiency of the proposed system we also utilized the 3D application Multi Model Virtual Chemistry Lab (MMVCL) developed for HT [6, 7]. It has learning materials in the form of slides which is based on the adaptive learning approach of horizontal transition.

2.3. Experimental Protocol

To conduct the experiments, 40 students (20 males and 20 females) of intermediate level from 10 different institutions having ages between 17 to 19 years were randomly selected for evaluation. Students were divided into two groups (G1 and G2), each one had 20 males and 20 females. All students were familiar with gaming, using a keyboard, mouse, and touchscreen but they had no experience with VLEs. G1 was assigned the HT system implemented through MMVCL while G2 was trained on the HTWSP system implemented through VBIOLAB for experiments. All students were briefed about their assigned system. They were also directed about the selection of different aids and interaction with the models. The MMVCL has learning materials in the form of slides, tables, and graphs and is based on the learning approach of HT. The learning materials were altered to our topic taken from biology "Identification of various bones of the human skeleton". MMVCL and VBIOLAB systems were installed on systems during experimentation. Students were asked to perform experiments on both systems and give a subjective test for each of them. We also evaluated the system usability scale (SUS) of both systems. At the final step questionnaire was provided to the students for evaluation for both approaches. In HTWSP system the experiment "Identification of various bones of Human skeleton" was experimented. We have selected four modules; skull and ribs from the axial skeleton and upper limb and lower limb from the appendicular skeleton. Students in G2 experimented with VBIOLAB utilizing multiple aids of their choice with the HTWSP approach while those in G1 used the learning approach of HT.

2.4. Horizontal Transition with Student Preference (HTWSP)

The proposed learning approach HTWSP is based on the concept of allowing students to choose their preferred learning styles according to their needs and pace. This approach allows each student to select his own choice of learning materials instead of automatically adapted aids. We have worked on the presumed learning approach to solve the problems of learners in many ways. We have provided detailed information in the form of aids i.e. textual, graphical, 3D models related to the experimental modules, and animated video. Categorizing students and providing details to each student according to his performance in the previous module creates confusion and students need more information in the next module. The proposed learning approach eliminates this issue by providing an aid selection facility to the students. Thus weak and good students can participate more dynamically and achieve learning objectives suitably. HTWSP allows students to stay in a certain module and attain more information about that learning module through various aids of their choice. To go to the next learning module there is a mechanism of vertical transition which allows a student to make quick progress by skipping the details about a certain module. Students are allowed to make the vertical transition to their

preference, thus good students are prevented from being overwhelmed. Figure 2 shows the proposed system architecture.

The description of each Module of the proposed system is explained below.

- **Start**
  The process begins here, initiating the learning system.
- **Learning Module M**
  This is the first learning module where students engage with the material. It provides foundational knowledge or concepts to the learners.
- **User Input**
  After interacting with Learning Module M, the system collects feedback or input from the student regarding their learning progress, preferences, or needs.
- **User Decision**
  Based on the input, the student chooses how to proceed. This decision determines the type of transition (horizontal or vertical) and subsequent actions.
- **Repeat with Different Aid(s)**
  The student continues with the revised module until they are satisfied with their understanding.
- **End**
  The learning process concludes here after the student completes all required modules and transitions.

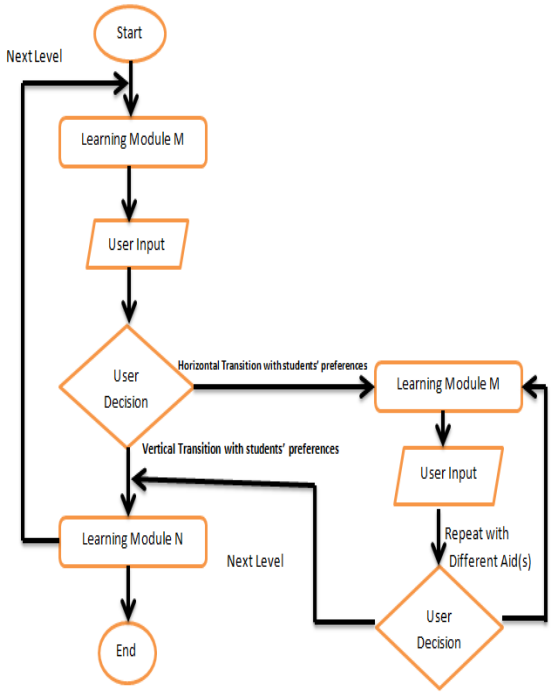

Fig. 2. The proposed system architecture.

3. RESULTS AND DISCUSSION

3.1. Students' Learning

This section presents the results of the tests after experiments conducted on HT and proposed systems for students. The experimental results show that 75% of students got high marks using the HTWSP system, while 10 % of students got lower marks on the HTWSP system as compared to the HT system. Similarly, 15% of students got the same marks while conducting experiments on HT and HTWSP systems. The overall result showed improved student performance in terms of mean and standard deviation (STD) of marks obtained. The mean and STD of the HT system were 64.75 and 16.02. The mean and STD of the HTWSP system were 77.5 and 14.97. Figure 3 illustrates the results of both systems in terms of mean and standard deviation.

3.2. Standard Usability Scale (SUS) Analysis

The system usability scale (SUS) is an efficient tool for measuring the subjective view of the usability of a system. It provides a high-level measurement of subjective usability. It proved to be a valid and reliable tool for analyzing the usability of systems and can be used for a variety of systems and types of technologies i.e. hardware, software, websites, business software, cell phones, apps, etc. Particularly, SUS can be used to compare two versions of an application that are centered on diverse technologies [20]. A SUS score of 68 or higher is generally considered acceptable usability. We compared the HT and HTWSP virtual applications through SUS by providing the SUS templates to the students. 40 students participated in the evaluation

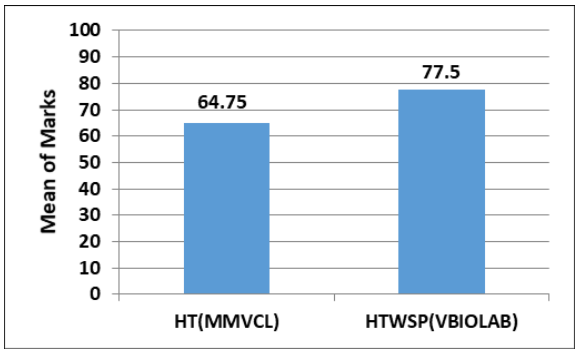

Fig. 3. Mean and STD of students' marks on both systems.

process and provided their opinions about both systems after performing experiments. For HT, the average SUS score was 71.25 while HTWSP average SUS score was 79.75 which indicates the efficiency and reliability of the proposed system. Figure 4 illustrates the SUS scores.

3.3. Subjective Evaluation

We distributed a questionnaire among 40 students for subjective evaluation of the HTWSP system. Table 1 shows the questionnaire which consists of five questions in which Q1,Q2 and Q3 are related to the efficiency of the HTWSP system. Figure 5 shows students' responses for Q1, Q2, and Q3 on a scale of 5 points. Q4 is about the prefered learning approach, for which students responses are shown in Figure 6. Q5 is related to the system attributes of both virtual environments which are given in Table 2. Students were asked about the proposed learning approach HTWSP and if it provided the student's choice of learning style. 60% of students marked it strongly agree, 25% agreed, 10% were neutral and 5% disagreed. The next question was about the freedom of selection and repetition of aids in the proposed system in contrast with the HT system. 65% selected strongly agreed, 30% agreed, 3% were neutral and 2% disagreed. In the HT, aids were provided automatically to the students for the next learning module, thus students were asked about the manual aid selection facility of the HTWSP. 58% selected strongly agree, 26% were agree, 6% were neutral and 10% were disagree as shown in Figure 5. The fourth question (Q4) was about both learning approaches. Students were asked about their preferred learning approach. 88% preferred the proposed learning approach "HTWSP" while 12% were in favor of the "HT" (see Figure 6).

3.4. Comparative Analysis

In Q5 we provided a table comprised of 8 questions to inquire students about environments of HT and

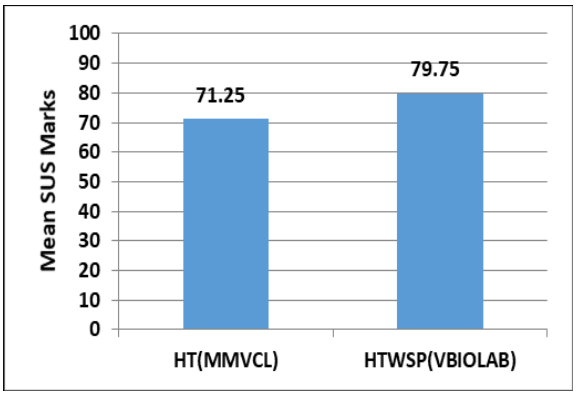

Fig. 4. SUS results of both systems**.**

Table 1. List of questions.

S. No.	Questions
1	The HTWSP provides learning styles according to the student's choice.
2	In contrast with the HT (MMVCL), the HTWSP (VBIOLAB) eliminates the concerns of time-bound and non-repeatable aid issues.
3	Instead of an automatic adaptation of teaching materials for the next learning module, the HTWSP was more effective.
4	You have utilized both learning approaches; HT and the HTWSP, which learning approach will you prefer?
5	Comparative analysis of system attributes

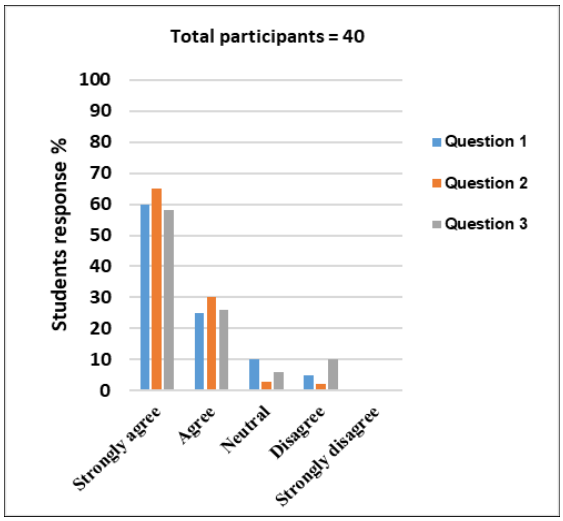

Fig. 5. Students' response for Q1, Q2 and Q3.

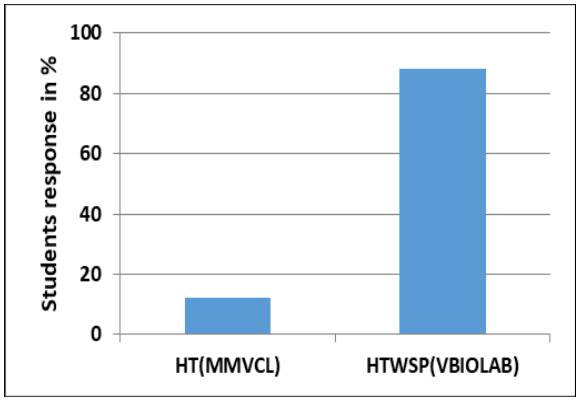

Fig. 6. Students prepared learning approach.

HTWSP systems. Table 2 shows questions related to the comparison of various attributes. For the first attribute, 81% of students marked the proposed system while 19% of students were in favor of the HT. For the second attribute, 84% marked the HTWSP system and 16% marked the HT. 83% of students marked the HTWSP for the third attribute and 17% marked the HT system. For the fourth attribute, 75% were in favor of the HTWSP system while 25% marked the HT system. For the fifth attribute, 80% marked the HTWSP and 20% preferred the HT. For the sixth attribute, 82% of students marked the HT to be intricate in transitions while 18 % marked the HTWSP system. For the seventh attribute, 76% were in favor of the HTWSP system and 24% selected the HT system. For the last attribute, 78% of students marked the HTWSP system to be student-friendly while 22% marked the HT system as shown in Figure 7.

From the overall results, it is clear that HTWSP significantly improved the learning performance of students and system usability, with 75% of students achieving higher marks and a mean score of 77.5 compared to 64.75 in the previous system. SUS scores favored the proposed system (79.75 vs. 71.25), and 88% of students preferred its customizable and student-centered approach. Most of the students (81-84%) found it more user-friendly, motivating, and efficient across various attributes, highlighting its efficiency over the old system.

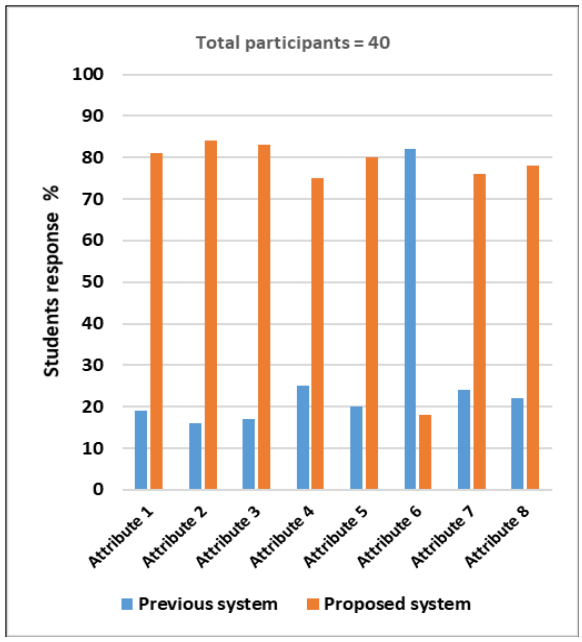

Fig.7. Comparison of HT and HTWSP systems.

Table 2. Comparative analysis of various system attributes.

S. No.	Attribute
1	The System Provides a Better Interaction Interface for Learning
2	The System Provides a More Natural Environment for Learning
3	The System Provides Ease of Navigation in the Virtual Environment
4	The System Provides Efficient Learning Materials and Models
5	The System Motivation Students Towards Learning
6	Intricate Horizontal and Vertical Transitions
7	Overall Efficiency of the system
8	The System is Student Friendly

The results of the statistical assessment and subjective evaluation proved that all the participants could accomplish their tasks in a short time by using VBIOLAB. VBIOLAB is an efficient application for familiarizing students with biology experiments and it can overcome the problems that are faced in educational institutions related to biology laboratories, i.e., space, equipment, and time. VBIOLAB provides students with an advanced 3D interactive environment, 3D models, textual, graphical, and animated video aids, and the freedom to select from these aids. We have provided an effective learning approach that delivers detailed and repeatable information through various aids that the students prefer. Experiments show that HTWSP improves students' learning skills and they take more interest in biology learning. The textual, graphical, 3D models, and animated video information are very helpful for students in improving their grades. Through different learning styles in VBIOLAB, they can perform their experiments without their teacher. The feedback of the participants also proved that the VBIOLAB is easy to use and easy to understand. All participants also endorsed that VBIOLAB is very useful and suitable for biology teachers and students because it provides a realistic virtual environment and facilitates the experimental process. VBIOLAB is an efficient tool for educational institutions to adopt as a replacement for the real lab which addresses the limitations of physical labs.

4. CONCLUSIONS

In this study, a key issue "the lack of adaptability to individual student needs and preferences" is addressed. Previous adaptive virtual environments provide automatic transitions between modules, leaving little space for student autonomy and preferred learning styles. To address this problem, we developed and tested the HTWSP approach, integrated into the VBIOLAB. Our developed application is very helpful for educational institutions where students can perform their biology experiments in a real-world biology laboratory. We have provided an effective learning approach inside a virtual biology laboratory to enhance students' learning. We conducted different tests on students to find the expediency and competence of the VBIOLAB and the learning approach HTWSP. Experimental results demonstrate that 75% of students improved their examination scores using VBIOLAB. The mean examination scores and system usability scale (SUS) ratings for VBIOLAB surpassed the HT system [6]. Moreover, in subjective evaluations, 88% of students preferred the HTWSP system. Overall evaluations prove that the HTWSP implemented through VBIOLAB is a very useful and efficient application for biology practical learning and the user can easily understand and use the system. HTWSP proved to be an effective learning approach. Providing different learning styles with the advantage of free selection among these aids greatly enhances students' curiosity and performance. Compared to previous works of researchers our system is very easy and flexible in usage, understanding the environment, performing the experiment with ease, and improving learning. The system's performance was tested on a specific setup, and factors like cultural differences or student-selected learning paths may affect consistency and applicability.

5. CONFLICT OF INTEREST

The authors declare no conflict of interest.

6. REFERENCES

1. J. Wei, J. He, J. Liu, G. Xuan, Y. Wei, X. Jiang, S. Luo, and F. Mao. Application research of virtual reality in technology in landscape design. *Journal of Physics: Conference Series* 1302(4): 042050 (2019).
2. C. Christou. Virtual reality in education. In: Affective, interactive and cognitive methods for e-learning design: creating an optimal education experience. A. Tzanavari and N. Tsapatsoulis (Eds.) *IGI Global Scientific Publishing* pp. 228-243 (2010).
3. A. Sypsas and D. Kalles. Virtual laboratories in biology, biotechnology and chemistry education: a literature review. *Proceedings of the 22nd Pan-Hellenic Conference on Informatics, (29th November-1st December 2018) Athens, Greece* (2018).
4. R. Subramanian and I. Marsic. ViBE: Virtual biology experiments. In: Proceedings of the 10th international Conference on World Wide Web 2001. *Hong Kong Hong Kong, (May 1 - 5, 2001)* pp. 316-325 (2001).
5. P. Papadopoulou, K.T. Chui, L. Daniela, and M.D. Lytras. Virtual and augmented reality in medical education and training: innovative ways for transforming medical education in the 21st century. In: Cognitive computing in technology-enhanced learning. M.D. Lytras, N. Aljohani, L. Daniela, and A. Visvizi (Eds.). *IGI Global Scientific Publishing* pp. 109-150 (2019).
6. A. Alam, S. Ullah, and N. Ali. The effect of learning-based Adaptivity on students' performance in 3D-virtual learning environments. *IEEE Access* 6: 3400-3407 (2017).
7. A. Alam and S. Ullah. Adaptive 3D-Virtual Learning Environments: From Students' Learning Perspective. *2016 International Conference on Frontiers of Information Technology (FIT), IEEE (1st December 2016), Islamabad, Pakistan* pp. 7-10 (2016).
8. L. Chittaro and R. Ranon. Adaptive hypermedia techniques for 3D educational virtual environments. *IEEE Intelligent Systems* 22(4): 31-37 (2007).
9. R.A. Kockro, C. Amaxopoulou, T. Killeen, W. Wagner, R. Reisch, E. Schwandt, A. Gutenberg, A. Giese, E. Stofft, and A.T. Stadie. Stereoscopic neuro anatomy lectures using a three-dimensional virtual reality environment. *Annals of Anatomy-Anatomischer Anzeiger* 201: 91-98 (2015).
10. J.H. Seo, B.M. Smith, M. Cook, E. Malone, M. Pine, S. Leal, Z. Bai, and J. Suh. Anatomy builder VR: Applying a constructive learning method in the virtual reality canine skeletal system. Advances in Human Factors in Training, Education, and Learning Sciences. Proceedings of the AHFE 2017. In: International Conference on Human Factors in Training, Education, and Learning Sciences. *Springer International Publishing (July 17-21 2018), Los Angeles, California, USA* pp. 245-252 (2018).
11. C. Byukusenge, F. Nsanganwimana, and

A.P. Tarmo. Investigating the effect of virtual laboratories on students' academic performance and attitudes towards learning biology. *Education and Information Technology* 29(1): 1147-1171 (2024).

12. O. Troyer, F. Kleinermann, and A. Ewais. Enhancing virtual reality learning environments with adaptivity: Lessons learned. In: HCI in Work and Learning, Life and Leisure: G. Leitner, M. Hitz, and A. Holzinger (Eds.). USAB 2010, Lecture Notes in Computer Science, vol. 6389. *Springer, Berlin, Heidelberg* pp. 244-265 (2010).
13. S. Jang, J.M. Vitale, R.W. Jyung, and J.B. Black. Direct manipulation is better than passive viewing for learning anatomy in a three-dimensional virtual reality environment. *Computers & Education* 106: 150-165 (2017).
14. N. Cristina, M. Arias, C. Carolina, A. Henríquez, and P. Riquelme. Assessment of Student and Teacher Perceptions on the Use of Virtual Simulation in Cell Biology Laboratory Education. *Education Sciences* 14(3): 243 (2024).
15. D. An and M. Carr. Learning styles theory fails to explain learning and achievement: Recommendations for alternative approaches. *Personality and Individual Differences* 116: 410-416 (2017).
16. D. Tsirulnikov, C. Suart, R. Abdullah, F. Vulcu, and C.E. Mullarkey. Game on: immersive virtual laboratory simulation improves student learning outcomes & motivation. *FEBS Open Bio* 13(3): 396-407 (2023).
17. I. Reisoğlu, B. Topu, R. Yılmaz, T. Karakuş, and Y. Göktaş. 3D virtual learning environments in education: A meta- eview. *Asia Pacific Education Review* 18: 81-100 (2017).
18. T.M. Gunathilaka, M.S. Fernando, and H. Pasqual. Individual learning path personalization approach in a virtual learning environment according to the dynamically changing learning styles and knowledge levels of the learner. *International Journal of Advanced and Applied Sciences* 5(5): 10-19 (2018).
19. M.T. Alshammari. Design and evaluation of an adaptive framework for virtual learning environments. *International Journal of Advanced and Applied Sciences* 7(5): 39-51 (2020).
20. J. Brooke. SUS: a retrospective. *Journal of Usability Studies* 8(2): 29-40 (2013).

Proceedings of the Pakistan Academy of Sciences: A Physical and Computational Sciences Suppl. Data: 1-5 (2024)

ISSN (Print): 2518-4245; ISSN (Online): 2518-4253

Pakistan Academy of Sciences

Supplementary Data

Study of Newly Synthesized Pyridinium-based Cationic Surfactants for Drug Interaction and Antibacterial Activity

Ali Jaan[1,2], Saqib Ali[2], Mohsin Javed[1], Ali Haider[2], Khurram Shahzad Munawar[3,4]*, Saja Abdulrahman Althobaiti[5], and Mahboob ur Rehman[6]

[1]Department of Chemistry, School of Science, University of Management and Technology, C-II Johar Town, Lahore, Pakistan

[2]Department of Chemistry Quaid-i-Azam University, 45320, Islamabad, Pakistan

[3]Institute of Chemistry, University of Sargodha, Sargodha, 40100, Pakistan

[4]Department of Chemistry, University of Mianwali, Mianwali, 42200, Pakistan

[5]Department of Chemistry College of Sciences and Humanities, Prince Sattam Bin Abdulaziz University, Saudi Arabia

[6]Cardiology Department, Pakistan Institute of Medical Sciences (PIMS), Islamabad, Pakistan

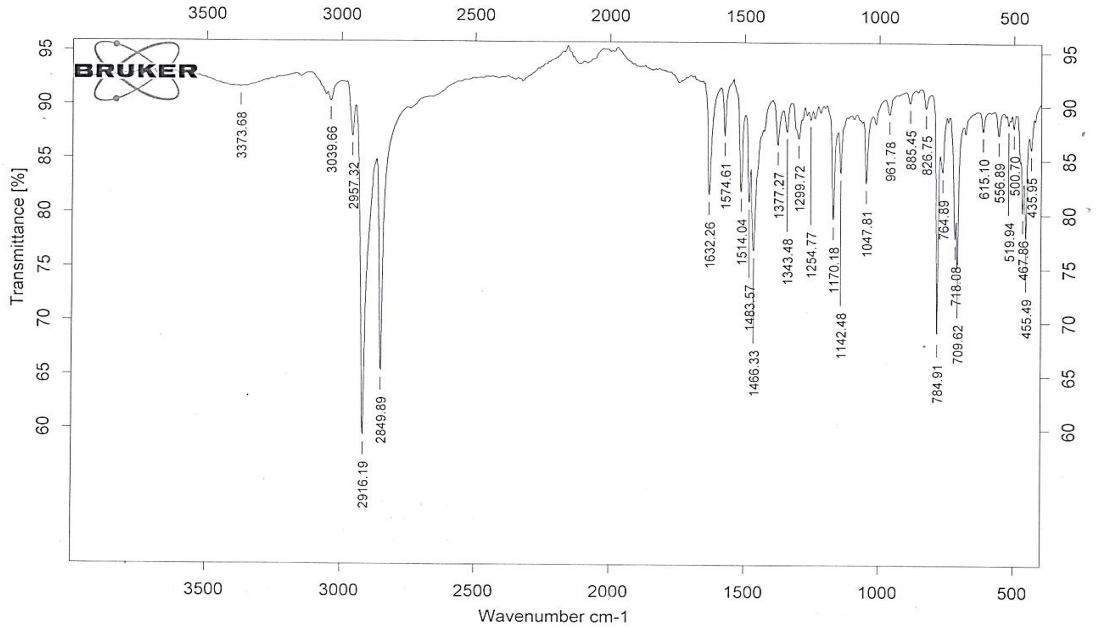

Fig. S1. FT-IR spectrum of sample A1.

* Corresponding Author: Khurram Shahzad Munawar <khurramchemist@gmail.com>

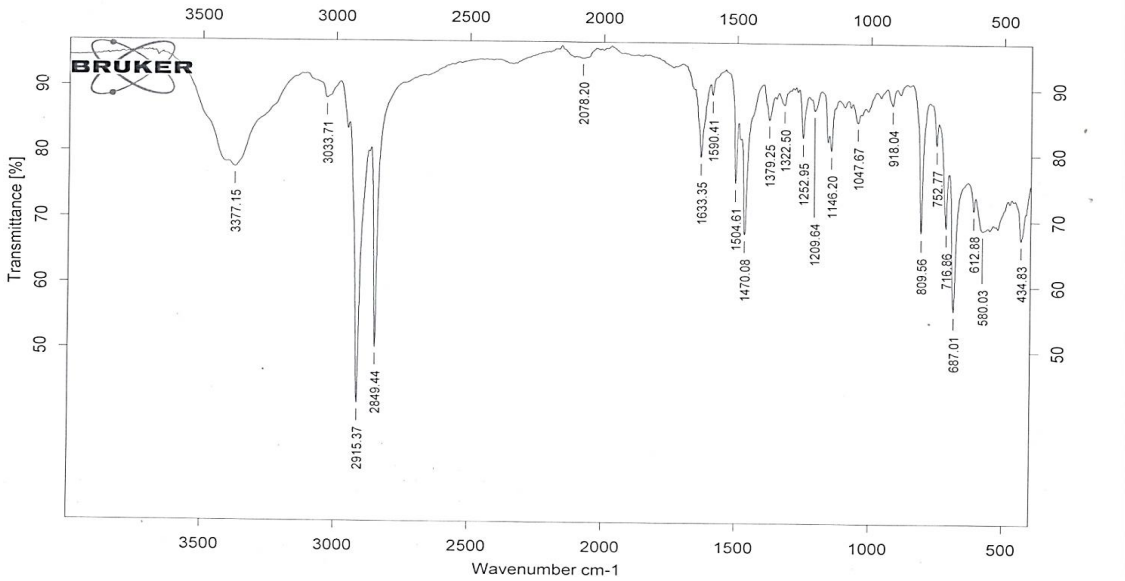

Fig. S2. FT-IR spectrum of sample A2.

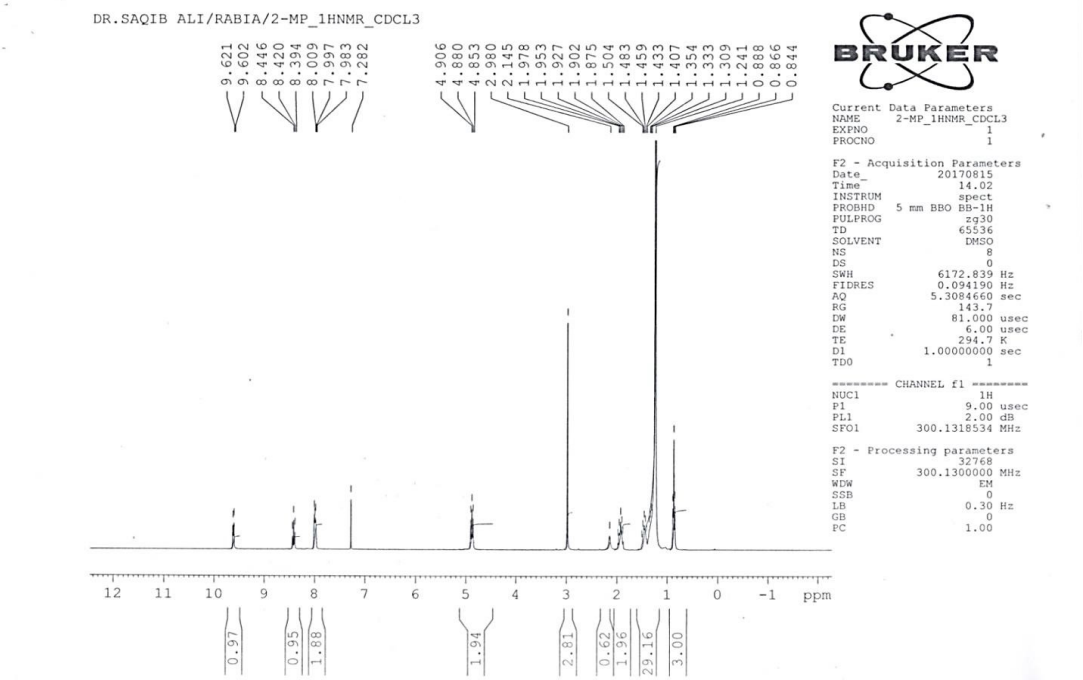

Fig. S3. [1]H-NMR spectrum of sample A1.

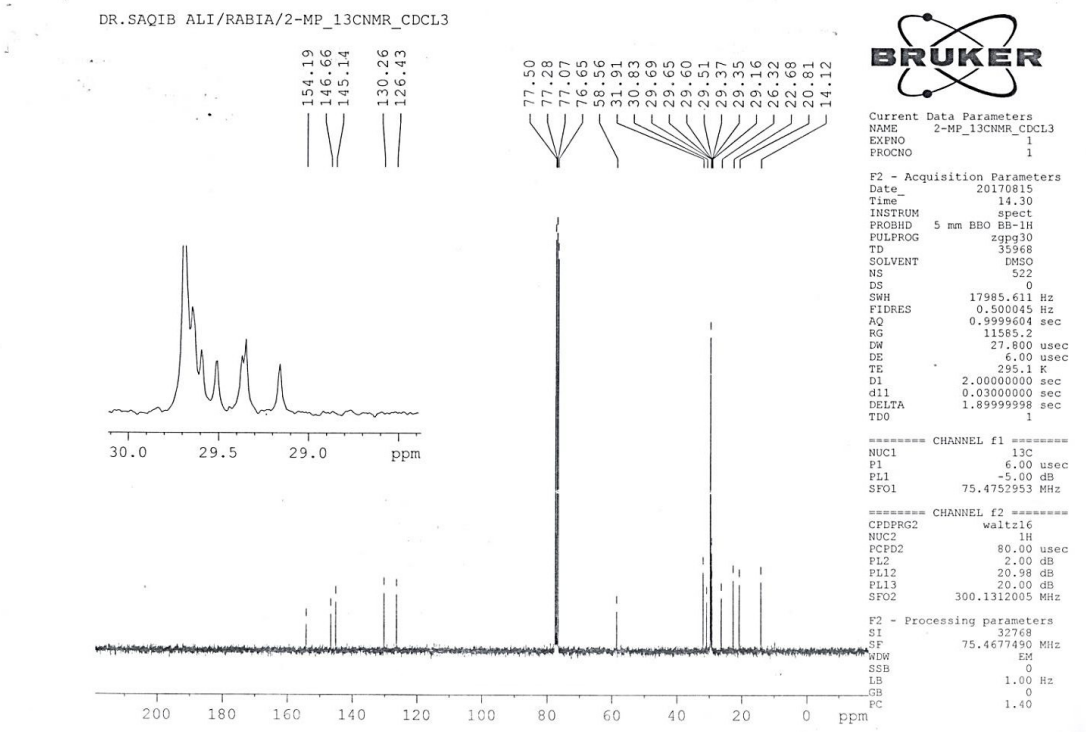

Fig. S4. ^{13}C-NMR spectrum of sample A1.

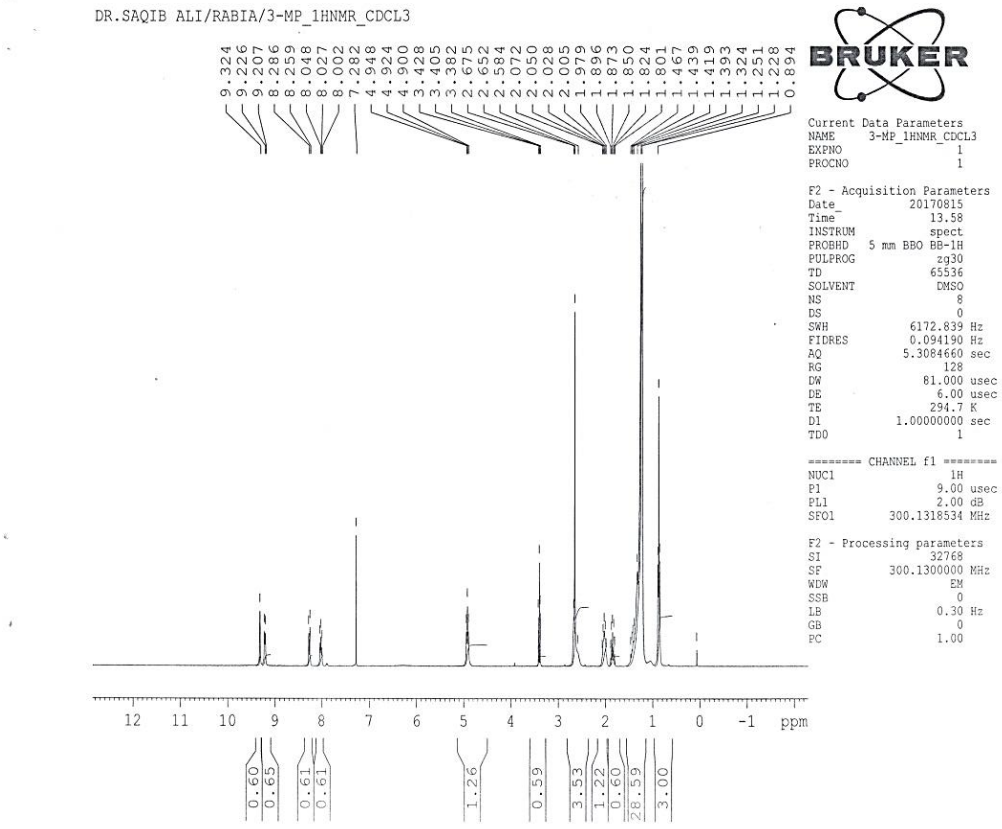

Fig. S5. ^{1}H-NMR spectrum of sample A2.

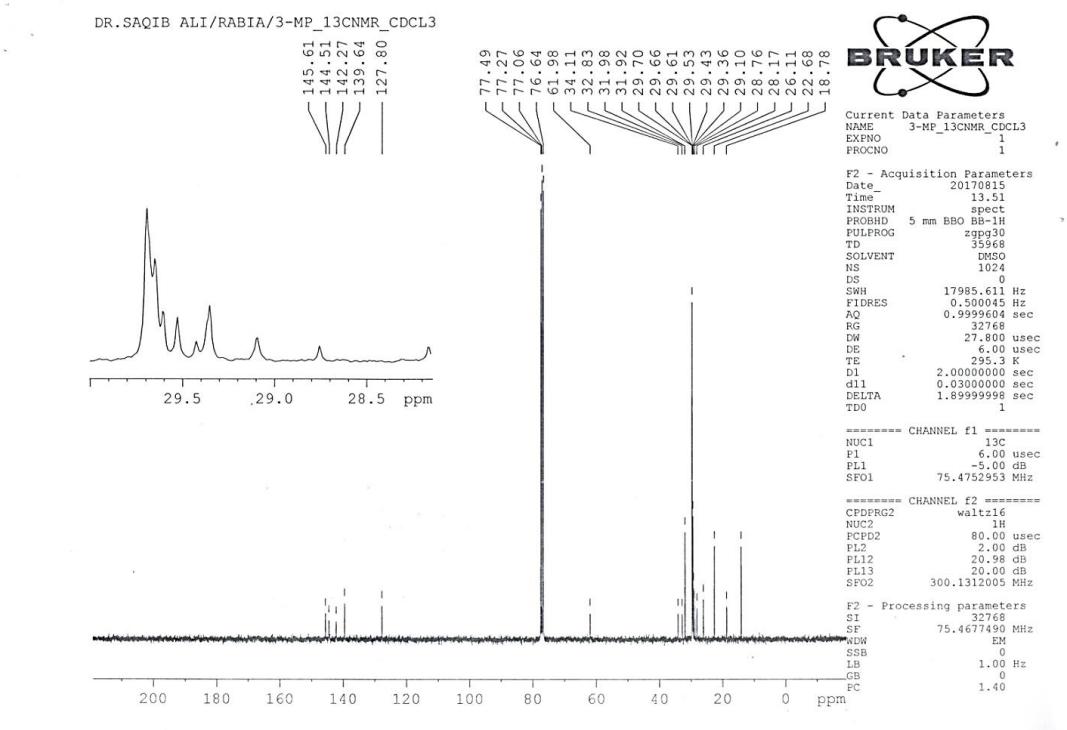

Fig. S6. ^{13}C-NMR spectrum of sample A2.

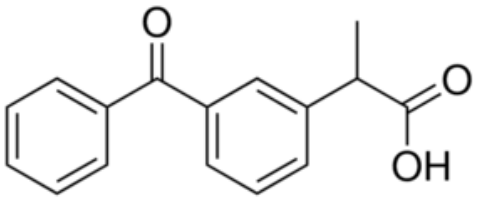

Fig. S7. Structure of ketoprofen.

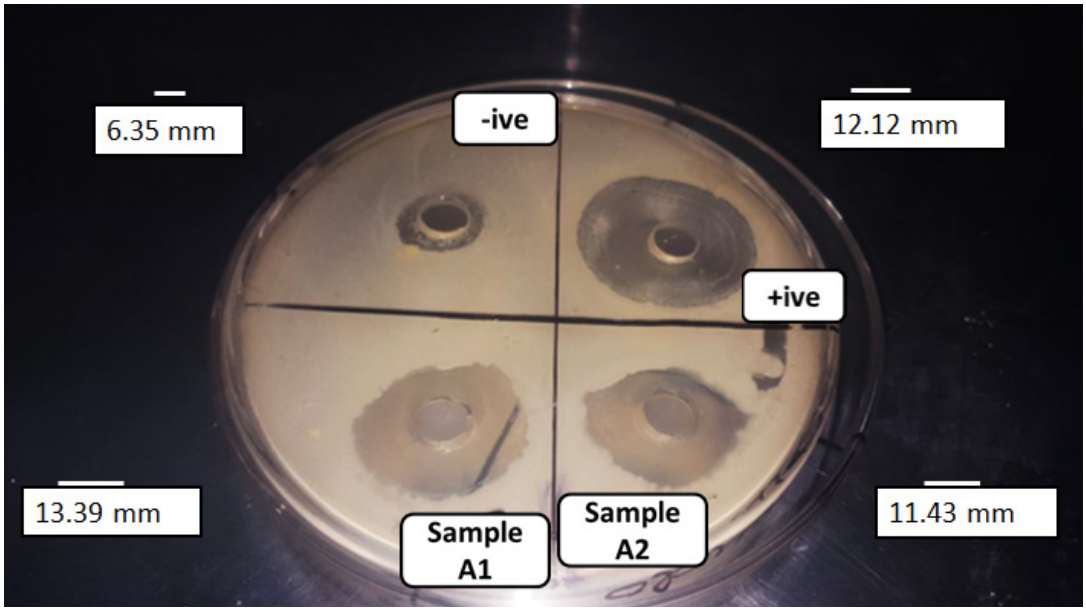

Fig. S8. Inhibition zones of samples A1 and A2 against *Staphylococcus pseudo*.

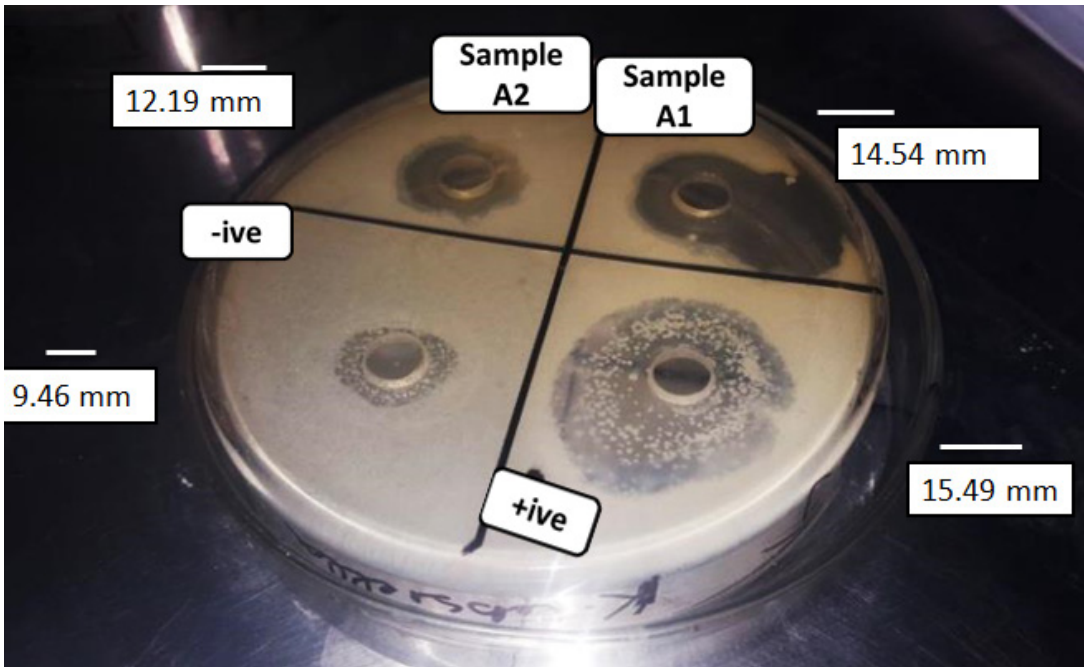

Fig. S9. Inhibition zones of samples A1 and A2 against *Klebsiella pneumoniae*.

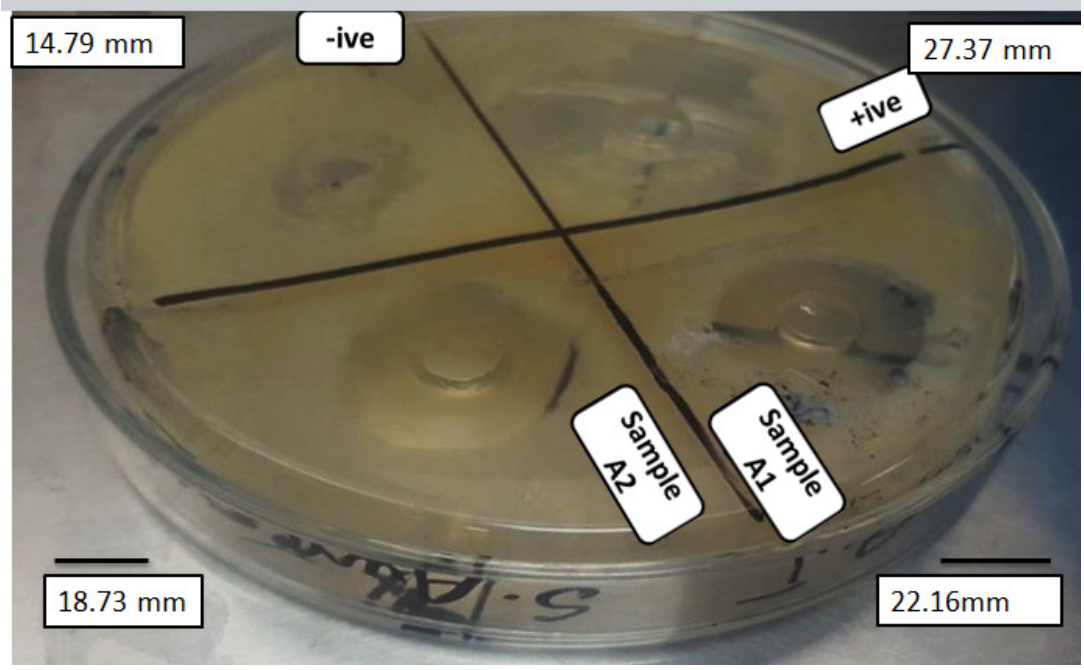

Fig. S10. Inhibition zones of samples A1 and A2 against *Staphylococcus aureus*.

Instructions For Authors

Manuscript Writing

The manuscript may contain a Title, Abstract, Keywords, INTRODUCTION, MATERIALS AND METHODS, RESULTS, DISCUSSION (or RESULTS AND DISCUSSION), CONCLUSIONS, ETHICAL STATEMENT (if applicable), ACKNOWLEDGEMENTS, CONFLICT OF INTEREST and REFERENCES, *and any other information that the author(s) may consider necessary*.

Title (Bold and font size 16): The title should be expressive, concise, and informative to the entire readership of the journal. It may include common terms, to make it more identifiable when people search online. Please avoid the use of long pervasive terms and non-standard or obscure abbreviations, acronyms, or symbols.

Abstract (font size 10, max 250 words)**:** Must be self-explanatory**,** stating the rationale, objective(s), methodology, main results, and conclusions of the study. Abbreviations, if used, must be defined on the first mention in the Abstract as well as in the main text. Abstracts of review articles may have a variable format.

Keywords (font size 10)**:** Provide five to eight keywords consisting of words and phrases that are closely associated with the topic depicting the article.

INTRODUCTION (font size 11)**:** Provide a clear and concise statement of the problem, citing relevant recent literature, and objectives of the investigation. Cite references in the text by number in square brackets**,** the reference must be cited in a proper English sentence [1]. or "... as previously described [3, 6–8]". For a single author: Bednorz [2] investigated the environmental pollution ... When there are only two authors: Bednorz and Allan [2] investigated the environmental pollution ... and for three or more authors: Bednorz *et al.* [2] investigated the environmental pollution ..; and list them in the REFERENCES section, in the order of citation in the text.

MATERIALS AND METHODS (font size 11)**:** Provide an adequate account of the procedures or experimental details, including statistical tests (if any), concisely but sufficiently enough to replicate the study. Relevant references to methodology must be cited.

RESULTS (font size 11)**:** Be clear and concise with the help of appropriate Tables, Figures, and other illustrations. Data should not be repeated in Tables and Figures but must be supported with statistics. The data presented in Tables and Figures must be elaborated in the main text.

DISCUSSION (font size 11)**:** Provide interpretation of the RESULTS in the light of previous relevant studies, citing published references.

CONCLUSIONS (font size 11)**:** Briefly state the implication of your study findings, and carefully address the study questions. Confine your conclusions according to the objectives of your study and the aspects covered in the abstract. Discuss both positive and negative findings.

ETHICAL STATEMENT (font size 10)**:** The statement of ethical approval by an appropriate ethics committee or review board must be included in the manuscript (if applicable), as per the Journal's policy.

ACKNOWLEDGEMENTS: (font size 10)**:** In a brief statement, acknowledge the financial support and other assistance.

CONFLICT OF INTEREST (font size 10)**:** State if there is any conflict of interest.

REFERENCES (font size 10)**:** References must be listed in numerical order as listed in the main text. Only published (and accepted for publication) journal articles, books and book chapters, conference proceedings, online reports, a degree thesis, and materials available on the website qualify for REFERENCES.

Declaration: Provide a declaration that: (i) the results are original, (ii) the same material is neither published nor under consideration for publication elsewhere, (iii) approval of all authors has been obtained, and (iv) in case the article is accepted for publication, its copyright will be assigned to the *Pakistan Academy of*

Sciences. Authors must obtain permission to reproduce, where needed, copyrighted material from other sources and ensure that no copyrights are infringed upon.

Manuscript Formatting

Manuscripts must be submitted in Microsoft Word (Latest Version .doc or .docx format); pdf files are not acceptable. Figures can be submitted separately in TIFF, GIF, JPEG, EPS, or PPT. Manuscripts, in *Times New Roman*, 1.15 spaced (but use single-space for Tables, long headings, and long captions of tables and figures). The Manuscript sections must be numbered, i.e., **1. INTRODUCTION, 2. MATERIALS AND METHODS,** and so on… (a) **Title** of the article **(**Capitalize the initial letter of each main word, font-size 16, **bold**), max 160 characters (no abbreviations or acronyms), depicting article's contents; (b) Author's complete name (font size 12, **bold**), and professional affiliation (i.e., each author's Department, Institution, Mailing address, and Email and Contact number, but no position titles) (font size 12); (c) Indicate the corresponding author with *; and (d) **Short running title**, max 50 characters (font size 10).

Headings and Subheadings (font size 11): All flush left

LEVEL-1: **ALL CAPITAL LETTERS; Bold**

Level-2: **Capitalize Each First Letter (**Except prepositions**); Bold**

Level-3: Capitalize the first letter only (Sentence case)***; Bold, Italic***

Level-4: *Run-in head*; *Italics*, *in the normal paragraph position. Capitalize the first letter only and end in a colon (i.e., **:**)*

A list of REFERENCES must be prepared as under:

a. Journal Articles *(Name of journals must be stated in full)*

1. J. Rashid, A. Ahsan, M. Xu, I. Savina, and F. Rehman. Synthesis of cerium oxide embedded perovskite type bismuth ferrite nanocomposites for sonophotocatalysis of aqueous micropollutant ibuprofen. *RSC Advances* 13(4): 2574-2586 (2023).

2. A. Fayyaz, N. Ali, Z.A. Umar, H. Asghar, M. Waqas, R. Ahmed, R. Ali, and M.A. Baig. CF-LIBS based elemental analysis of Saussurea simpsoniana medicinal plant: a study on roots, seeds, and leaves. *Analytical Sciences* 40(3): 413-427 (2024).

3. W. Bialek and S. Setayeshgar. Cooperative sensitivity and noise in biochemical signaling. *Physical Review Letters* 100: 258–263 (2008).

b. Books

4. W.R. Luellen (Ed.). Fine-Tuning Your Writing. *Wise Owl Publishing Company, Madison, WI, USA* (2001).

5. U. Alon and D.N. Wegner (Eds.). An Introduction to Systems Biology: Design Principles of Biological Circuits. *Chapman & Hall/CRC, Boca Raton, FL, USA* (2006).

c. Book Chapters

6. M.S. Sarnthein, J.E. Smolen, and J.D. Stanford. Basal sauropodomorpha: historical and recent phylogenetic developments. In: The Northern North Atlantic: A Changing Environment. P.R. Schafer and W. Schluter (Eds.). *Springer, Berlin, Germany* pp. 365–410 (2000).

7. S. Brown and L.A. Boxer. Functions of Europhiles. In: Hematology, (4th ed). W.J. Williams, E. Butler, and M.A. Litchman (Eds.). *McGraw Hill, New York, USA* pp. 103–110 (1991).

d. Reports

8. M.D. Sobsey and F.K. Pfaender. Evaluation of the H_2S method for Detection of Fecal Contamination of

Drinking Water. Report No.-WHO/SDE/WSH/02.08. *Water Sanitation and Health Programme, WHO, Geneva, Switzerland* (2002).

e. Online References

These should specify the full URL for reference, please check again to confirm that the work you are citing is still accessible:

9. UNESCO. Global Education Monitoring Report 2024/5: Leadership in education−Lead for learning. *United Nations Educational, Scientific and Cultural Organization, Paris, France* (2024). https://digitallibrary.un.org/record/4066661?ln=en&v=pdf

10. L.M. Highland and P. Bobrowsky. The landslide handbook−A guide to understanding landslides. Circular 1325. *US Geological Survey, Reston, Virginia* (2008).

    https://pubs.usgs.gov/circ/1325/pdf/C1325_508.pdf

f. Conference Proceedings

11. M. Khalid, A.B. Majid, F. Mansour, and C.R. Smith. Word Representations with Recursive Neural Networks for Morphology. *27th European Conference on Signal Processing, (2nd - 6th September 2021), Madrid, Spain* (2021).

g. A Degree Thesis

12. M. Afzal. Investigation of structural and magnetic properties of nanometallic Fe-Mn Alloys. Ph.D. Thesis. *Quaid-i-Azam University, Islamabad, Pakistan* (2023).

Tables: Insert all tables as editable text, not as images. Number tables consecutively following their appearance in the text. A concise but self-explanatory heading must be given. Tables should be numbered according to the order of citation (like **Table 1.**, **Table 2.** (font size 10)). *Do not* abbreviate the word "Table" to "Tab.". Round off data to the nearest three significant digits. Provide essential explanatory footnotes, with superscript letters or symbols keyed to the data. Do not use vertical or horizontal lines, except for separating column heads from the data and at the end of the Table.

Figures: In the main text write Figure, not Fig. Figures may be printed in two sizes: column width of 8.0 cm or page width of 16.5 cm; In the Figure caption, number them as **Fig. 1.**, **Fig. 2.** Captions to Figures must be concise but self-explanatory (font size 10). Laser-printed line drawings are acceptable. Do not use lettering smaller than 9 points or unnecessarily large. Photographs must be of high quality. A scale bar should be provided on all photomicrographs. All Figures should have sufficiently high resolution (minimum 300 dpi) to enhance the readability. Figures as separate files in JPG or TIFF format may be provided.

SUBMISSION CHECKLIST

The following list will be useful during the final checking of an article before submission to the journal.

1. Manuscript in MS Word format
2. Cover Letter
3. Novelty Statement
4. Copyright Form
5. Figures in JPG or TIFF format

In case of any difficulty while submitting your manuscript, please get in touch with:

Editor-in-Chief

Pakistan Academy of Sciences
3-Constitution Avenue,
G-5/2, Islamabad, Pakistan
Email: editor@paspk.org
Tel: +92-51-920 7140
Websites: http://www.paspk.org/proceedings/; http://ppaspk.org/

PROCEEDINGS OF THE
PAKISTAN ACADEMY OF SCIENCES: PART A
Physical and Computational Sciences

CONTENTS

Volume 61, No. 4, December 2024 **Page**

Research Articles

PAKISTAN ACADEMY OF SCIENCES, ISLAMABAD, PAKISTAN

HEC Recognized; Scopus Indexed

Websites: http://www.paspk.org/proceedings/; http://ppaspk.org